

Light-quark hadron spectroscopy: A geometric quark model for S states*

Malcolm H. Mac Gregor

Lawrence Livermore Laboratory, Livermore, California 94550

(Received 4 August 1971; revised manuscript received 26 December 1973)

A geometric light-quark model is described in which all quark-quark binding energies are less than 5%. The quark states of this model are formed entirely from a single mass quantum M , which has the same principal quantum numbers as the kaon. M appears in a spinless configuration ($M \sim 70$ MeV), and also in a relativistically spinning configuration ($M_s \sim 110$ MeV) as the nucleon quark $S \equiv 3M_s \sim 330$ MeV. The mass ratio $M_s/M \sim \frac{3}{2}$ is a calculated quantity. The model can be formulated with a total of ten quark-state parameters: the masses $M^0 = 70.0$ MeV, $M^\pm = 74.6$ MeV, $S^\pm = 330.6$ MeV, and $S^{\pm\pm} = 336.9$ MeV; the hadronic binding energies $MM = -5.0$ MeV, $MM_s = -5.0$ MeV, and $M_sM_s = -9.1$ MeV; a magnetic binding energy $S^\pm S^\pm = \pm 1.7$ MeV; a magnetic moment $\mu_{S^\pm} = \pm 9.3$ nuclear magnetons (μ_N); and a radius $R_M \approx 0.6$ fermi. The spin angular momentum $J = \frac{1}{2}\hbar$ of the spinor S is a calculated quantity, and the model also includes small calculated Coulomb corrections arising from multiple internal charges. With this formulation, the masses of all of the fundamental narrow-width hadron resonances— π^\pm , π^0 , K^\pm , K^0 , η , M , η' , δ^0 , p , n , $\bar{p}n$, Λ , Σ^+ , Σ^0 , Σ^- , Ξ^0 , Ξ^- , and Ω^- —are calculated to an average absolute accuracy of $\pm 0.1\%$, or ± 1 MeV, and spins, charge splittings, magnetic moments, and strangeness quantum numbers are reproduced. These calculated mass values are accurate enough to pinpoint the M meson as the fundamental ground-state member of the $M(953)$, $\eta'(958)$, $\delta^0(963)$ multiplet, a result that is experimentally confirmed by both the production modes and the decay modes for these mesons.

I. INTRODUCTION

A light-quark model for reproducing hadron resonances is described. This model is simple enough that its essential numerical features have been described in the abstract to this paper, and yet it possesses accuracy and comprehensiveness. The parameters of the model are physically identifiable, and in general they can be isolated and determined either phenomenologically from the experimental data or else from straightforward theoretical considerations. This light-quark model has a mathematically well-defined geometry, and in the present paper we introduce specific geometrical configurations for the individual quark states and for the quark clusters that constitute hadron resonances. These geometrical configurations have several important features: (1) They account for both hadronic binding energies and internal Coulomb corrections in an accurate and apparently unique manner; (2) they give spin angular momenta, magnetic moments, and the volume of a nucleon as directly calculated quantities; (3) they facilitate the pedagogical presentation of this somewhat unconventional approach to elementary particle structure. It should be recalled that Maxwell had a mechanical model for the electromagnetic field firmly in mind when he wrote down his famous set of equations. Maxwell's spinners and idler wheels have long since disappeared, leaving behind only the equations which express

their operation. The present geometrical quark model may similarly disappear, but hopefully the systematic results which it represents will remain.

In another paper,¹ denoted here as paper I, a compilation of about 130 low-mass experimental hadron resonances was presented, documented, and evaluated. In the present paper we use these data values directly, usually without further documentation. Paper I also included a phenomenological analysis of the experimental data which revealed the existence of the present set of light-quark states. It was demonstrated in I, with the aid of these quark states, that the broad-width hadron resonances can be interpreted as nuclear-physics-type rotational levels, with the narrow-width resonances constituting the rotationless S -state bandheads.² A comprehensive study of these hadron rotational bands was given in I. In the present paper, we are concerned only with the problem of reproducing the narrow-width S -state resonances.² The mapping problem—the task of reproducing all of the observed resonances, and only the observed resonances—was discussed at some length in I; this discussion is not repeated here. Also, the predictive power of this light-quark model (which was formulated several years ago) has been demonstrated in one way or another by almost $\frac{1}{4}$ of the resonances in the 130-resonance data compilation of paper I; these predictive successes are summarized in detail in that paper.

In Sec. II of the present paper the very-narrow-width S -state resonances ($\Gamma \ll 5$ MeV) are reproduced, and in Sec. III the intermediate-width S -state resonances ($\Gamma \geq 10$ MeV) are reproduced. Sec. IV summarizes the experimental, phenomenological, and theoretical evidence that can be used in order to determine numerical values for the ten parameters of this light-quark model. Although the masses and binding energies of this light-quark model are quoted here to accuracies of 0.1 MeV, this is not meant to imply that these values are actually known to that accuracy. Our purpose is rather to demonstrate that this very limited set of light-quark states (which are all formed from the quantum $M \sim 70$ MeV) has the intrinsic capability of accurately reproducing the very-well-known ground-state hadron resonances, since this capability furnishes the strongest argument for the physical reality of the basis set. Section V contains a brief summary of the present results. Several topics are amplified and extended in appendixes at the end of the paper.

The meson and baryon S -state resonances discussed in Secs. II and III total 53 resonances in all. These 53 resonances are reproduced by the present light-quark model to an average absolute mass accuracy of better than $\pm 0.4\%$.

In the present paper, and also in paper I, it is evident that we are using what is in many respects a classical description to reproduce particles and resonances which are thought to be highly quantum-mechanical in nature. The reason for this semiclassical approach is not due to any particular desire on the part of the author to circumvent quantum mechanics. Our one goal in these two papers has been to provide a spectroscopic description for these particles, including mass values, spins, charge states, and magnetic moments; and, in obtaining these spectroscopic quantities, the author was literally forced into the description that is provided here. As one example, the use of actual rotating current distributions to calculate particle magnetic moments may seem (to present-day physicists) to be a highly implausible procedure, and yet these current loops give correct answers—and in fact answers which have not been forthcoming from any field-theory model of which the author is aware. The model that we end up with in the present paper is a rather curious mixture of classical and quantum concepts. The dynamical implications of this model clearly must be investigated before the utility of this approach can be accurately assessed, and these dynamical studies may well force a revision of some of the concepts. However, on the spectroscopic level the model is, as far as the author can determine, in agreement with experiment. The geometric

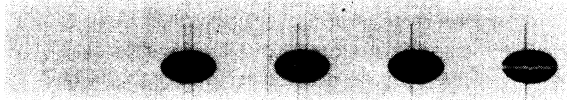
elementary particle model that is illustrated in Figs. 1–28 of the present paper is offered here not as a “solution” to the elementary particle problem, but rather as an indication of fruitful areas for further research.

II. THE VERY-NARROW-WIDTH S -STATE RESONANCES

These resonances include the π , K , η , M , η' , δ^0 , and δ^- pseudoscalar bosons, and the p , n , Λ , Σ , Ξ , and Ω metastable fermions. In addition, two bound-state resonances, $\bar{p}n$ and $K^-p \equiv \Lambda(1402)S$, are also included, since they fit in naturally with the present systematics.

The fundamental mass quantum $M \sim 70$ MeV is described in Fig. 1, and the complete set of light-quark basis states generated as combinations of quanta M is shown in Fig. 2. These basis states, $1 \equiv M$, $3 \equiv 3M$, $4 \equiv 4M$, $7 \equiv 7M$, and $S \equiv (3M)_{\text{spinning}}$, are *linear arrays* of quanta M , denoted as “cabers.”³ Although the appearance of these quark states as linear structures seems somewhat unusual, the linear arrays in fact uniquely represent both the formalism for hadronic binding energies and the formalism for applying Coulomb corrections.

Table I summarizes the numerical values of the ten independent quark-state parameters that are used in the present model. In Sec. IV, many of these parameters are deduced directly from the experimental data. Table II lists the properties of the $1, 3, 4, 7, S$ caber basis set, including their strangeness characteristics, hadronic binding en-



QUANTUM	M^+	M^0	\bar{M}^0	M^-
MASS (MeV)	74.6	70.0	73.0	74.6
CHARGE	+e	0	0	-e

FIG. 1. The fundamental mass quantum $M \sim 70$ MeV. M appears to have the same quantum numbers as the K meson; in particular, it has isotopic spin $I = \frac{1}{2}$, spin angular momentum $J = 0$ (it also appears as the spinning quantum M_s in the spinor S), and strangeness $S = \pm 1$. The shape of the quantum M is that of an oblate spheroid, with radii $R_{\text{max}} \approx \frac{1}{3}\sqrt{3} F$ and $R_{\text{min}} \approx \frac{1}{3} F$, as determined in Appendix B. As shown in Fig. 2, the quantum M occurs in its spinless form in the basis states $1 \equiv M$, $3 \equiv 3M$, $4 \equiv 4M$, and $7 \equiv 7M$, and it occurs in its spinning form in the spinor $S \equiv 3M_s$. Although the spinless quantum $M \sim 70$ MeV has not been observed experimentally, the spinning quantum M_s is related phenomenologically by the equations of special relativity to the readily observed muon (see Appendix E and Fig. 28).

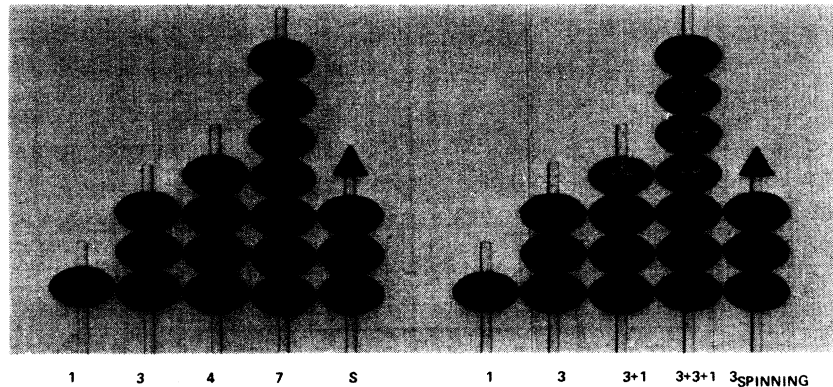


FIG. 2. The cabers 1, 3, 4, 7, S. These are formed as linear arrays of quanta M . The linear arrays account in an apparently unique manner for a number of phenomenologically required light-quark binding energy characteristics and electromagnetic characteristics, as is summarized in Table IV. These linear arrays occur both as cabers (strangeness = +1) and as anticabers (strangeness = -1), and hadronic binding energies exist only between caber-anticaber pairs. In hyperon resonances, which are formed by adding spinless anticabers to an existing nucleon spinor triplet, it is the spinless anticabers which carry the conventional strangeness quantum numbers; the conservation of baryon number is precisely equivalent to the conservation of nucleon spinor triplets, so that the strangeness of the spinor triplet, and hence also of the spinor S , does not enter into the bookkeeping of the associated-production process. Thus the spinor S is assigned a strangeness quantum number of zero, although from its hadronic binding energy it is in fact "strange." In Sec. III, "nonstrange" forms of the cabers 3, 4, and S are also described. The mass of a caber is the sum of the masses of the constituent subquanta M . The properties of the cabers 1, 3, 4, 7, S are summarized in Table II, and the spinor S is discussed in detail in Appendix B.

ergies, and mass values. A notation is introduced for the different particle-antiparticle states of these linear arrays, as follows: *strange cabers* (1, 3, 4, 7, S ; strangeness = +1); *strange anticabers* ($\bar{1}$, $\bar{3}$, $\bar{4}$, $\bar{7}$, \bar{S} ; strangeness = -1); *nonstrange cabers* ($\underline{3}$, $\underline{4}$, \underline{S} ; strangeness = 0); *nonstrange anticabers* ($\bar{\underline{3}}$, $\bar{\underline{S}}$; strangeness = 0). The "strangeness" of the spinors S and \bar{S} , which does not contribute to the strangeness quantum numbers of Gell-Mann and Nishijima, is discussed in the caption to Fig. 2. It is convenient to denote strange cabers and strange anticabers simply as "cabers" and "anticabers." Nonstrange cabers and nonstrange anticabers are usually lumped together under the general heading of "nonstrange cabers;" the distinction between these two types of nonstrange caber is of importance only for detailed associated-production reactions, as described in Appendix D.

Table III summarizes phenomenological rules for reproducing hadron resonances as clusters of cabers, with the Fermi-Yang⁴ formulation of the nucleon being used rather than the formulation of Gell-Mann and Zweig.⁵ These rules reproduce the observed spectrum of S -state hadron resonances. The rotational levels mentioned in Rule 7, which are described in detail in paper I, complete the mapping of the hadron resonance spectrum. Table IV describes some features of these hadron reso-

nances which are uniquely accounted for by the linear caber configurations of Fig. 2. Figure 3 shows the distinctive manner in which individual caber-anticaber pairs bind together, and Fig. 4 shows how these caber-anticaber pairs occur in a cluster of cabers.

Figure 5 is an energy-level diagram for the very-narrow-width $J^P = 0^-$ meson and kaon resonances (these resonances are discussed in more detail in Appendix A and the isospin labels are discussed in Ref. 6). Experimentally, the widths of these resonances appear to be much less than 5 MeV; phenomenologically, these resonances can be constructed entirely from spinless quanta M . The position of the M meson^{7,8} in Fig. 5 as the lowest-mass member of the M, η', δ^0 multiplet⁷⁻⁹ suggests that the M must be the fundamental ground-state member of this multiplet (see Table V).

Figure 6 shows the π mesons, and it illustrates the manner in which parameters (1), (2), and (5) of Table I exactly reproduce these resonances. Figure 7 describes the caber-anticaber pairs $\pi^0 = 1^0 \bar{1}^0$, $\eta = 4^+ 4^-$, $(M, \eta', \delta^0) = 7^+ 7^-$, $K^+ = 7^+$, and $K^- = 7^-$, and the mass calculations in this figure show that parameters (1), (2), and (5) also accurately reproduce these resonances. The $7^+ 7^-$ mass calculation coincides with the mass of the

TABLE I. Summary of numerical values and calculational quantities for the ten-parameter light-quark basis set. It is important to note that several of the numerical values which are given here as free parameters can be determined directly from the experimental data or from theoretical calculations, as is described in Sec. IV. M and M_s denote nonspinning and spinning quanta M .

Quark-state masses	
Parameter (1). $M^0, \bar{M}^0 = 70.0$ MeV.	
Parameter (2). $M^+, M^- = 74.6$ MeV.	
Parameter (3). $S^+, S^- = 330.6$ MeV ($S^+ \equiv M_s^0 M_s^+ M_s^0, S^- \equiv \bar{M}_s^0 M_s^- \bar{M}_s^0$).	
Parameter (4). $S^{++}, S^{--} = 336.9$ MeV ($S^{++} \equiv M_s^+ M_s^0 M_s^+, S^{--} \equiv \bar{M}_s^0 \bar{M}_s^+ \bar{M}_s^-$).	
Rule: The intrinsic masses of the spinless cabers $3 \equiv 3M$, $4 \equiv 4M$, and $7 \equiv 7M$ are the sums of the constituent masses M (see Table II).	
Hadronic binding energies	
Parameter (5). $B_{\bar{M}\bar{M}} = -5.0$ MeV, $B_{MM} = B_{\bar{M}\bar{M}} = 0$.	
Parameter (6). $B_{\bar{M}\bar{M}_s} = B_{\bar{M}_s\bar{M}} = -5.0$ MeV, $B_{MM_s} = B_{\bar{M}_s\bar{M}} = 0$.	
Parameter (7). $B_{M_s\bar{M}_s} = -9.1$ MeV, $B_{M_s M_s} = B_{\bar{M}_s \bar{M}_s} = 0$.	
Rule: These hadronic binding energies are very short-ranged; they operate directly between matching subquanta in adjacent caber-anticaber pairs.	
Magnetic binding energies	
Parameter (8). $B_{S^+ S^+} = B_{S^+ S^+} = -1.7$ MeV, $B_{S^+ S^+} = +1.7$ MeV, $B_{S^+ S^+} = +3.4$ MeV.	
Rule: These magnetic binding energies are short-ranged; the values shown here apply only to adjacent spinors in a cluster.	
Magnetic moments	
Parameter (9). $\mu_{S^+} = +9.3\mu_N$, $\mu_{S^-} = -9.3\mu_N$, $\mu_{S^{--}} = -18.6\mu_N$.	
Note: Equatorial charge distributions on the spinors S give calculated magnetic moments that are precisely a factor of three larger than the values shown here.	
Radii of the quantum M	
Parameter (10). $R_{\max} \approx \frac{1}{3}\sqrt{3}$ F.	
Dependent parameter: $R_{\min} \approx \frac{1}{3}$ F. [From the calculations of Appendix B, $R_{\min} = R_{\min}(S^\pm, 3^\pm, R_{\max})$.]	
Coulomb effects	
Coulomb self-energies: Strange cabers in general occur singly charged, and alternate charge states are formed by adding another charge; nonstrange excitation cabers occur uncharged.	
Coulomb binding energies: These are calculated classically; for definiteness, the quanta M^\pm are assumed to have centered point charges and the quanta M_s^\pm are assumed to have equatorial charge distributions, although these detailed charge distributions have little effect on the (small) Coulomb corrections.	
Spin angular momentum	
The spin angular momentum $J = \frac{1}{2}\hbar$ of the spinor S is a calculated quantity, as shown in the calculations of Appendix B.	

M , which is in agreement with the systematics of Fig. 5 and Table V. Figure 8 shows details of the η' multiplet; it illustrates the manner in which the model can reproduce the η' - M mass difference, and also the manner in which the δ^- is constructed as a charged form of the η' . The doubly charged caber 7^{+-} that appears in the δ^- in Fig. 8 also appears singly as the K^0 in Fig. 9. Arguments which single out the M meson as the fundamental member of the η' multiplet are summarized in Table V.

Figure 9 illustrates the K mesons. The caber configurations shown here reproduce the absolute masses of the kaons, the charge splitting of the masses,¹⁰ the spins and total charges of the kaons, and the strangeness values (± 1 for the K^\pm and

mixed for the K_L^0 and K_S^0). These kaon caber configurations also have significance with respect to lifetime systematics (Appendix A) and with respect to the equations for associated production (Appendix D). The fact that a secondary scattering, whose effect is clearly to cause a geometrical rearrangement, converts some K_L^0 mesons into K_S^0 mesons suggests that the difference between these two meson states is geometrical. From the negative parity of the $K_L^0 \rightarrow \pi\pi\pi$ decay and the positive parity of the $K_S^0 \rightarrow \pi\pi$ decay, we have a further suggestion that the parity and the particle-antiparticle nature of a mass quantum M^0 may depend on its spatial orientation with respect to the resonance structure in which it is contained.

TABLE II. Properties of the cabers 1, 3, 4, 7, S. These linear arrays of quanta M and \bar{M}_s , which constitute a complete set of light-quark basis states, are illustrated in Fig. 2. They occur as strange cabers and anticabers and as nonstrange cabers and anticabers. Strange caber-anticaber pairs bind hadronically with HBE $\sim 4\%$; nonstrange cabers bind hadronically with HBE $\sim 0\%$; strange caber-caber and anticaber-anticaber pairs do not bind hadronically. The mass of a caber is the sum of the constituent masses, and the "intrinsic mass" of a caber is the mass before multiple-charge Coulomb corrections have been applied.

(a) Strangeness quantum numbers and hadronic binding energies					
Strange cabers (all subquanta M) ^a	1	3	4	7	S
strangeness	+1	+1	+1	+1	"0" ^b
hadronic binding energy (to anticabers)	$\sim 4\%$	$\sim 4\%$	$\sim 4\%$	$\sim 4\%$	$\sim 4\%$
Strange anticabers (all subquanta \bar{M}) ^a	$\bar{1}$	$\bar{3}$	$\bar{4}$	$\bar{7}$	\bar{S}
strangeness	-1	-1	-1	-1	"0" ^b
hadronic binding energy (to cabers)	$\sim 4\%$	$\sim 4\%$	$\sim 4\%$	$\sim 4\%$	$\sim 4\%$
Nonstrange cabers (mixed subquanta M and \bar{M}) ^c		$\dot{3}$	$\dot{4}$		\dot{S}
strangeness		0	0		0
hadronic binding energy (to everything)		$\sim 0\%$	$\sim 0\%$		$\sim 0\%$
Nonstrange anticabers (mixed subquanta M and \bar{M}) ^c		$\bar{\dot{3}}$			$\bar{\dot{S}}$
strangeness		0			0
hadronic binding energy (to everything)		$\sim 0\%$			$\sim 0\%$
(b) Intrinsic mass values					
Caber	1	3	4	7	S
	Intrinsic mass (MeV)				
Uncharged	70.0	210.0	280.0	... ^d	... ^d
Singly charged	74.6	214.6	284.6	494.6	330.6
Doubly charged	... ^d	... ^d	289.2	499.2	336.9

^a The kaon is an exception. ^b See Fig. 2. ^c See Sec. III. ^d Not observed.

TABLE III. Rules for hadron resonance formation as clusters of cabers.

- (1) Nonstrange pseudoscalar mesons are formed as hadronically-bound strange caber-anticaber pairs: $\pi = 1\bar{1}$, $\eta = 4\bar{4}$, $(M, \eta', \delta^0) = 7\bar{7}$.
- (2) Strange pseudoscalar mesons are single (unbound) strange cabers or anticabers: $K = 7$ and $\bar{K} = \bar{7}$ are the only examples.
- (3) The nucleon is the hadronically bound Fermi-Yang^a spinor triplet $N = S\bar{S}\bar{S}$. Conservation of baryon number is precisely equivalent to the conservation of these triplets.
- (4) Metastable hyperon resonances are formed by adding strange anticabers $\bar{3}$ and $\bar{4}$ to an existing $S\bar{S}\bar{S}$ nucleon core: $\Lambda = S\bar{S}\bar{S}\bar{3}$, $\Sigma = S\bar{S}\bar{S}\bar{4}$, $\Xi = S\bar{S}\bar{S}\bar{3}\bar{3}$, $\Omega = S\bar{S}\bar{S}\bar{3}\bar{4}$.
- (5) Short-lived baryon and hyperon resonances are formed by adding nonstrange cabers $\dot{3}$ and $\dot{4}$ to the metastable "ground states" N , Λ , Σ , and Ξ : $N3, N4, N33, N44, \Lambda3, \Lambda4, \Lambda33, \Lambda44, \Sigma3, \Sigma4, \Sigma33, \Sigma34, \Sigma44, \Xi3, \Xi4$, etc. (see Fig. 16).
- (6) Short-lived meson resonances are formed by adding nonstrange excitation quanta to an $\bar{S}\bar{S}$ spinor pair: $\omega = \bar{S}\bar{S}\dot{\pi}$, $\phi = 3\bar{S}\bar{S}\pi$, $D = 3\bar{S}\bar{S}\dot{3}$, $E = 3\bar{S}\bar{S}\dot{4}$, etc. (see Fig. 19).
- (7) Broad-width baryon and meson resonances ($\Gamma \sim 100$ MeV) are interpretable as rotational excitations, with the S -state resonances of rules (5) and (6) serving as bandheads.^b The S -state resonances of rules (1)–(4) do not have overlying rotational bands.

^a See Ref. 4. ^b See Ref. 1.

TABLE IV. Distinctive feature of light-quark hadron resonances which are uniquely accounted for by the *linear* caber structures of Fig. 2.

Hadronic binding energies

(1) If the observed pseudoscalar bosons are compared to a 70-MeV mass grid, it is apparent (see Fig. 5) that (a) the π , η , and M , η' , δ^0 resonances have binding energies that are proportional to their masses, (b) the kaons appear to be unbound.

(2) The strange anticabers $\bar{3}$, $\bar{4}$, and $\bar{7}$ all bind to the $S\bar{S}$ spinor core with the same binding energy: -30 MeV (see Figs. 3 and 4).

(3) In multiple-strangeness excitations, the first anticaber binds with -30 MeV, the second binds with -15 MeV, and the third with ~ 0 MeV (see Fig. 4).

(4) The calculations of the $\bar{p}n$ and hyperon masses in Figs. 11–15 all assume that these caber clusters are coplanar; this coplanarity implies that the cabers have essentially cylindrical (linear) geometries with respect to hadronic binding energies.

Other hadron properties

(5) The K^0 - K^\pm mass difference, which is 4.0 MeV instead of 4.6 MeV, implies a length for the K^0 of at least 2.4 F (see Fig. 9).

(6) The calculated Coulomb corrections for the baryon and hyperon resonances of Figs. 10–15 accurately reproduce the observed n - p , Σ^- - Σ^0 - Σ^+ , and Ξ^- - Ξ^0 charge splittings; this suggests that the linear displacements assumed for the internal Coulomb charges must be approximately correct.

(7) The mechanical and electromagnetic properties of the spinor S which are derived in Appendix B are based on a linear array of three subquanta M_s .

The mass calculations for the resonances of Figs. 5–9 are summarized in Table VI. In making these calculations, we have used a total of five numerical parameters—the masses M^0 and M^\pm , the binding energy $B_{M\bar{M}}$, and the radii R_{\max} and R_{\min} for the Coulomb corrections—and we have reproduced the masses of the nine resonances in Table VI to an average absolute accuracy of better than 0.5 MeV, using a 70-MeV mass quantum as the fundamental building block. This is the strongest argument that we can give for the reality of this spinless light-quark basis state (which does not appear in the conventional quark model). In assessing the results shown in Table VI, the absence of any counterexamples should be stressed; all of the observed low-mass $J^P = 0^-$ bosons are

included here.

Figure 10 describes the nucleons. Since these are spinor triplets $S\bar{S}$ in which there are two hadronic $S\bar{S}$ bonds but no hadronic SS bond, the triplets can occur either as linear arrays or as clusters, depending on the electromagnetic potentials; and as shown in Fig. 10, the proton appears as a linear array and the neutron as a cluster. These configurations reproduce the masses, charge splitting, spins, and magnetic moments of the nucleons, as well as the zero electric dipole moments with respect to the spin axes. As discussed in paper I, these configurations reproduce the rms electric and magnetic radii for the nucleons; also, if the charge distributions are assumed to be equatorial current loops, then these

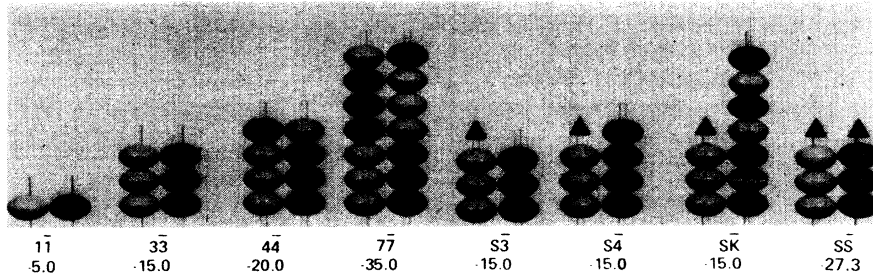


FIG. 3. Hadronic binding energies between caber-anticaber pairs. The hadronic binding, which from its $\sim 4\%$ magnitude is very short-ranged, operates directly between matching M and \bar{M} subquanta in adjacent cabers. Denoting these subquanta as M (nonspinning) and M_s (spinning), the hadronic binding energies between subquanta are as follows: $M\bar{M} = -5.0$ MeV, $M\bar{M}_s = \bar{M}M_s = -5.0$ MeV, $M_s\bar{M}_s = -9.1$ MeV, $M\bar{M} = \bar{M}M = M\bar{M}_s = \bar{M}_sM_s = M_s\bar{M}_s = \bar{M}_sM_s = 0$. As shown in the figure, the corresponding caber-anticaber binding energies in MeV are as follows: $\bar{1}\bar{1} = -5.0$, $\bar{3}\bar{3} = -15.0$, $\bar{4}\bar{4} = -20.0$, $\bar{7}\bar{7} = -35.0$, $S\bar{3} = S\bar{4} = S\bar{7} = -15.0$, $S\bar{S} = -27.3$, $SS = \bar{S}\bar{S} = 0$. The mass proportionality of the $\bar{1}\bar{1}$, $\bar{3}\bar{3}$, $\bar{4}\bar{4}$, and $\bar{7}\bar{7}$ binding energies and the equality of the $S\bar{3}$, $S\bar{4}$, and $S\bar{7}$ binding energies are both phenomenologically required features, and they seem to follow uniquely from the linear caber configurations shown here.

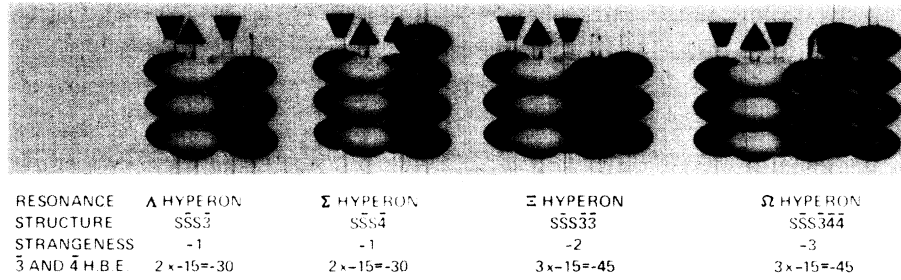


FIG. 4. Hadronic binding energies for clusters of spinless anticabers added to a nucleon core. Due to the very short range of the $\sim 4\%$ hadronic binding energies, only adjacent caber-anticaber pairs in a cluster can bind hadronically. When adding spinless anticabers to an $S\bar{S}\bar{S}$ -triplet nucleon core to form a hyperon resonance, the first $\bar{3}$ or $\bar{4}$ binds with two spinors S to give HBE = -30.0 MeV, the second $\bar{3}$ binds with only one spinor S to give HBE = -15 MeV, and the third anticaber, from its position in the excitation cluster, binds with essentially zero binding energy. As discussed in Fig. 2, the spinless anticabers carry the strangeness quantum numbers of the hyperon resonance. Experimentally, anticabers $\bar{3}$ and $\bar{4}$ will bind to an $S\bar{S}\bar{S}$ nucleon spinor core to produce Y^* resonances, but cabers 3 and 4 will not bind to this same spinor core to produce Z^* resonances. Thus the particle-antiparticle asymmetry that is inherent in the nucleon spinor core leads to observable consequences. In the present light-quark approach to particle structure, the Fermi-Yang (Ref. 4) formulation of the nucleon, $N = S\bar{S}\bar{S}$, is required, rather than the Gell-Mann and Zweig (Ref. 5) formulation, $N = SSS$.

current loops can account for the behavior of electromagnetic form factors in appearing like dipoles at low energies and like point charges (partons) at high energies, depending on whether the incident particle wavelength is large or small as compared to the dimensions of the current loops. In Appendix B it is shown that these spinor triplets give an average nucleon volume that is in agreement with the nucleon volume obtained from optical-model calculations for heavy nuclei.

Figure 11 shows the $\bar{p}n$ bound state. The calculation given here represents the only quantitative explanation of which the author is aware for this $\bar{p}n$ binding energy of -83.3 ± 1.4 MeV. In particular, potential model calculations of the $\bar{p}n$ system have great difficulty in reproducing the narrow width ($\Gamma \leq 8$ MeV) of the resonance. The $\bar{p}n$ bound state is a remarkable experimental result in that it gives us for the first time direct evidence that binding energies as large as 4% exist in nature. As was discussed in paper I, nucleon-nucleon and nucleon-antinucleon binding energies are analogous to the quark-quark binding energies that appear in the present light-quark model.

Figures 12–15 illustrate the metastable hyperon resonances. From the observed mass intervals, and also from the magnetic moments, it is clear that these are formed as combinations of spinless basis states combined with an $S\bar{S}\bar{S}$ nucleon core. From the systematics of both the meson and baryon resonances, it is apparent that the spinless excitation quanta carry the strangeness quantum numbers. This light-quark representation for the hyperons, in addition to reproducing the masses and quantum numbers, establishes a direct relationship between internal particle-antiparticle

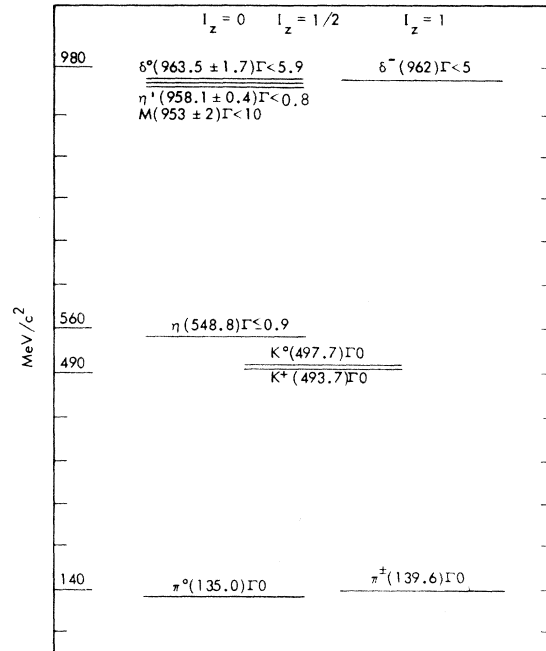


FIG. 5. An energy-level diagram for the pseudoscalar boson resonances, plotted with 70-MeV mass intervals. Experimentally, all of these resonances except the δ^0 have been measured to be $J^P = 0^-$ levels. The position of the M as the lowest member of the (M, η', δ^0) multiplet suggests that it is the fundamental member of this group—a suggestion that is borne out by the mass calculations of Figs. 7 and 8 and the production and decay modes summarized in Table V. As can be seen by the 70-MeV mass grids, the π , η , and (M, η', δ^0) resonances have small binding energies that are proportional to the masses, whereas the K mesons appear to be unbound. The δ^- , a charged form of the η' , is discussed in Fig. 8. Experimental evidence for these levels is discussed in Appendix A. The isotopic-spin labels are discussed in Ref. 6.

TABLE V. A summary of arguments which indicate that the M meson is the fundamental ground-state member of the $M(953)$, $\eta'(958)$, $\delta^0(963)$ multiplet.

- (1) As shown in Fig. 5, the M is the lowest-mass member of the multiplet.
 (2) The mass calculations of Fig. 7 pinpoint the M as the most strongly bound (and therefore most symmetric) resonance.
 (3) The M meson is observed in the symmetric reactions

- (a) $p + d \rightarrow \text{He}^3 + M$ (Ref. 7),
 (b) $K^- + p \rightarrow K^- + p + M$ (Ref. 8),

which do *not* show the η' or δ^0 resonances, whereas the η' has been observed in the asymmetric reaction

- (c) $K^- + p \rightarrow \Lambda + \eta'$ (Ref. 8),

which does *not* show the M , and the δ^0 has been observed in the charge-exchange reaction

- (d) $\pi^- + p \rightarrow \delta^0 + n$ (Ref. 9),

which shows an η' signal but no M signal. The symmetric reactions (a) and (b), in which the M is created directly from kinetic collision energy, require that the M have perfect internal particle-antiparticle symmetry, and hence a hadronic binding energy of -35 MeV (Fig. 8).

- (4) The M has the symmetric one-step decay process

- (e) $M \rightarrow \pi\pi\gamma$ ($\sim 100\%$) (Ref. 8),

whereas the η' has the asymmetric two-step decay process

- (f) $\eta' \rightarrow \rho\gamma$, $\rho \rightarrow \pi\pi$ ($\sim 100\%$).

Appendix A contains equations for the production and decay reactions shown here. These equations bring the symmetry characteristics of reactions (a)–(f) more sharply into focus.

symmetries and strangeness quantum numbers. It also shows that baryon number conservation is identical with the conservation of $S\bar{S}\bar{S}$ nucleon spinor triplets. The mapping problem as to why just these particular hyperons are produced, and not for example $\Xi' = S\bar{S}\bar{S}\bar{4}$, is discussed in Appendix D. The Σ^- (Ref. 11) and Ξ^- (Ref. 12) magnetic moments are discussed in the captions of Figs. 13 and 14, respectively. The Ω^- mass shown in the caption to Fig. 15 is from Ref. 13.

The baryon and hyperon caber cluster calculations of Figs. 10–15 are summarized in Table VII. The one resonance included in Table VII which is not shown in the figures is the K^-p bound state $\Lambda(1402)S$. We can calculate the mass of the K^-p bound state immediately by noting that this $p7^-$ excitation is directly analogous to the $p4^-$ excitation that constitutes the Σ^0 resonance. Thus the $\Lambda(1402)$ should have a mass that is just $3 \times 70.0 = 210.0$ MeV above the Σ^0 mass. The actual mass difference (see Figure 15) is 209.9 MeV. In Table VII we followed the less accurate procedure of calculating the $\Lambda(1402)$ mass directly from the $S\uparrow S\uparrow S\uparrow 7^-$ cluster of cabers. In line with these calculations, it is interesting to note that the decay of the $\Lambda(1402)$ resonance is 100% into Σ resonances, and not into the $\Lambda(1116)$ resonance (which has a spinor-flipped spinor core configuration).

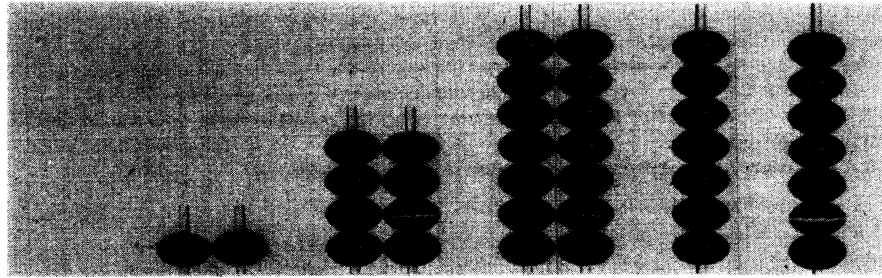
The average calculated absolute mass accuracy for the eleven resonances shown in Table VII is

$\pm 0.12\%$, or ± 1.6 MeV. In assessing the physical content of this result, several factors should be noted in addition to just the number of numerical parameters contained in the model: (1) The basic building blocks for these resonances are very large—a spinor $S \sim 330$ MeV and two spinless cabers $3 \sim 210$ MeV and $4 \sim 280$ MeV; (2) these



RESONANCE	π^-	π^0	π^+
UNBOUND MASS	144.6	140.0	144.6
HADRONIC B. E.	-5.0	-5.0	-5.0
BOUND MASS	139.6	135.0	139.6
EXPER. MASS	139.6	135.0	139.6

FIG. 6. The π mesons. The M^0 , \bar{M}^0 , and M^\pm mass values of Fig. 1 and the $M\bar{M}$ binding energy of Fig. 3 are adjusted so as to precisely reproduce the pion mass values. A stringent test of this phenomenology is to then use these same parameters to reproduce the higher-mass resonances, since any systematic errors will scale with the resonance masses. As is shown in Figs. 7–9, the parameters that accurately reproduce the pion masses also accurately reproduce the masses of the higher-mass resonances of Fig. 5. The caber pairs shown here also reproduce the strangeness quantum number $S=0$ and the spin $J=0$ of the pion. Phenomenologically, it seems to be correct that every hadronic resonance must contain at least one neutral quantum M^0 or M_s^0 . If we postulate this as a requirement for the π mesons, then we have also reproduced the isotopic spin $I=1$ of the pion multiplet.



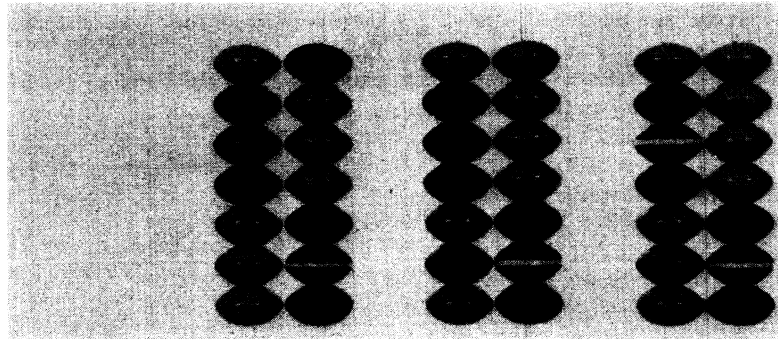
RESONANCE	PI MESON	ETA MESON	M MESON	K ⁺ MESON	K ⁻ MESON
STRUCTURE	11	44	77	7	7
STRANGENESS	0	0	0	+1	-1
UNBOUND MASS	140	569	989	495	495
HADRONIC B.E.	-5	-20	-35	0	0
COULOMB CORR.	0	-1	-1	0	0
BOUND MASS	135	548	953	495	495
EXPER. MASS	135	549	953	494	494

FIG. 7. The pseudoscalar bosons π , η , M , and K^\pm , members of the pseudoscalar nonet. As can be seen, the parameters that reproduced the pion masses in Fig. 6 also reproduce the masses of these resonances. Furthermore, the mass calculation singles out the M meson as the fundamental member of the M, η', δ^0 multiplet, in agreement with the results of Figs. 5 and 8 and with the systematics shown in Table V. The Coulomb corrections used here were obtained from parameter (10) in Table I: $R_{\max}^2 \approx 0.6 \text{ F} \rightarrow e^2/2R_{\max} \approx -1 \text{ MeV}$, a result that is essentially independent of any specific choice made for the internal + and - charge distributions in the subquanta M^+ and M^- . The Caber charge assignments $\eta = 4^+ 4^-$, $M = 7^+ 7^-$, $K^+ = 7^+$, and $K^- = 7^-$ shown here are in agreement with the rule for Coulomb self-energies given at the bottom of Table I.

same basis states also appear in other resonances, for example in the resonances of Table VI; (3) the absolute mass of each particle is a delicate balance among three kinds of binding energy—hadronic, magnetic, and Coulomb—and the magnetic and Coulomb binding energies are constrained

by the requirements of reproducing spins, magnetic moments, charge splittings, and total charges; (4) there are no counterexamples—all of the observed long-lived baryon and hyperon resonances are included here.

Table VIII summarizes all of the calculations of



RESONANCE	M MESON	η' MESON	δ^- MESON
PRODUCTION PROCESS	A·B·A·B·RES	A·B·C·RES	A·B·A·RES
UNBOUND MASS	989	989	994
HADRONIC B.E.	-35	-30	-30
COULOMB CORR.	-1	-1	-1
BOUND MASS	953	958	963
EXPER. MASS	953	958	962

FIG. 8. The $M(953)$, $\eta'(958)$, and $\delta^-(962)$ mesons. The symmetric production mode $A + B \rightarrow A + B + M$ mandates that the M , which is created directly from kinetic collision energy, must have perfect internal particle-antiparticle symmetry, and hence a binding energy of -35 MeV . The asymmetric production mode of the η' , on the other hand (see Table V), suggests a particle-antiparticle "defect," an unmatched MM pair, which shifts the mass upwards by 5 MeV . This asymmetry also relates to the decay modes of the M and η' resonances, as is shown in Table V. The $M(953)$, $\eta'(958)$, $\delta^0(963)$ fine structure is a direct experimental indication of the 5-MeV internal MM binding energy that was invoked initially to explain the pion masses of Fig. 6. The δ^- appears here naturally as a charged form of the η' . From the Coulomb rule at the bottom of Table I, this charged state is formed by adding a charge, so that $\delta^- = 7^+ 7^-$. The 7^+ caber shown here in the δ^- can also be observed singly as the K_L^0 meson of Fig. 9.

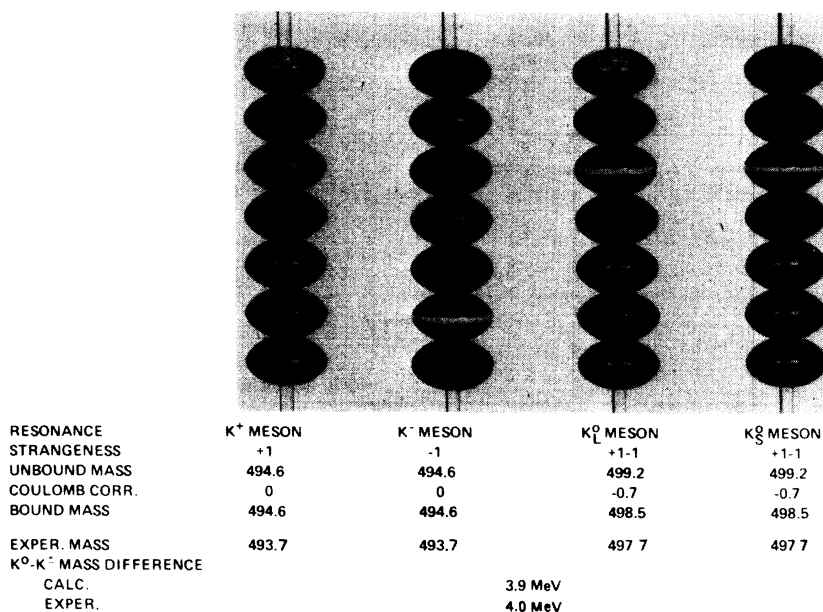


FIG. 9. The K mesons. The configurations shown here reproduce the absolute mass values, the charged splitting of the masses, and the strangeness characteristics. The $K^\pm = 7^\pm$ mesons were shown in Fig. 7. The $K_L^0 = 7^{+-}$ caber also appears in the δ^- resonance of Fig. 8; the K_S^0 is a more symmetric form of the 7^{+-} caber, and it has a $\pi\pi$ decay mode as compared to the $\pi\pi\pi$ decay mode of the K_L^0 . As is shown in Fig. 23 of Appendix A, these kaon configurations also have phenomenological significance with respect to the lifetimes of these resonances. From the calculation of the K^0-K^\pm mass difference, the Coulomb correction in the K^0 must be -0.6 MeV (the value of -0.7 MeV shown here is from the radius $R_{\min} \approx \frac{1}{3} F$ given in Table I). Thus the K^0 charge separation must be $e^2/R^\pm = -0.6$ MeV $\rightarrow R^\pm = 2.4 F$. This large value for R^\pm is one of the main reasons for selecting a linear structure to represent the kaon. The conventional quark model predicts unambiguously (Ref. 10) that the K^\pm meson should be heavier than the K^0, \bar{K}^0 meson, so the present light-quark systematics offers a resolution of this long-standing theoretical puzzle. The kaon configurations shown here are $K^\pm = 3^+4^0, K_L^0 = 3^+3^-1^0$, and $K_S^0 = 3^+4^-$, so that K^\pm have strangeness ± 1 and K_L^0 and K_S^0 have mixed strangeness, as observed experimentally. The K_S^0 regeneration process, a secondary scattering, is a geometrical rearrangement of the K_L^0 structure.

TABLE VI. Calculation of mass values for the very-narrow-width boson resonances. The rules for reconstructing these resonances are given in Tables I–III. These resonances are illustrated in Figs. 5–9.

Boson	Caber array	Intrinsic	Binding energies		Observed mass		
		mass	(MeV)		(MeV)		
		(MeV)	Hadronic	Coulomb	Calc.	Exper.	Error
π^\pm	$1^0 1^\pm$	144.6	-5.0		139.6	139.6	0.00%
π^0	$1^0 \bar{1}^0$	140.0	-5.0		135.0	135.0	0.00%
η	$4^+ 4^-$	569.2	-20.0	-1.2	548.0	548.8 ^a	-0.15%
M	$7^+ 7^-$	989.2	-35.0	-1.2	953.0	953	0.00%
η'	$7^+ 7^-$	989.2	-30.0	-1.2	958.0	958.1	-0.01%
δ^0	$7^+ 7^-$	989.2	-25.0	-1.2	963.0	963.5	-0.05%
δ^-	$7^+ \bar{7}^-$	993.8	-30.0	-1.3	962.0	962	+0.05%
K^\pm	7^\pm	494.6	0		494.6	493.7	+0.18%
K^0, \bar{K}^0	7^{+-}	499.2	0	-0.7	498.5	497.7	+0.16%

Average percentage mass accuracy $\pm 0.07\%$

Average absolute mass accuracy ± 0.4 MeV

^a A recent measurement [D. M. Binnie *et al.*, Phys. Rev. D **8**, 2789 (1973)] gives the η mass as 548.1 ± 0.4 MeV.

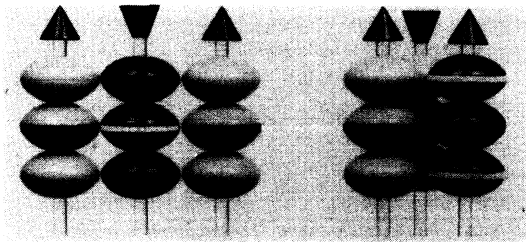


FIG. 10. The proton and neutron. These are both formed as Fermi-Yang (Ref. 4) spinor clusters $N = \bar{S}\bar{S}\bar{S}$. The internal charge assignments for the nucleons follow uniquely from the requirement of reproducing the following experimental data: the total charges, the magnetic moments, the spins, the mass difference, and the zero electric dipole moment for the neutron about its spin axis. From their resultant electromagnetic interactions, the proton appears with a linear $\bar{S}\bar{S}\bar{S}$ configuration and the neutron with a clustered $\bar{S}\bar{S}\bar{S}$ configuration. The nucleon values that are reproduced from the parameters of Table I are the following:

	Proton	Neutron
Spinor configuration	$S\uparrow S\uparrow S\uparrow$ (linear)	$S\uparrow S\downarrow S\uparrow$ (clustered)
Intrinsic mass (MeV)	991.8	998.1
hadronic binding energy	-54.6	-54.6
magnetic binding energy	+3.4	-1.7
Coulomb binding energy	-2.2	-2.1
Calculated mass	938.4 MeV	939.7 MeV
Experimental mass	938.4 MeV	939.6 MeV
Calculated magnetic moment	+2.79 μ_N	-1.86 μ_N
Experimental magnetic moment	+2.79 μ_N	-1.91 μ_N

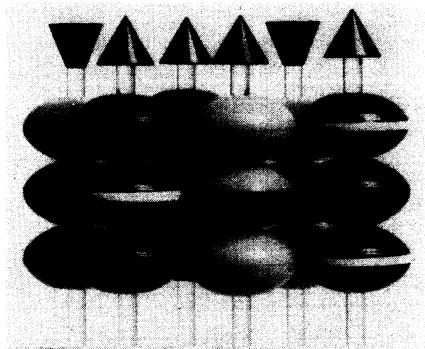


FIG. 11. The $\bar{p}n$ bound state. The same parameters that reproduce the proton and neutron also reproduce the $\bar{p}n$ bound state. The $\bar{p}n$ cluster shown here is a spin-1 configuration, as suggested by the experimental data.

Spinor configuration	$S\uparrow S\uparrow S\uparrow S\uparrow S\downarrow S\uparrow$
Intrinsic mass (MeV)	1989.9
hadronic binding energy	-191.1
magnetic binding energy	+1.7
Coulomb binding energy	-5.6
Calculated mass	1794.9 MeV
Experimental mass	1794.5 \pm 1.4 MeV

The Coulomb corrections for Figs. 10-15 are discussed in Sec. IV and summarized in Table I.

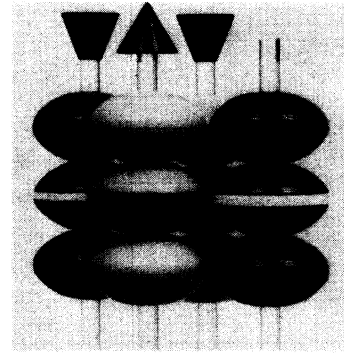


FIG. 12. The Λ hyperon. The Λ is the caber cluster $\bar{S}\bar{S}\bar{S}$, in which the anticaber \bar{S} carries the strangeness quantum number $S = -1$. Calculated values for the Λ are the following:

Caber configuration	$S\uparrow S\uparrow S\uparrow \bar{S}$
Intrinsic mass (MeV)	1206.4
hadronic binding energy	-84.6
magnetic binding energy	-1.7
Coulomb binding energy	-3.2
Calculated mass	1116.9 MeV
Experimental mass	1115.6 MeV
Calculated magnetic moment	-0.93 μ_N
Experimental magnetic moment	(-0.67 \pm 0.06) μ_N

the present section. Starting with the ten numerical parameters of Table I, and using them in the manner outlined in Tables I-III, we have reproduced or otherwise accounted for the absolute masses of twenty resonances to an average accuracy of $\pm 0.1\%$, or ± 1.0 MeV, taking into account the constraints of item (3) in the above paragraph plus the requirement of reproducing the strangeness quantum numbers. It might be argued that this geometric light-quark model has some built-in parameter freedom in addition to these ten numerical constants; however, it can also be argued that a number of these constants are in fact pinned down by the experimental data, as is discussed in Sec. IV.

It is instructive to compare the summary of results in Table VIII with the mass calculations that are obtained from symmetry schemes, using the discussion of these symmetry schemes by Feld¹⁴ as a guide. The standard baryon mass formula $\frac{1}{2}(M_{\Sigma} + M_{\Lambda}) = \frac{1}{4}(M_{\Sigma} + 3M_{\Lambda})$, which follows from the early Goldhaber model,¹⁵ requires three known masses to determine the fourth. Choosing all neutral masses, this formula gives the mass of the Ξ^0 , for example, to an accuracy of 1.2%. If this same Goldhaber formalism is applied to meson masses, it gives the equation $4M_K = 3M_{\eta} + M_{\pi}$. Using the K^0 and π^0 as input masses, the η mass is calculated to an accuracy of 13%. If the *ad hoc* assumption is then made that the squares

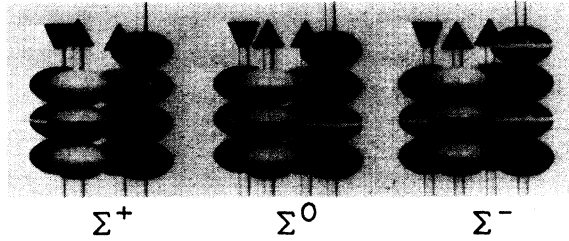


FIG. 13. The Σ hyperons. The Σ hyperons are caber clusters $\bar{3}_S \bar{3}_4$, in which the anticaber $\bar{4}$ carries the strangeness quantum number $S = -1$. The configurations shown here reproduce the masses and charge splittings correctly. The Σ^+ magnetic moment is correctly reproduced. The calculated Σ^- magnetic moment is in disagreement with a recent measurement (Ref. 11). The magnetic moment of the Σ^0 has not measured, but the Σ^0 cluster shown here and the Λ cluster of Fig. 12 correctly reproduce the Q value of the observed decay mode $\Sigma^0 \rightarrow \Lambda + \gamma$ (see Fig. 22).

	Σ^+	Σ^0	Σ^-
Caber configuration	$S\uparrow S\uparrow S\uparrow \bar{4}^0$	$S\uparrow S\uparrow S\uparrow \bar{4}^-$	$S\uparrow S\uparrow S\uparrow \bar{4}^-$
Intrinsic mass (MeV)	1271.8	1276.4	1281.0
hadronic binding energy	-84.6	-84.6	-84.6
magnetic binding energy	+5.1	+5.1	+5.1
Coulomb binding energy	-1.4	-3.2	-3.3
Calculated mass (MeV)	1190.9	1193.7	1198.2
Experimental mass (MeV)	1189.4	1192.5	1197.3
Calculated charge splitting (MeV)	2.8	4.5	
Experimental charge splitting (MeV)	3.1	4.8	
Calculated magnetic moment	$+2.79\mu_N$	$+2.79\mu_N$	$+2.79\mu_N$
Experimental magnetic moment	$(+2.59 \pm 0.46)\mu_N$...	$(-1.48 \pm 0.37)\mu_N$ (Ref. 11)

of masses should be used in this equation, the η mass is calculated to an accuracy of 6%. These Goldhaber mass equations do not work for other groups of meson resonances. In the SU(6) formalism, the η' meson can be added to the (π, K, η) group, but only at the expense of introducing an additional arbitrary mixing parameter, so that SU(6) has no real prediction for the $\eta'(958)$ mass [for example, the $E(1416)$ meson is sometimes considered to be the singlet member of this group]. Thus, with respect to the calculation of absolute resonance masses, the SU(6) formalism and its various antecedents give values for only two resonances out of the list of resonances shown in Table VIII—one baryon mass to an accuracy of $\sim 1\%$ and one meson mass to an accuracy of $\sim 6\%$ (or perhaps 13%). With respect to charge splittings, the SU(6) formalism, with the n - p , Σ^- - Σ^0 , and Σ^- - Σ^+ mass differences as input parameters, gives the Ξ^- - Ξ^0 mass difference correctly, but it gives the K^+ mass as being larger than the K^0

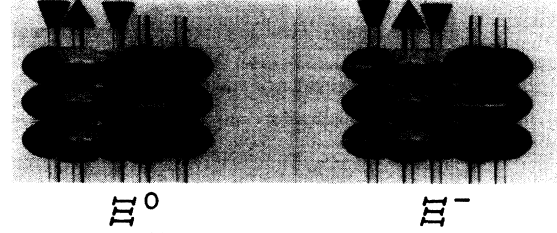


FIG. 14. The Ξ hyperons. The Ξ hyperons are the caber clusters

$$\bar{3}_S \bar{3}_3,$$

in which the two anticabers $\bar{3}\bar{3}$ carry the strangeness quantum $S = -2$. In order to reproduce the large charge splitting for this hyperon resonance, we must, as in the case of the proton and neutron, form the second charge state by using a doubly charged spinor S^- . This leads to the prediction that the Ξ^- and the neutron have comparable magnetic moments, in contrast to the SU(6) prediction that the Ξ^- and Λ have comparable magnetic moments. A recent experimental result (Ref. 12) is in agreement with the present prediction. The Ξ^0 magnetic moment is unknown.

	Ξ^0	Ξ^-
Caber configuration	$S\uparrow S\uparrow S\uparrow \bar{3}^- \bar{3}^0$	$S\uparrow S\uparrow S\uparrow \bar{3}^- \bar{3}^0$
Intrinsic mass (MeV)	1416.4	1422.7
hadronic binding energy	-99.6	-99.6
magnetic binding energy	-1.7	-1.7
Coulomb binding energy	-3.2	-3.3
Calculated mass	1311.9 MeV	1318.1 MeV
Experimental mass	1314.9 MeV	1321.3 MeV
Calculated charge splitting		6.2 MeV
Experimental charge splitting		6.4 MeV
Calculated magnetic moment	$-0.93\mu_N$	$-1.86\mu_N$
Experimental magnetic moment	...	$(-1.93 \pm 0.75)\mu_N$ (Ref. 12)

mass. If the $\pi^+ - \pi^0$ and $K^+ - K^0$ mass differences are instead used as input parameters, SU(6) then gives the wrong value for the n - p mass difference. Thus, while the unitary symmetry schemes give the IBY relationships (isotopic spin, baryon number, hypercharge) in a very striking manner, the calculation of absolute masses is not one of their main virtues. In this connection, it should be noted that the prediction of the Ω^- mass was based on a decimet interval rule with spacings of 140 MeV. As can be observed in Figs. 16 and 19, 140-MeV resonance spacings are a very common occurrence. Perhaps the most important point to bring out in this discussion is one that does not involve masses. This point is the fact that the existence of the $M, \eta', \delta^0, \delta^-$ resonance fine struc-

ture seems to be in contradiction with any results that we would expect to find on the basis of either unitary symmetry schemes or S -matrix approaches.

The very-narrow-width resonances of the present section are constructed entirely from strange cabers and anticabers. In Sec. III, we consider intermediate-width baryon and meson S -state resonances which include nonstrange cabers. In many respects, the systematics of the nonstrange excitations is considerably simpler than the systematics of the present section.

III. THE INTERMEDIATE-WIDTH S -STATE RESONANCES

In Figs. 12–15, we saw that hyperon resonances are formed by adding strange anticabers $\bar{3}$ and $\bar{4}$ to an $S\bar{S}\bar{S}$ nucleon spinor core: $\Lambda = S\bar{S}\bar{S}\bar{3}$, $\Sigma = S\bar{S}\bar{S}\bar{4}$, $\Xi = S\bar{S}\bar{S}\bar{3}\bar{3}$, and $\Omega = S\bar{S}\bar{S}\bar{3}\bar{4}\bar{4}$. In these hyperon excitations, the anticabers $\bar{3}$ and $\bar{4}$ carry strangeness quantum numbers $S = -1$, so that the excitations have different strangeness values than the $S\bar{S}\bar{S}$ nucleon ground state. The anticabers $\bar{3}$ and $\bar{4}$ have $\sim 4\%$ binding energies with the spinors S in the nucleon spinor core (see Figs. 3 and 4).

Figure 16 shows a different kind of baryon excitation. This figure is an energy-level diagram of the rotationless narrow-width and S -state baryon and hyperon resonances, with each resonance type grouped in a column (an “excitation tower”) above the corresponding metastable “ground state,” and with 70-MeV mass grids superimposed on the ground states. As can be seen, the resonances occur at accurate 70-MeV intervals above these ground states, so that the excitations are formed from 70-MeV quanta with essentially zero binding energy. Also, the excitation quanta are “nonstrange,” since the excited states have the same strangeness quantum numbers as the ground states. From the observed level spacings it can be seen, as shown in the column at the far left in Fig. 16, that these excitation quanta are formed as combinations of the (nonstrange) cabers $\bar{3}$ and $\bar{4}$. Thus *metastable* (very-narrow-width) hyperon resonances are formed by adding strange anticabers $\bar{3}$ and $\bar{4}$ to an $S\bar{S}\bar{S}$ “ground state,” with $\sim 4\%$ binding energies; and *intermediate-width* S -state baryon and hyperon resonances are formed by adding nonstrange cabers $\bar{3}$ and $\bar{4}$ to the “ground states” $S\bar{S}\bar{S}$, $S\bar{S}\bar{S}\bar{3}$, $S\bar{S}\bar{S}\bar{4}$, and $S\bar{S}\bar{S}\bar{3}\bar{3}$, with essentially zero binding energy.

As was discussed in paper I, the 3-type and the 4-type excitations, both strange and nonstrange, exhibit different symmetry properties. For example, the $N\bar{4}\bar{4}$, $\Lambda\bar{4}\bar{4}$, and $\Sigma\bar{4}\bar{4}$ excitations of Fig. 16 are dominant and easily observed S states.

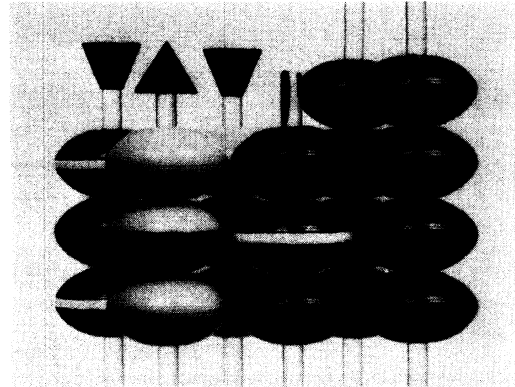


FIG. 15. The Ω^- hyperon. The Ω is the caber cluster

$$\begin{matrix} S\bar{S}\bar{S} \\ \bar{3}\bar{4} \\ 4 \end{matrix}$$

in which the three anticabers $\bar{3}\bar{4}\bar{4}$ carry the strangeness quantum number $S = -3$. The spin of the Ω has not been measured. Since the $\Omega^- - \Xi^-$ mass difference is 350.9 MeV, almost precisely equal to 5×70.0 MeV, we have assigned the Ω^- the same spinor-triplet configuration as the Ξ^- . In a similar pairing of resonances, the $\Lambda(1402.4) = p7^-$ and $\Sigma^0(1192.5) = p4^-$ resonances have a mass difference of 209.9 MeV, almost precisely equal to 3×70.0 MeV.

Caber configuration	$S\bar{S}\bar{S}\bar{3}\bar{4}\bar{4}^0$
Intrinsic mass (MeV)	1772.7
hadronic binding energy	-99.6
magnetic binding energy	-1.7
Coulomb binding energy	-3.3
Calculated mass	1668.1 MeV
Experimental mass	1672.2 MeV (Ref. 13)

whereas the $N\bar{3}\bar{3}$, $\Lambda\bar{3}\bar{3}$, and $\Sigma\bar{3}\bar{3}$ excitations are, respectively, an unobserved $N(1359)$ bandhead, the narrow-width $J = \frac{3}{2}$ $\Lambda(1518)D$ resonance (which is not a D state), and the controversial $\Sigma(1620)S$ resonance (which was identified as an S state on the basis of the present systematics before it was verified as such experimentally). Figure 17 shows strange and nonstrange forms of the caber $\bar{3}-\bar{3}$, $\bar{3}, \bar{3}, \bar{3}$. Figure 18 illustrates the nonstrange excitation cluster $\bar{4}\bar{4}$,¹⁶ and also the three resonances mentioned above, $N\bar{4}\bar{4}$, $\Lambda\bar{4}\bar{4}$, and $\Sigma\bar{4}\bar{4}$, which are dominant baryon and hyperon S states.

Meson resonances form the same kind of nonstrange excitations as baryons, but with two differences: (1) The ground state for the meson excitations is the very difficult to observe $\bar{S}\bar{S}$ nonstrange spinor pair (which is related to the even more difficult to observe $J^P = 2^+ \bar{S}\bar{S}\bar{S}\bar{S}$ spinor quartet that causes the interference effects in the A_2 meson); (2) nonstrange meson excitation quanta include, in addition to the nonstrange cabers $\bar{3}$ and

TABLE VII. Reconstruction of the metastable baryon and hyperon resonances and the $\bar{p}n$ and $\bar{K}p$ bound states according to the rules of Tables I–III. The configurations shown here reproduce masses, spins, charge splittings, strangeness quantum numbers, and magnetic moments. The average calculated absolute mass accuracy is $\pm 0.12\%$, or ± 1.6 MeV.

Name	Resonance cluster ^a	Intrinsic mass	Binding energies			Final mass values			S^b	μ^c
			Hadronic	Magnetic	Coulomb	Calc.	Exper.	Error		
p	$S^{\dagger}S^{\dagger}S^{\dagger}$	991.8	-54.6	+3.4	-2.2	938.4	938.3	+0.01%	0	+3
n	$S^{\dagger}S^{\dagger}S^{\dagger}$	998.1	-54.6	-1.7	-2.1	939.7	939.6	+0.01%	0	-2
Λ	$S^{\dagger}S^{\dagger}S^{\dagger}3^{-}$	1206.4	-84.6	-1.7	-3.2	1116.9	1115.6	+0.12%	-1	-1
Σ^{+}	$S^{\dagger}S^{\dagger}S^{\dagger}4^0$	1271.8	-84.6	+5.1	-1.4	1190.9	1189.4	+0.13%	-1	+3
Σ^0	$S^{\dagger}S^{\dagger}S^{\dagger}4^{-}$	1276.4	-84.6	+5.1	-3.2	1193.7	1192.5	+0.10%	-1	+3
Σ^{-}	$S^{\dagger}S^{\dagger}S^{\dagger}4^{--}$	1281.0	-84.6	+5.1	-3.3	1198.2	1197.3	+0.08%	-1	+3
Ξ^0	$S^{\dagger}S^{\dagger}S^{\dagger}3^{-}3^0$	1416.4	-99.6	-1.7	-3.2	1311.9	1314.9	-0.23%	-2	-1
Ξ^{-}	$S^{\dagger}S^{\dagger}S^{\dagger}3^{-}3^0$	1422.7	-99.6	-1.7	-3.3	1318.1	1321.3	-0.24%	-2	-2
Ω^{-}	$S^{\dagger}S^{\dagger}S^{\dagger}3^{-}4^0 4^0$	1772.7	-99.6	-1.7	-3.3	1668.1	1672.2	-0.25%	-3	-2
$\bar{p}n$	$S^{\dagger}S^{\dagger}S^{\dagger}S^{\dagger}S^{\dagger}S^{\dagger}$	1989.9	-191.1	+1.7	-5.6	1794.9	1794.5	+0.02%	0	-5
$K\bar{p}$	$S^{\dagger}S^{\dagger}S^{\dagger}7^{-}$	1486.4	-84.6	+5.1	-3.2	1403.7	1402.4	+0.09%	-1	+3

Charge splittings				
	$n-p$	$\Sigma^0-\Sigma^{+}$	$\Sigma^{-}-\Sigma^0$	$\Xi^{-}-\Xi^0$
Calculated	1.3 MeV	2.8 MeV	4.5 MeV	6.2 MeV
Experimental	1.3 MeV	3.1 MeV	4.8 MeV	6.4 MeV

^a See Figs. 10–15. ^b Strangeness quantum number. ^c Approximate magnetic moment (see Tables I and VIII).

4 observed in the baryon excitations, the non-strange excitation unit $\pi = 1^0\bar{1}^0$, which does not play a role in the baryon resonances. With these three types of excitation— $\pi, \bar{3}, \bar{4}$ —intermediate-width S -state meson resonances can and do occur essentially every 70 MeV, as is shown in Fig. 19. An excitation symmetry scheme for mapping these resonances was given in paper I.

Strange and nonstrange forms of the spinor $S-S, \bar{S}, \bar{S}, \bar{S}$ —are shown in Fig. 20. As was explained in the caption to Fig. 2, the strange spinors S and \bar{S} occur only in nucleon spinor triplets SSS and antitriplets $\bar{S}\bar{S}\bar{S}$, which are invariants in associated-production reactions. Thus these “strange” spinors do not contribute to the conventional strangeness quantum numbers. The non-strange spinors \bar{S} and \bar{S} occur only pairwise and only in meson and kaon resonances. Although the $\bar{S}\bar{S}$ pair by itself is very difficult to observe as an S -state resonance, it appears prominently in rotational levels as the bandhead of the broad-width $\rho(1P_1)$ and $\epsilon(3P_0)$ meson resonances.²

Figures 16 and 19 contain a total of 34 intermediate-width S -state resonances, including the $\Lambda(1402)$ resonance of Table VII. Theoretical cal-

culations for the masses of these resonances consist simply of the mass values given by the 70-MeV mass grids erected on the $\bar{S}\bar{S}, N, \Lambda, \Sigma,$ and Ξ “ground states.” Table IX summarizes the mass accuracies that are obtained for these resonances. It is also shown in Table IX that the probabilities for random spacings rather than 70-MeV spacings in Figs. 16 and 19 are vanishingly small. As with Tables VI and VII, we stress the completeness of the resonance mappings in Figs. 16 and 19—all of the observed S -state and intermediate-width resonances are included. The linear systematics of Figs. 16 and 19 have led to a number of predictive successes. These are summarized in paper I. Figure 21 shows hyperon resonances from Fig. 16 plotted against the $p(938)$ “ground state.” It illustrates the $\sim 4\%$ binding energies for strange excitations as compared to the $\sim 0\%$ binding energies for nonstrange excitations.

IV. EXPERIMENTAL, PHENOMENOLOGICAL, AND THEORETICAL DETERMINATIONS OF THE LIGHT-QUARK PARAMETER VALUES

In the present section we summarize information that can be used to determine parameter values

TABLE VIII. A summary of hadron particle properties that are accounted for by the ten-parameter light-quark model of Tables I–III. Twenty absolute masses and strangeness quantum numbers, nineteen spins, five magnetic moments, and four charge splittings are accurately reproduced. The only difficulty is with a recent measurement of the Σ^- magnetic moment (Ref. 11). As discussed in the text, SU(6) gives only two of these absolute masses as calculated values: one baryon mass ($\pm 1\%$) and one meson mass ($\pm 6\%$).

Particle	Absolute mass accuracy		Magnetic moment				Where described
	Percent	MeV	Spin	Strangeness	Calc.	Measured	
π^0	0.00%	0.0	0	0			Fig. 6
π^\pm	0.00%	0.0	0	0			Fig. 6
K^\pm	0.18%	0.9	0	1			Fig. 9
K_L^0, K_S^0	0.16%	0.8	0	mixed			Fig. 9
η	0.15%	0.8	0	0			Fig. 7
M	0.00%	0.0	0	0			Fig. 8
η'	0.01%	0.1	0	0			Fig. 8
δ^0	0.05%	0.5	0	0			Appendix A
δ^-	0.05%	0.5	0	0			Fig. 8
p	0.01%	0.1	$\frac{1}{2}$	"0" ^a	+2.79	+2.793	Fig. 10
n	0.01%	0.1	$\frac{1}{2}$	"0" ^a	-1.86	-1.913	Fig. 10
Λ	0.12%	1.3	$\frac{1}{2}$	-1	-0.93	-0.67 \pm 0.6	Fig. 12
Σ^+	0.13%	1.5	$\frac{1}{2}$	-1	+2.79	+2.59 \pm 0.46	Fig. 13
Σ^0	0.10%	1.2	$\frac{1}{2}$	-1	+2.79		Fig. 13
Σ^-	0.08%	0.9	$\frac{1}{2}$	-1	+2.79 ^a	-1.48 \pm 0.37 ^b	Fig. 13
Ξ^0	0.23%	3.0	$\frac{1}{2}$	-2	-0.93		Fig. 14
Ξ^-	0.24%	3.2	$\frac{1}{2}$	-2	-1.86 ^b	-1.93 \pm 0.75 ^c	Fig. 14
Ω^-	0.25%	4.1	$\frac{1}{2}$ ^d	-3	-1.86		Fig. 15
$\bar{p}n$	0.02%	0.4	1	0	-4.65		Fig. 11
$\bar{K}p$	0.09%	1.3	$\frac{1}{2}$	-1	+2.73		Table VII
Average	$\pm 0.09\%$	± 1.0 MeV					

^a See Table II and Fig. 2.

^b The calculated value is in disagreement with a recent experiment (Ref. 11).

^c The calculated value is in agreement with experiment and in disagreement with SU(6).

^d This spin is not known experimentally.

for the ten-parameter light-quark basis set that is listed in the abstract and described in Table I.

A. The mass quantum $M^0 = 70.0$ MeV

Since the mass quantum M has not been observed experimentally, indirect methods must be used to ascertain its mass values. Table X lists eight determinations of the M^0 mass, based on properties of meson, kaon, hyperon, and lepton resonances. The first determination, $M^0(1033.6)$

– $\delta^0(963.5)$, is the energy difference between two narrow meson peaks noted by the same experimental group⁹ in the same type of experiment – $\pi^-p - X^0n$, with the η' peak available as a reference mass in both experiments. The second through fourth determinations are based on mass differences between well-established hyperon resonances. The fifth determination is based on the meson energy levels of Fig. 19, and it involves the $\bar{S}\bar{S}$ ground-state mass, which is discussed in

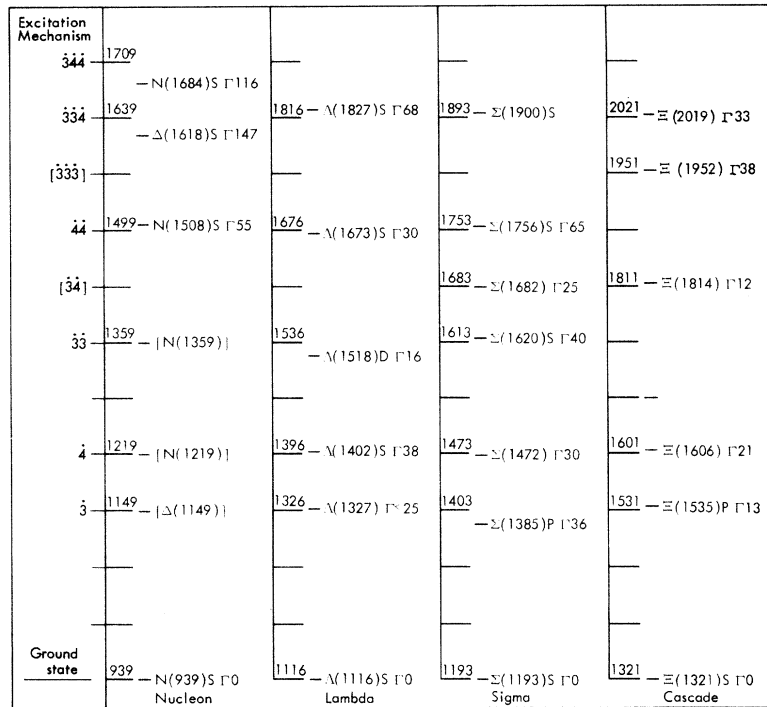


FIG. 16. Intermediate-width S-state baryon and hyperon resonances, arranged as “excitation towers” above the metastable N, Λ, Σ, and Ξ “ground states” (the three bracketed nucleon excitations are unseen bandheads that are identified by overlying rotational levels). As indicated in the column at the left, these excitations are formed as combinations of uncharged nonstrange cabers $\bar{3}$ and $\bar{4}$, which cluster with essentially zero binding energy. The mixed excitation $\bar{3}\bar{4}$ is weak, and the excitation $\bar{3}\bar{3}\bar{3}$ is inhibited because of competition with the transition $\bar{3}\bar{3}\bar{3} \rightarrow \bar{3}\bar{3}$ (see Appendix C). Figure 21 shows hyperon resonances from the present figure plotted against a nucleon “ground state.” The Ξ(1952) and Ξ(2019) resonances are from Rossi 73 in RPP74 (Ref. 25).

Table XI.

The sixth determination, the absolute mass of the K^+ , is of considerable phenomenological interest in that it gives a direct evaluation of the assumption that the quanta M^0 occur in linear cabers (in this case the caber 7^+) with essentially zero hadronic binding energy. From the value $M^0 = 69.9$ MeV obtained from the K^+ in Table X, we can set an upper limit on the intracaber binding energy of 0.1 MeV (in the present paper we neglect this binding energy).

The seventh and eighth determinations of the mass M^0 , the values obtained from the muon and from the electron, are shown mainly for their heuristic significance. The muon result is obtained from Appendix E. The electron result, a scaling of masses as a power of $\alpha = e^2/\hbar c$, is phenomenologically of interest when it is combined with the fact (Appendix A) that the lifetimes of the metastable particles also show a scaling in α (over a span of nine decades in α).

Since the attempt in the present paper is to obtain the simplest possible representation of the

hadronic basis set, the value $M^0 = 70.0$ MeV was selected as the consensus value from Table X and used as parameter (1) in Table I. If we break down the eight M^0 determinations of Table X into types, we obtain

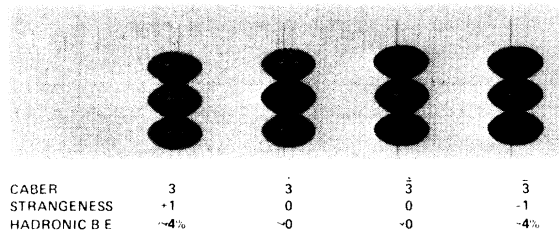


FIG. 17. Strange and nonstrange forms of the caber 3. Phenomenologically, the relationship between strangeness quantum numbers and binding energies that is established here is one of the most important results of the present systematics: strange quanta have HBE ~ 4%, and nonstrange quanta have HBE ~ 0%. These caber properties are summarized in Table II. In Sec. IV it is demonstrated experimentally that strange and nonstrange basis states have the same intrinsic masses.

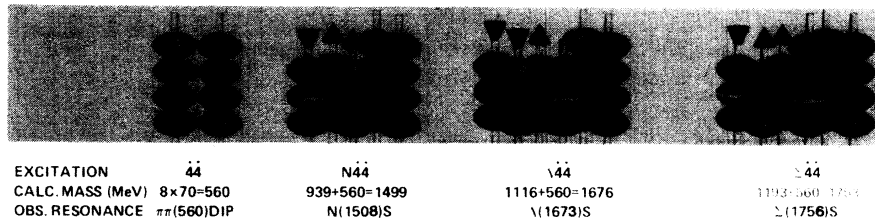


FIG. 18. The nonstrange caber pair $\bar{44}$, which appears with zero hadronic binding energy. Evidence for direct $\bar{44}$ = 560 MeV resonance effects in meson amplitudes is weak (Ref. 16), but the $N\bar{44}$, $\Lambda\bar{44}$, and $\Sigma\bar{44}$ resonances are dominant and easily observed baryon and hyperon S states. The mass values shown here indicate that the zero-binding-energy approximation for these excitations is accurate.

- (1) and (5) = mesons → 70.1 MeV and 69.8 MeV → 69.95 MeV,
- (2)–(4) = hyperons → 70.0, 70.2, and 69.7 MeV → 70.0 MeV,
- (6) = the kaon → → 69.9 MeV,
- (7) and (8) = leptons → 70.4 MeV and 70.0 MeV → 70.2 MeV.

Thus the quantum M^0 appears with essentially the same mass value in all types of resonant structure. We have not quoted experimental uncertainties in these determinations, because our goal is not to obtain a “best value” for M^0 , but rather a representative value that is applicable to all types of particle.

B. The mass quantum $M^\pm = 74.6$ MeV

The mass difference $M^\pm - M^0$ is set equal to the mass difference $\pi^\pm - \pi^0$. At present we have no way of calculating this Coulomb self-energy, but the fact that it is almost exactly equal to nine electron masses is probably not accidental, and it suggests that a simple (geometric) explanation may exist.

C. The mass quantum $S^\pm = 330.6$ MeV

Mass values for the spinning quark state S^\pm can be obtained from single quark phenomenology; from quark-pair,¹⁷ quark-triplet, and quark-quartet^{17–23} experimental data, and from the special-relativistic equations of Appendix B. These determinations are summarized in Table XI. Single spinors (quarks) S^\pm have not been observed, but we can deduce a spinor mass from the assumed¹⁴ quark magnetic moments and quark interaction ranges ($R \sim \hbar/mc$). These arguments were given in Table VIII of paper I, and they indicate an average nucleon quark mass of about 330 MeV.

The spinor-pair mass determination is based on the 658-MeV $\hat{S}^+\hat{S}^-$ ground state of the meson excitation tower of Fig. 19 (the mass value of about 658 MeV is obtained from Fig. 8 of Ref. 17). Since this spinor pair is seen only in $I = 0$ ampli-

tudes, it has spin $J = 1$ (from the I, J rule quoted in Fig. 20). Hence it has a magnetic binding energy of -1.7 MeV and a Coulomb binding energy of -1.4 MeV. Thus the corrected mass of the $\hat{S}^+\hat{S}^-$ pair is about 661 MeV, which gives an \hat{S}^\pm spinor mass of about 330.5 MeV.

The spinor-triplet determination is shown in Table XI, where the proton and $\bar{p}n$ masses, with small Coulomb corrections applied, are used to deduce the $S\bar{S}$ binding energy, and then to unbind the proton. The value obtained from this determination, $S^\pm = 330.6$ MeV, was used as parameter (3) in Table I.

The spinor-quartet mass determination is obtained by studying the position of the A_2 dip, which (from the present viewpoint) is an interference effect caused by the $J^P = 2^+ \hat{S}_1 \hat{S}_1 \hat{S}_1 \hat{S}_1$ state. Although a deeply split A_2 meson seems to be ruled out experimentally, a small interference effect still persists in a number of uncontroverted experiments, and always at the same location.²² Table XI gives a summary of these experiments,^{18–23} and it shows estimated electromagnetic corrections applied to the spinor-quartet masses. The average S^\pm spinor mass obtained from the A_2 experiments is 329.3 MeV. The close agreement of all of these mass determinations of the spinor S^\pm is, in the author’s opinion, a strong argument for the reality of the A_2 interference effect.

An interesting determination of the mass S^\pm comes from the equations of special relativity as applied to rotating systems (Appendix B). Equation (B1) in Appendix B establishes the mass relationship $M_{S^\pm} = M_{S^\pm}(M_{3^\pm}, R_{\max}, R_{\min})$. Thus only three of these four parameters are independent. In

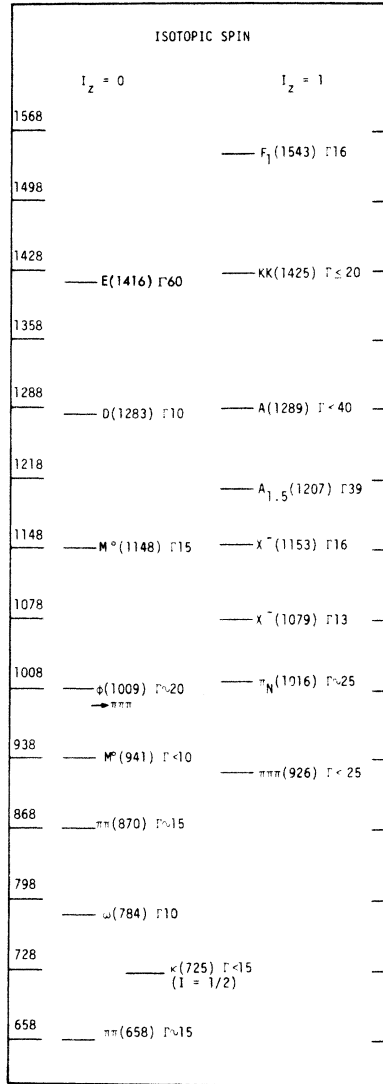
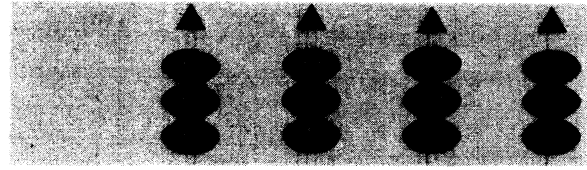


FIG. 19. A meson excitation tower based on the $\hat{S}\hat{S}$ (658) nonstrange spinor pair "ground state." Unlike the spinless meson resonances of Fig. 5, many of these resonances are known to be spin-1 resonances. Dominant excitations are $\omega = \hat{S}\hat{S}\pi$, $\phi = \hat{S}\hat{S}\pi$, $D = \hat{S}\hat{S}\hat{S}\hat{S}$, and $E = \hat{S}\hat{S}\hat{S}\hat{S}$. The ϕ meson is shown here in its $\pi\pi\pi$ decay mode. The isotopic-spin headings are discussed in Ref. 6. The obscure $I = \frac{1}{2}$ κ (725) kaon resonance fits naturally into this excitation tower (the excitation $\hat{S}\hat{S}1$ is strange, since the quantum $1 \equiv M$ is strange). A number of predictive successes have emerged from this meson excitation tower, which was first published in 1970. These predictive successes are summarized in paper I. The ϕ resonance shown here is discussed in Appendix C.

Table I we have selected R_{\min} as the dependent variable. With respect to Eq. (B1), it is important to note that all four of the parameters M_{S^\pm} , M_{3^\pm} , R_{\max} , and R_{\min} have several independent determinations for their values: M_{S^\pm} is determined



SPINOR	S	\bar{S}	\hat{S}	\tilde{S}
STRANGENESS	"+1"	0	0	"-1"
HADRONIC B.E.	$\sim 4\%$	~ 0	~ 0	$\sim 4\%$
ANGULAR MOM.	$\frac{1}{2}\hbar$	$\frac{1}{2}\hbar$	$\frac{1}{2}\hbar$	$\frac{1}{2}\hbar$

FIG. 20. Strange and nonstrange forms of the spinor S . Figures 17 and 20 show analogous characteristics for the spinless caber 3 and the spinor S . The fundamental spinor-pair production and decay transition $333 \leftrightarrow SS$ is discussed in Appendix C. This transition gives an explanation for the quantization of spin angular momentum, and it leads to a fundamental spin and isotopic-spin selection rule: $\hat{S}\hat{S}$ spinor pairs occur either as $J=1, I=0$ or as $J=0, I=1$ configurations. Spinors S occur in hadron resonances in a very distinctive manner, namely as $\hat{S}\hat{S}$ and $\tilde{S}\tilde{S}$ spinor triplets in baryon resonances and as $\hat{S}\hat{S}$ and $\tilde{S}\tilde{S}\hat{S}\hat{S}$ pairs and quartets in meson resonances. From their 4% hadronic binding energies, the spinors S and \bar{S} are "strange," but from the invariant nature of $\hat{S}\hat{S}$ triplets, this strangeness is an invariant (and therefore ignorable) in associated-production reactions. Thus we formally assign to the spinors S and \bar{S} a strangeness $S=0$. As is shown in Sec. IV, strange and nonstrange spinors have the same intrinsic masses, and as is shown in Appendix B, the spin angular momentum $J = \frac{1}{2}\hbar$ is a calculated quantity.

from Table XI, M_{3^\pm} is determined from the phenomenology of the spinless mass quanta (Tables I and X), R_{\max} is accurately determined by the spin angular momentum and probably also by the magnetic moment (Appendix B), and R_{\min} is determined from both the K^0 - K^\pm mass-splitting calculation of Fig. 9 and the nucleon volume as obtained from optical-model calculations (Appendix B). The fact that one set of values for these four parameters satisfies Eq. (B1) and also all of these other phenomenological requirements is one of the most important tests of the present geometric light-quark model.

As in the case of Table X, our purpose in Table XI has been to demonstrate the universality of the spinor S rather than to obtain a "best value" for the mass of the spinor S^\pm . In particular, we can see from the results of Table XI that the spinors S, \bar{S} and \hat{S}, \tilde{S} have the same intrinsic masses once the binding-energy effects have been disentangled.

D. The mass quantum $S^{\pm\pm} = 336.9$ MeV

Special relativity (Appendix B) shows that a spherical mass quantum which is initially at rest

TABLE IX. Summary of intermediate-width baryon and meson S -state resonances that contain nonstrange excitation quanta. These states are formed in accordance with rules (5) and (6) of Table III, and they are plotted in Figs. 16 and 19.

Excitation rule. Intermediate-width S -state baryon resonances are formed by adding nonstrange quanta $\dot{3}$ and $\dot{4}$ to the basic "ground states" $N(939)$, $\Lambda(1116)$, $\Sigma(1193)$, and $\Xi(1321)$; intermediate-width S -state meson resonances are formed by adding non-strange quanta π , 3 , and 4 to the basic "ground state" $S\bar{S}(658)$.

Observed resonances.

Baryon—19 resonances (shown in Fig. 16);
Meson—16 resonances (shown in Fig. 19).

Average calculated mass accuracy (comparison of experimental masses with the 70-MeV mass grids shown in Figs. 16 and 19).

Baryon—19 resonances, ± 7.5 MeV or $\pm 0.47\%$;
Meson—16 resonances, ± 6.5 MeV or $\pm 0.57\%$.

Over-all calculated S -state mass accuracy (the 54 resonances listed in Tables VI, VII, and IX): $\pm 0.38\%$.

Probabilities for random spacings (the probabilities that the resonance levels of Figs. 16 and 19 actually represent random spacings instead of 70-MeV interval spacings).

Baryon— $(7.5/17.5)^{19} \approx 1 \times 10^{-7}$;
Meson— $(6.5/17.5)^{16} \approx 1 \times 10^{-7}$.

becomes half again as massive when it is set into relativistic rotation (with its equator near the velocity of light). If this same mass ratio holds for Coulomb self-energies, then we would expect the 4.6-MeV charge splitting of spinless quanta to become a 6.9-MeV charge splitting for spinors S (at least as an order-of-magnitude estimate). However, in the doubly charged spinor S^{++} the induced magnetic field from the two rotating currents will lower this value somewhat. Empirically, an S^{++} - S^+ charge splitting of 6.3 MeV reproduces both the n - p mass difference and the Ξ^- - Ξ^0 mass difference (see Table VII).

E. The binding energy $M\bar{M} = -5.0$ MeV

This binding energy was selected to be used in conjunction with the mass values $M^0 = 70.0$ MeV and $M^\pm = 74.6$ MeV in reproducing the pion masses of Fig. 6. Experimental evidence for this 5-MeV $M\bar{M}$ binding energy is provided by the $M(953)$, $\eta'(958)$, $\delta^0(963)$ fine structure shown in Figs. 5 and 8 and in Table V.

F. The binding energy $M\bar{M}_s = -5.0$ MeV

We would expect the $M\bar{M}_s$ binding energy to be intermediate between the $M\bar{M} = -5.0$ MeV and $M_s\bar{M}_s = -9.1$ MeV values. Empirically, $M\bar{M}_s = \bar{M}M_s = -5.0$ MeV gives accurate mass values (Table VII).

G. The binding energy $M_s\bar{M}_s = -9.1$ MeV

The $\bar{p}n$ binding energy is -83.3 ± 0.14 MeV. Of this amount, -1.3 MeV is attributable to magnetic and Coulomb effects. Thus -82.0 MeV represents hadronic binding energy. If we assume that the

$\bar{p}n$ bound state includes three extranucleon $S\bar{S}$ pairs (Fig. 11), then each $S\bar{S}$ pair has a hadronic binding energy (HBE) of -27.3 MeV, and each $M_s\bar{M}_s$ sub-pair has HBE = -9.1 MeV.

H. The magnetic binding energy $S^+S^+ = \pm 1.7$ MeV

This spinor-pair binding energy is deduced from the reaction $\Sigma^0 \rightarrow \Lambda + \gamma$, as is described in Fig. 22. If we estimate magnetic binding energies on the basis of the observed magnetic moments, they are an order of magnitude smaller than the value of ± 1.7 MeV deduced in Fig. 22. Thus this large phenomenological value must arise from the singular nature of adjacent current loops. Hence we have the result that only *adjacent* (singly charged) spinors will bind with a magnetic binding energy of ± 1.7 MeV; magnetic binding energies for nonadjacent spinors can be disregarded at the level of accuracy in the present calculations.

I. The magnetic moment $\mu = \pm 0.93$ nuclear magneton (μ_N)

Magnetic-moment calculations in the present paper lead to a difficulty, but it is an intriguing difficulty. In the conventional quark model,¹⁴ the quark is assumed to have an "intrinsic" magnetic moment (per unit charge) of 2.79 nuclear magnetons. In the present model, if the spinor S contains a charge that is free to move, it will be forced to the equator by the action of the magnetic field. At the equator, which is the radius $R_{\max} = \frac{1}{3}\sqrt{3}F$, this rotating charge produces a calculated magnetic moment $\mu = \pi R_{\max}^2 i = 2.79$ nuclear magnetons (Appendix B)—the same value that is assumed for (integrally charged) quarks. However,

this value for μ gives magnetic moments for the p , n , Λ , Σ^+ , and Ξ^- , as calculated here, that are all too large by a factor of three. Since an equatorial charge distribution represents the largest possible magnetic moment, it is easy to modify this charge distribution so as to obtain smaller magnetic moments. But with no phenomenologically significant basis for making the required alteration in the charge distribution, this difficulty has been handled by introducing an intrinsic spinor magnetic moment $\mu = 2.79/3 = 0.93\mu_N$ as parameter (9) of the model, which suppresses the unwanted factor of three. It is not clear whether the difficulty with the magnetic-moment calculation arises from the values for the individual spinor magnetic moments or from the manner in which quark projection operators should be handled. This problem is left here as an unresolved difficulty with the present model. In the Coulomb calculations described below, spinning charged quanta are assumed to have equatorial current loops, for the reasons suggested here.

J. The radius $R_{\max} \approx \frac{1}{3}\sqrt{3} F$

The radius R_{\max} of the quantum M is determined from the two requirements of reproducing the spin angular momentum $J = \frac{1}{2}\hbar$ and the magnetic moment $\mu = 2.79\mu_N$ [see the comments in Sec. IV I above] of the spinor S . These two *independent* requirements both lead (if the factor-of-three difficulty with the magnetic moment is suppressed) to essentially the same value for R_{\max} , $R_{\max} \approx \frac{1}{3}\sqrt{3} F$, as is calculated in detail in Appendix B.

The *dependent radius* $R_{\min} \approx \frac{1}{3} F$. The value of $R_{\min} \approx \frac{1}{3} F$ of the quantum M is obtained (see Appendix B) by inserting the values $M_{S_{\pm}} = 330.6 \text{ MeV}$, $M_{S_{\pm}} = 214.6 \text{ MeV}$, and $R_{\max} = \frac{1}{3}\sqrt{3} F$ into Eq. (B1) and carrying out a numerical (computer) integration of this equation. The value for R_{\min} can also be determined both from the K^0-K^+ mass difference (Fig. 9), and from optical-model determinations of the volume of the nucleon (Appendix B).

Coulomb self-energies. In spinless mass quanta, the self-energy of a unit electric charge is taken to be $+4.6 \text{ MeV}$, the $\pi^{\pm}-\pi^0$ mass difference; in spinning mass quanta, this value is roughly half again as large. The number of electric charges contained in a spinor S can in many cases be deduced by the total charge, spin, and magnetic moment of the resonance in which it is contained (as, for example, in the case of the nucleons of Fig. 10). The assignment of internal charges to spinless quanta is somewhat more arbitrary, but the simple caber charge rule stated in the paragraph on Coulomb self-energies in Table I gives

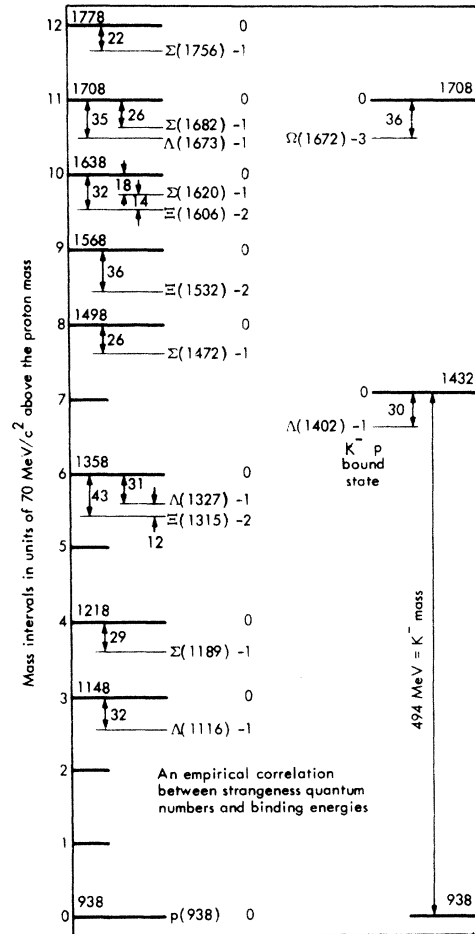


FIG. 21. An experimental relationship between strangeness quantum numbers and binding energies. The narrow-width and S-state hyperon resonances are shown plotted against a 70-MeV mass grid based on the fundamental nonstrange $p(938)$ proton ground state. As can be seen in Fig. 21, the strangeness -1 levels are shifted downward by $\sim 30 \text{ MeV}$ and the strangeness -2 and strangeness -3 levels are shifted downward by $\sim 40 \text{ MeV}$ with respect to the 70-MeV mass grid. These results are in contrast to Fig. 16, in which excitations that are plotted against 70-MeV mass grids based on ground states of the same strangeness as the excited levels show no downward shifts. Figures 16 and 21 illustrate the binding-energy rule of Table II in the text: Non-strange excitations (Fig. 16) have $\text{HBE} \approx 0\%$; strange excitations (Fig. 21) have $\text{HBE} \approx 4\%$. We also note in Fig. 21 that the $\Lambda(1402)$ resonance appears as a simple $K^{\bar{p}}$ bound state.

accurately calculated mass values.

Coulomb binding energies. Coulomb binding energies are calculated classically, using the caber dimensions and configurations described in Figs. 1–15. For definiteness in assigning charge dis-

TABLE X. Experimental and phenomenological determinations of the fundamental mass value $M^0 = 70.0$ MeV. Eight determinations are shown: two meson, one kaon, three hyperon, and two lepton; these all yield essentially the same mass value.

(1) $M^0(1033.6) - \delta^0(963.5) = M^0$	$\rightarrow M^0 = 70.1$ MeV	Appendix A
(2) $\Lambda^0(1402.4) - \Sigma^0(1192.5) = 3M^0$	$\rightarrow M^0 = 70.0$ MeV	See Fig. 15
(3) $\Omega^-(1672.2) - \Xi^-(1321.3) = 5M^0$	$\rightarrow M^0 = 70.2$ MeV	See Fig. 15
(4) $\Lambda^0(1673) - \Lambda^0(1115.6) = 8M^0$	$\rightarrow M^0 = 69.7$ MeV	Fig. 16
(5) $D^0(1286) - \dot{S}\dot{S}(658) = 9M^0$	$\rightarrow M^0 = 69.8$ MeV	Fig. 19
(6) $K^+(493.7) = 6M^0 + M^+$; $M^+ = M^0 + 4.6$ MeV	$\rightarrow M^0 = 69.9$ MeV	Fig. 9
(7) muon: $M_\mu(105.66) = \frac{3}{2}M^0$	$\rightarrow M^0 = 70.4$ MeV	Appendix E
(8) electron: $M_e(0.5110)/\alpha = M^0$	$\rightarrow M^0 = 70.0$ MeV	$\alpha = e^2/\hbar c$

TABLE XI. Determinations of the mass of the spinor S^+ . Mass values are obtained from (1) single spinors (electromagnetic properties of quarks), (2) $\dot{S}\dot{S}$ spinor pairs [the spin-1 $\pi\pi(658)$ dip], (3) $\dot{S}\dot{S}\dot{S}$ spinor triplets (the nucleon and the $\bar{p}n$ bound state), (4) $\dot{S}\dot{S}\dot{S}\dot{S}$ spinor quartets (the spin-2 A_2 dip). All of these determinations give essentially the same mass value for the spinors S^+ and \dot{S}^+ (as discussed in the text). In addition, special relativity (5) gives the spinor mass as a calculated quantity.

(1) *Single spinor S (quark)*. A number of quark-model arguments which are summarized in Table VIII of paper I indicate that the average mass of a nucleon quark is just about 330 MeV.

(2) *Spinor pair $\dot{S}\dot{S}$* .

$$\pi\pi(658) \text{ dip}^a + 3 \text{ e.m. corr.}^b = 661 \text{ MeV}/2 \rightarrow \dot{S}^+ = 330.5 \text{ MeV.}$$

(3) *Spinor triplet $\dot{S}\dot{S}\dot{S}$* .

$$(a) \bar{p}n \text{ binding energy} = -83.3 \text{ MeV} + 1.3 \text{ e.m. corr.}^b \rightarrow \text{HBE} = -82.0 \text{ MeV,}$$

$$(b) \text{HBE} = -82.0 \text{ MeV}/3 \rightarrow \text{HBE} = -27.3 \text{ MeV per } \dot{S}\dot{S} \text{ pair (Fig. 3),}$$

$$(c) S^+S^+S^+ \equiv p(938.3) + 2 \times 27.3 - 1.2 \text{ e.m. corr.}^b \rightarrow 991.7 \text{ MeV (unbound proton),}$$

$$(d) S^+ + S^+ + S^+ = 991.7 \text{ MeV} \rightarrow 991.7/3 = 330.6 \text{ MeV per spinor } S^+.$$

(4) *Spinor quartet $\dot{S}\dot{S}\dot{S}\dot{S}$ (location of the " A_2 effect")*.

(a) Location of the A_2 dip:

Experiment	Location	Electromagnetic corr.	Corrected location
Kienzle ^c	1310 ± 2 MeV	$(\dot{S}\dot{S}\dot{S}\dot{S})^- \rightarrow +7$ MeV	1317 ± 2 MeV
BCS ^{d,a}	1307 MeV	$(\dot{S}\dot{S}\dot{S}\dot{S})^0 \rightarrow +10$ MeV	1317 MeV
BDNPT ^e	~ 1310 MeV	$(\dot{S}\dot{S}\dot{S}\dot{S})^+ \rightarrow +7$ MeV	~ 1317 MeV
Barnham ^f	~ 1310 MeV	$(\dot{S}\dot{S}\dot{S}\dot{S})^+ \rightarrow +7$ MeV	~ 1317 MeV
Bloodworth ^g	~ 1305 MeV	$(\dot{S}\dot{S}\dot{S}\dot{S})^+ \rightarrow +7$ MeV	~ 1312 MeV

(b) Location of an A_2 peak:

$$\text{Crenneil}^h \quad 1311 \pm 2 \text{ MeV} \quad (\dot{S}\dot{S}\dot{S}\dot{S})^0 \rightarrow +10 \text{ MeV} \quad 1321 \pm 2 \text{ MeV}$$

(c) Average location of the " A_2 effect" ≈ 1317 MeV:

$$1317 \text{ MeV}/4 \rightarrow S^+ = 329.3 \text{ MeV.}$$

(5) *Special relativity*. Equation (B1) in Appendix B gives the mass S^+ as a function of the rest mass 3^+ and the eccentricity $\epsilon = (R_{\max} - R_{\min})/R_{\min}$. Choosing the values $3^+ = 214.6$ MeV, $R_{\max} = \frac{1}{3}\sqrt{3} F$, and $R_{\min} = \frac{1}{3} F$ and carrying out a numerical (computer) integration of Eq. (B1) gives a mass $S^+ \approx 330$ MeV.

Summary of S^+ mass determinations.

- (1) S (quark) $\rightarrow S^+ \approx 330$ MeV;
- (2) $\dot{S}\dot{S}$ $\rightarrow S^+ = 330.5$ MeV;
- (3) $\dot{S}\dot{S}\dot{S}$ $\rightarrow S^+ = 330.6$ MeV [used as parameter (3) in Table I];
- (4) $\dot{S}\dot{S}\dot{S}\dot{S}$ $\rightarrow S^+ = 329.3$ MeV;
- (5) Special relativity $\rightarrow S^+ \approx 330$ MeV.

^a See Fig. 8 in Ref. 17.

^b See text.

^c Reference 18.

^d Reference 19.

^e Reference 20.

^f Reference 21.

^g Reference 22.

^h Reference 23.

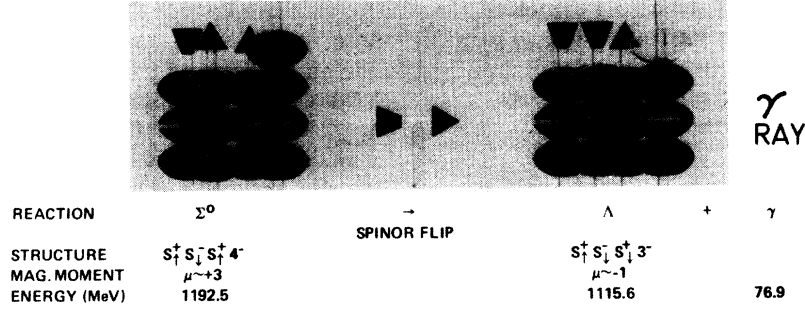


FIG. 22. An empirical determination of the SS spinor-pair magnetic interaction energy from the decay $\Sigma^0 \rightarrow \Lambda + \gamma$. The Σ^0 and Λ hyperons shown in the figure have identical Coulomb energies. Hence the electromagnetic energy difference of 6.9 MeV indicated in the figure is due to magnetic effects. The Σ^0 has +3 magnetic pairs ($++$), and the Λ has -1 magnetic pair ($+-$), where +1 pair denotes a repulsive interaction that contributes positively to the potential energy. Thus the 6.9 MeV of magnetic energy is attributed to the difference $(+3) - (-1) = +4$ magnetic pairs, which gives a magnetic pairing energy of 1.7 MeV per pair.

tributions within a quantum M , an equatorial charge distribution is assumed for spinning quanta and a centered point charge for spinless quanta. The difference between these two charge distributions is not large for Coulomb corrections as carried out in the present paper. For example, if we consider adjacent charged quanta M^\pm or M_s^\pm , the *point-point* Coulomb interaction is $e^2/2R_{\max} \approx 1.2$ MeV for $R_{\max} = \frac{1}{3}\sqrt{3}F$; the *point-loop* interaction is 1.3 MeV, and the *loop-loop* interaction is taken to be 1.4 MeV (the point-loop correction is doubled).

Spin angular momentum. As shown in Appendix B, the spin angular momentum $J = \frac{1}{2}\hbar$ of the spinor S is a directly calculated quantity. The equations of special relativity as applied to rotating systems are used to calculate a relativistic moment of inertia I , and hence an angular momentum $J = I\omega$, for the spinor S .

Parity. The parity rules of the present light-quark model are not the same as those of the conventional quark models.^{4,5} From the negative-parity configurations $1\bar{1} = \pi$, $4\bar{4} = \eta$, $7\bar{7} = \eta'$, $7 = K$, and $\bar{7} = \bar{K}$, we see that hadronically bound caber-anticaber pairs and single strange cabers have negative parities. If we assign positive parities to nonstrange $\bar{S}\bar{S}$ spinor pairs and to nonstrange excitation quanta 3 and 4, and negative parity to the excitation quantum π , then the parities of the resonances $\omega = \bar{S}\bar{S}\pi$, $\phi = 3\bar{S}\bar{S}\pi$, $D = 3\bar{S}\bar{S}\bar{S}\bar{S}$, $E = 4\bar{4}\bar{S}\bar{S}\bar{S}$, and $A_2 \text{ dip} = \bar{S}\bar{S}\bar{S}\bar{S}$ are all correctly reproduced. In the case of rotational resonances, the rotating bandheads appear with effectively positive parities (see paper I), which accounts for the predominance of broad-width $J^P = 1^-$ and $J^P = 2^+$ experimental resonances. In the case of the ϵ and S^* resonances,² the parity follows from the J quantum number and not from the L quantum number.

V. SUMMARY

At the beginning of this paper, it was stated that it is possible to devise a light-quark model for hadrons in which all quark-quark binding energies are less than 5%. It was further asserted that a formulation of this light-quark model can be defined which contains approximately ten numerical parameter values, which yields calculated mass values accurate to about one part in a thousand for all of the observed pseudoscalar meson resonances and metastable baryon resonances, and which reproduces the principal quantum numbers of these resonances. The aim of the present paper has been to demonstrate the following: (a) These claims are mathematically correct; (b) this light-quark model, although somewhat unconventional, is simple and straightforward in its phenomenological properties; (c) many of the numerical parameter values of the model can in fact be determined from the experimental data; (d) most of the parameters of the model have multiple constraints which exceed the available degrees of freedom, and the parameters are able to simultaneously satisfy these constraints; (e) the model seems capable of handling all of the different aspects of hadron spectroscopy.

In the present paper we have considered only the S -state meson and baryon resonances—the very-narrow-width S states of Sec. II, which are formed from strange cabers and anticabers, and the intermediate-width S states of Sec. III, which contain nonstrange cabers. As was described in paper I, many of the intermediate-width S -state resonances have associated rotational bands, and these rotational bands complete the mapping of the hadron resonance spectrum.

Although we have provided few references to the

experimental data, paper I contains a complete documentation of all of the data, including in particular discussions of resonances for which the author has different interpretations than those given in the Review of Particle Properties, RPP73.²⁴

The author would like to end this paper with the following friendly challenge to the reader: (1) Reproduce some of the mass calculations of Tables VI and VII to see that they really do work as advertised; (2) try changing any of the essential features of Tables I–III and see if the mass accuracy that is summarized in Table VIII can still be maintained. When these changes are attempted, it is soon discovered that at the accuracy level of one part in a thousand the experimental data are remarkably restrictive, especially when the constraints imposed by the requirements of reproducing spins, magnetic moments, charge splittings, and strangeness quantum numbers are also taken into consideration.

NOTE ADDED IN PROOF

Subsequent to the publication of paper I (Ref. 1), a new Review of Particle Properties, RPP74 (Ref. 25), has appeared. Thus it is of some interest to summarize new experimental information from RPP74 which bears on the systematic results discussed in paper I.

In the N and Δ resonances, a new comprehensive phase-shift analysis, Ayed 74, is included. Some preliminary results from this analysis were contained in paper I as Ref. 78. From Ayed 74 in RPP74, we have the following pertinent results: (1) The split Roper resonance is shown and discussed; (2) a narrow width is indicated for the $N(1520)S$ resonance, as expected from the systematics of paper I; (3) evidence for the $N(2133)G_{19}$ resonance, listed in Table XX of paper I with a C rating, is described as “quite good” in RPP74; (4) some confirmation is given for the $\Delta(2174)G_{39}$ resonance, first reported by Von Schlippe 72, which fills out the dominant Δ rotational band of Table XIX in paper I. Rey *et al.*²⁶ also give evidence for a negative-parity (G -wave?) resonance $\Delta(2196)$. Higher-energy S , P , and D levels continue to appear in the N and Δ amplitudes, showing that the systematics of Tables XVIII–XX in paper I extend to higher energies than are included there.

In the Λ and Σ resonances, Hart 73 report $\Lambda(1672)S_{01}$ $\Gamma 19 \pm 2$, which gives the narrow width expected for this S -state resonance, and they also report $\Lambda(1684)D_{03}$ $\Gamma 86 \pm 9$, which gives the broad width expected for this rotational level (compare these widths to the values shown in Table XVII of paper I). Cline 73 furnish additional evidence

for the narrow $\Sigma(1472)$ resonance observed by Pan 70. Jones 74 report $\Sigma(1760)S_{11}$ $\Gamma 92$, which has the mass expected from the results of paper I (Table XVI), but which has a broader width than we would expect for this S state.

In the Ξ resonances, Rossi 73 report $\Xi(1821)\Gamma 12$, which furnished much-needed confirmation for a narrow Ξ resonance at this energy (see Footnote c of Table VII in paper I). Rossi 73 also report $\Xi(1952)\Gamma 38$ and $\Xi(2019)\Gamma 33$, which are included in the present paper in Fig. 16, and which accurately match the 70-MeV level spacings marked in Fig. 16.

In Table XXX of paper I, rotational systematics were given for some observed energy levels in very light nuclei. Included in Table XXX was some rather uncertain evidence for a rotational level in He^3 at an energy of about 23 MeV. A recent phase-shift analysis by Arvieux,²⁷ indicates a broad He^3 P -wave phase shift resonance at the somewhat lower energy of 14 MeV. This value corresponds to $E_{\text{rot}} = 7$ MeV for He^3 in Table XXX, and it shifts the He^3 points shown in Figs. 11 and 12 of paper I so that they are actually in somewhat better agreement with the rotational systematics of the other resonances. With respect to the He^5 and Li^5 levels listed in Table XXX of paper I, recent studies (see below) indicate that the ground states for these resonances are rotational levels, so that the excited state energies shown in Table XXX cannot be identified directly as rotational energies; hence He^5 and Li^5 should be deleted from the systematics of Table XXX and Figs. 11 and 12 in paper I.

The present model can be readily extended to encompass atomic nuclei. If the strong (4%) hadronic force does not operate in collections of nucleons, then the nuclear force must be electromagnetic, and its attractive component is necessarily magnetic. From this result, from the nucleon quark geometries shown in Figs. 10 and 11, and from the observed pairing interactions in atomic nuclei, it seems clear that nucleons cluster side by side in atomic nuclei, in the form of two-dimensional “Ising” layers, with each layer having a thickness of 2 F (the height of the nucleons shown in Figs. 10 and 11). This leads to a “laminar cluster model” for nuclei, with a large nucleus containing a number of Ising layers, and with each Ising layer composed of α -particle “clusters” and other light-nucleus “clusters.” As one consequence of this formalism, the prolate U^{238} nucleus, which has an experimentally determined length of 18 F, contains nine Ising layers, and the assumption of low-energy fission at a central Ising interface (where Coulomb repulsion is the strongest) gives an immediate *quantitative ex-*

planation for the observed asymmetry in low-energy U^{238} fission, with the large and small fission fragments containing five and four Ising layers, respectively.

The author would like to take this opportunity to make the following corrections to paper I: Page 1275, bottom of first column: "isotropic spin $I=0$ " should read "isotropic spin $I=0$ "; page 1281: "AYED (Ref. 46)" should read "AYED (Ref. 78);" page 1289, Table XXII, (4): "[see Eqs. (27) and (28)]" should read "[see Eq. (35) and the accompanying discussion];" page 1309, Table XXXV, F: " $\overline{SS} = N$ " should read " $\overline{SS} = \overline{N}$ ";" page 1313, caption to Fig. 21: "The experimental lifetimes are from Ref. 1" should read "The experimental lifetimes are from Ref. 25;" page 1326, Ref. 127: "(see Fig. 19)" should read "(see Fig. 18)."

ACKNOWLEDGMENT

The author would like to thank R. J. Howerton for his continued interest in this work.

APPENDIX A: SOME PROPERTIES OF THE PSEUDOSCALAR MESONS

Properties of the pseudoscalar mesons were discussed in Sec. II, shown in Figs. 5-9, and calculated in Table VI. In the present section, we expand briefly on some of the special features of these resonances.

The appearance of the neutral-meson fine structure $M(953)$, $\eta'(958)$, $\delta^0(963)$ is very important because of its theoretical implications: This fine structure is perhaps the most direct evidence we have for the existence of an underlying light-quark substructure in these hadron resonances. Thus it is important to review the experimental evidence for this splitting of the pseudoscalar meson masses. In the δ^0 experiment,⁹ both the η' and δ^0 peaks were observed, and the δ^0 - η' mass difference was established as 5.4 ± 1.4 MeV. The η' - M mass difference is more difficult to determine, because the symmetric experiments which show the M cannot show the η' , and the asymmetric experiments which show the η' do not show the M (Table V). However, there are, nevertheless, two fairly accurate measurements of the M that give us this mass difference. In one M experiment,⁷ $p+d \rightarrow He^3 + M$, the π^0 , η , and ω peaks were available as energy calibration points. Thus the position of the M peak could be accurately pinpointed and was found to be $953.4_{-2.5}^{+1.1}$ MeV. The mass of the η' is known from a number of recent experiments²⁴ to be 958.1 ± 0.4 MeV. Thus the masses of these two resonances are clearly separated. In a second M experiment,⁸ both the $K^- + p \rightarrow K^- + p + M$ and K^-

$+ p \rightarrow \Lambda + \eta'$ channels were measured, thus permitting a common calibration for the experimental energies. The η' and M masses measured in this experiment were as follows.

	All final states	Final states containing a γ ray
η'	955.7 ± 2.0 MeV	956 ± 2 MeV
M	951 ± 4 MeV	953 ± 2 MeV

While these results do not establish the η' - M interval spacing as being precisely 5 MeV, they do indicate, when they are combined with the experiment of Maglich *et al.*⁷ and with the many η' experiments,²⁴ a definite mass displacement between the η' and M resonances.

In addition to the mass differences just discussed, the η' and M mesons can be differentiated both on the basis of their different production modes and on the basis of their different decay modes, as is summarized in Table V. It is instructive to write down equations for these reactions. In writing these equations, it is useful, especially with respect to strangeness properties, to represent the interaction quanta as combinations of the symmetric excitation $\pi \equiv M\overline{M}$ (Fig. 6) and the asymmetric excitation $3 \equiv 3$ or $\hat{3}$ or $\overline{3}$ (Fig. 17); the kaons, for example, then appear as $K = 3\pi\pi$ and $\overline{K} = \overline{3}\pi\pi$, and the η as $\eta = 4\overline{4} = 3\overline{3}\pi$ (this caber substructure is suggested in Figs. 2 and 3). As additional notation, the basic spinor core configurations are $\hat{p} = S_1^+ S_2^- S_3^+$, $\hat{n} = S_1^+ S_2^- S_3^+$, and $\hat{\Lambda} = S_1^+ S_2^- S_3^+$, and the square [] and curly { } brackets represent destruction and creation operators, respectively. With these conventions, Eqs. (b) and (c) in Table V become

$$(b) \quad K^- + p \rightarrow K^- \{ 3\overline{3}\pi 3\overline{3} \} \hat{p} \\ \rightarrow K^- + 7\overline{7} + p \\ \rightarrow K^- + M + p, \quad 3\overline{3}\pi 3\overline{3} = 7\overline{7} = M$$

and

$$(c) \quad K^- + p \rightarrow \overline{3}\pi\pi \{ 3\pi \cdot \overline{3}\pi \} \hat{p} \\ \rightarrow \hat{\Lambda} \overline{3} + \pi\pi 3\pi \overline{3}\pi \\ \rightarrow \Lambda + \eta', \quad \pi\pi 3\pi \overline{3}\pi = 7\overline{7} = \eta'$$

The symmetry of the reaction (b) requires perfectly matched internal particle-antiparticle symmetry for the newly created M meson, whereas the scrambled excitation that forms the η' meson evidently contains one unmatched internal pair (these results are illustrated schematically in Fig. 8).

The symmetry characteristics of the M and η' mesons also carry over to the decay modes. The M has the direct one-step annihilation process

(from Table V)

$$(e) M = 7\bar{7} \rightarrow [3\pi][\bar{3}\pi]\pi\pi + \gamma,$$

whereas the η' has the sequential two-step decay (also from Table V)

$$(f) \eta' = 7\bar{7} \rightarrow [3\pi]333 \rightarrow \dot{S}\dot{S} + \gamma = \rho + \gamma,$$

$$\dot{S}\dot{S} \rightarrow 333 \rightarrow [3\pi] + \pi\pi$$

where $\dot{S}\dot{S}$ in a rotational mode is the ρ meson²⁸ (see paper I), and where the transition $333 \rightarrow \dot{S}\dot{S}$ is discussed in Appendix C. In analogy to the decay modes (e) and (f), we note that the ω meson has the decay mode

$$\omega = \dot{S}\dot{S}\pi \rightarrow 333\pi \rightarrow [3\pi]33 \rightarrow \pi\pi\pi.$$

The $\delta^-(962)$ meson has been a difficult level to pin down experimentally. From its production mode, $\pi^- + p \rightarrow \delta^- + p$, it is an η' -type resonance, and we expect to see it appearing 4.5 MeV above the η' (Fig. 8 and Table VI), or possibly above the δ^0 peak. Although subsequent missing-mass experiments have not repeated the original CERN²⁴ observation of this peak, Defoix *et al.*²⁹ have observed it in the decay modes $D^0 \rightarrow \delta^+ \pi^-$ and $D^0 \rightarrow \delta^- \pi^+$, with a mass that is 320 MeV below the mass of the D^0 meson (see Fig. 19), and with a width $\Gamma = 30$ MeV that is consistent with their resolution of 30 MeV and hence, when unfolded, is much narrower than 30 MeV. Also, Atherton *et al.*³⁰ have observed this narrow peak and have identified its spin-parity as $J^P = 0^-$.

One other resonance that is of interest here is the $M^0(1033.6)$ peak shown in Table X. This peak

and the $\delta^0(963.5)$ peak were measured by the same group^{9,31} in the same type of experiment, $\pi^- + p \rightarrow X^0 + n$, with a time-of-flight neutron energy determination, and with the η' peak available as a reference mass in each case (the M^0 and δ^0 mass values quoted here are adjusted to match the mass used here for the η'). The difference in mass between the M^0 and δ^0 peaks, as noted in Table X, is 70.1 MeV, which suggests the structure $M^0(1033.6) = 7^+ 8^-$.

As one final topic in connection with the pseudo-scalar meson resonances, it is interesting to observe that the particle configurations shown in Figs. 6 and 9 also have phenomenological significance with respect to the lifetimes of these particles.³² The metastable mesons and hyperons ($\tau \sim 10^{-10}$ to 10^{-8} sec) show accurate 2:1 and 4:2:1 ratios in the lifetimes, and also an over-all scaling as powers of $\alpha = e^2/\hbar c$ (see paper I). Figure 23 shows the manner in which these factor-of-two lifetime ratios can be accounted for in terms of the caber structures of Figs. 6 and 9, which were deduced originally on the basis of the masses, strangeness characteristics, and decay modes of these resonances.

APPENDIX B: THE GEOMETRY OF THE SPINOR S

In this appendix we summarize the phenomenological considerations which serve to fix the geometry of the spinor S. In Fig. 2 the light-quark cabers, including the spinor S, are all shown as linear arrays of quanta M or \bar{M} . The two reasons

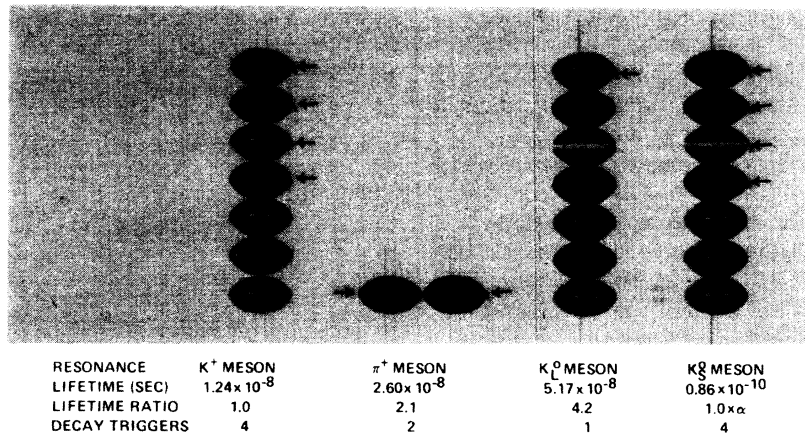


FIG. 23. Lifetime systematics of the K^+ , π^+ , K_L^0 , and K_S^0 mesons. As shown in this figure, the K^+ , π^+ , K_L^0 lifetimes form an accurate 1:2:4 lifetime triplet, and the K_S^0 can be grouped into a similar triplet shifted by one power of $\alpha = e^2/\hbar c$. Statistically, these accurate 1:2:4 lifetime ratios can be explained by assuming that 4:2:1 subquanta M are available to independently annihilate and trigger the decays (the author is aware of no other explanation for these lifetime ratios). Possible sets of decay triggers are indicated by the arrows. The anomalously long lifetimes of the resonances are related to the fact that the decays are triggered by the annihilation of single quanta M or \bar{M} , since resonances that contain matching internal $M\bar{M}$ pairs have much shorter lifetimes.

for assigning this configuration to the spinor S are that it systematizes spinor binding energies in an apparently unique manner (see Figs. 3 and 4), and it leads to a formalism for Coulomb corrections which also seems to be unique (see Table IV).

The spinor S and the spinless quantum 3 are related mathematically by the equations of special relativity as applied to rotating systems. For an individual mass quantum M , or for three quanta M in an aligned array (the caber 3), the relativistic mass increase m/m_0 and the relativistic moment of inertia I about the spin axis are given by the following equations, which were derived and discussed in Appendix B of paper I:

$$m = 3m_0 \int_0^{\pi/2} d\theta \frac{(1 + \epsilon \sin\theta)^2 (1 + 2\epsilon \sin\theta) \sin\theta \cos^2\theta}{[1 - \sin^2\theta(1 + \epsilon \sin\theta)^2/(1 + \epsilon)^2]^{1/2}} \quad (\text{B1})$$

and

$$I = 3m_0 R_A^2 \int_0^{\pi/2} d\theta \frac{(1 + \epsilon \sin\theta)^4 (1 + 2\epsilon \sin\theta) \sin^3\theta \cos^2\theta}{[1 - \sin^2\theta(1 + \epsilon \sin\theta)^2/(1 + \epsilon)^2]^{1/2}}, \quad (\text{B2})$$

where m_0 is the rest mass of the spinning quanta, where the rotation is at or near the full relativistic limit

$$\omega = c/R_{\max}, \quad (\text{B3})$$

and where the radii of the spinning quanta are

$$R_A = R_{\min} = \text{axial radius},$$

$$R = R_A(1 + \epsilon \sin\theta), \quad (\text{B4})$$

$$R_E = R_{\max} = \text{equatorial radius} = R_A(1 + \epsilon),$$

with

$$\epsilon = (R_E - R_A)/R_A. \quad (\text{B5})$$

ϵ is a deformation parameter that characterizes the oblateness of the spinning spheroid, and θ is the angle of the radius vector with respect to the axis of symmetry (which is also the spin axis). For a spherical geometry ($\epsilon = 0$), Eqs. (B1) and (B2) become simply

$$m = \frac{3}{2}m_0 \quad (\text{B6})$$

and

$$I = \frac{1}{2}mR^2 = \frac{3}{4}m_0R^2. \quad (\text{B7})$$

From (B1), it can be seen that

$$m = m(m_0, \epsilon), \quad (\text{B8})$$

a result that was used to classify the parameter R_{\min} as a dependent variable in Table I. From the equation

$$J = I\omega = Ic/R_{\max}, \quad (\text{B9})$$

the angular momentum J of the spinor S can be obtained as a directly calculated quantity. Also, for a unit equatorial charge distribution, the calculated magnetic moment of the spinor S is

$$\begin{aligned} \mu &= \pi R_{\max}^2 i \\ &= \pi R_{\max}^2 (e/c) (\omega/2\pi) \\ &= \frac{1}{2} e R_{\max}. \end{aligned} \quad (\text{B10})$$

The value chosen for R_{\max} is

$$R_{\max} \simeq \hbar/mc \simeq \frac{1}{3}\sqrt{3} F, \quad (\text{B11})$$

where $m = M_{S^{\pm}} = 330.6$ MeV, so that R_{\max} reflects the Compton wavelength of the spinor S . If we specialize these results to a spherical geometry, Eqs. (B3), (B7), (B9), and (B11) give

$$J = I\omega = \frac{1}{2}mRc = \frac{1}{2}\hbar \quad (\text{B12})$$

as the calculated spin angular momentum. In the more general case of an oblate spheroidal geometry, we must use Eq. (B9) together with a numerical integration of Eq. (B2). Inserting Eq. (B11) into Eq. (B10) gives

$$\mu = e\hbar/2mc \quad (\text{B13})$$

as a calculated magnetic moment.

The functions $V(\epsilon)$, $\mu(\epsilon)$, $I(\epsilon)$, and $m(m_0, \epsilon)$ that were used to fix the geometry of the spinor S are shown in Fig. 24, plotted as functions of ϵ . The volume $V(\epsilon)$ relates to the volume of a nucleon, which is obtained from the optical-model radius for heavy nuclei:

$$R_{\text{nucleus}} = 1.25 A^{1/3} F,$$

$$V_{\text{nucleon}} = V_{\text{nucleus}}/A$$

$$= \left(\frac{4}{3}\pi\right) (1.25)^3 \quad (\text{B14})$$

$$= 8.2 F^3.$$

$\mu(\epsilon)$, the calculated magnetic moment, should be matched to the intrinsic quark magnetic moment $\mu = 2.79 \mu_N$.¹⁴ $I(\epsilon)$, the moment of inertia, is used in the calculation of the spin angular momentum; in adjusting the parameters of the spinor S , the values for the spinning mass and for R_{\max} and R_{\min} were constrained so as to maintain $J = \frac{1}{2}\hbar$ exactly for all values of ϵ . The spinning mass $m(m_0, \epsilon)$ should match the mass of a spinor as given in Table XI. For the case where $\epsilon = 0$ (a spherical geometry), the volume V is too large, the magnetic moment μ is also too large, and the spinning mass is too small. As the value for ϵ is increased in the positive direction, the volume V decreases, the magnetic moment μ also decreases, and the spinning mass increases. Hence

the deformation of the quantum M away from a spherical geometry and into an oblate spheroidal geometry changes all of these quantities in the right direction. The values of ϵ for which each of the quantities V , μ , and m reaches its proper value are somewhat different from one another; these values are summarized in Table XII. However, the essential point here is that the use of an oblate spheroidal geometry for the quantum M is phenomenologically justified. Guided by the values for ϵ shown in Table XII, we have chosen the value at the bottom of the table, a value which gives $R_{\max}/R_{\min} = \sqrt{3}$. The functional dependence of the quantities V , μ , and m on ϵ is slowly varying (note the restricted ranges of the ordinates in Fig. 24), and the present simplified discussion should not be expected to yield precisely the same value of ϵ for each of these quantities.

APPENDIX C: THE FUNDAMENTAL TRANSITION 333 \leftrightarrow $\dot{S}\dot{S}$

Equation (B6) in Appendix B suggests that the transition 333 \rightarrow $\dot{S}\dot{S}$ is essentially isoergic. This transition actually seems to occur, in both directions, in hadron interactions, and it is in fact a cornerstone of the present light-quark phenomenology. The experimental indications for this transition were discussed in paper I, where an excitation symmetry scheme for generating meson resonances was presented. The main reason for discussing this transition here is to show how the caber geometries of the present model furnish a mechanical description of the transition process from spinless quanta to spinning quanta and back again.

Clear-cut evidence for the transition

TABLE XII. Summary of determinations of the deformation parameter ϵ for the mass quantum M_s as it appears in the spinor S [$\epsilon = (R_E - R_A)/R_A$, where R_E and R_A are the equatorial and axial radii of the oblate spheroids shown in Fig. 2]. Each value quoted for ϵ in the table is the value which gives the correct calculation for the quantity in question (see Fig. 24). Although the magnetic-moment calculation, volume calculation, and mass calculation all indicate somewhat different choices for ϵ , a phenomenologically significant improvement is obtained in each case by using an oblate spheroidal geometry instead of a spherical geometry. The value selected for ϵ in the present paper is the average of the three determinations shown here.

Quantity to be calculated	Calculated value		Required value for ϵ
	Sphere	Oblate spheroid	
Angular momentum (held fixed)	$(J = \frac{1}{2}\hbar)$	$(J = \frac{1}{2}\hbar)$	
Magnetic moment ^a	$\mu = 2.84\mu_N$	$\mu = 2.79\mu_N$	$\epsilon \sim 0.4$
Volume of the nucleon ^b	$V = 16 \text{ F}^3$	$V = 8 \text{ F}^3$	$\epsilon \sim 0.7$
Spinning relativistic mass ^c	$M = 321.9 \text{ MeV}$	$M = 330.6 \text{ MeV}$	$\epsilon \sim 1$
Consensus value for ϵ : $\epsilon \approx \sqrt{3} - 1$			

^a Based on a singly charged spinor S with an equatorial charge distribution.

^b The experimental volume is from optical-model calculations.

^c Based on Eq. (B1) with a rest mass of 214.6 MeV.

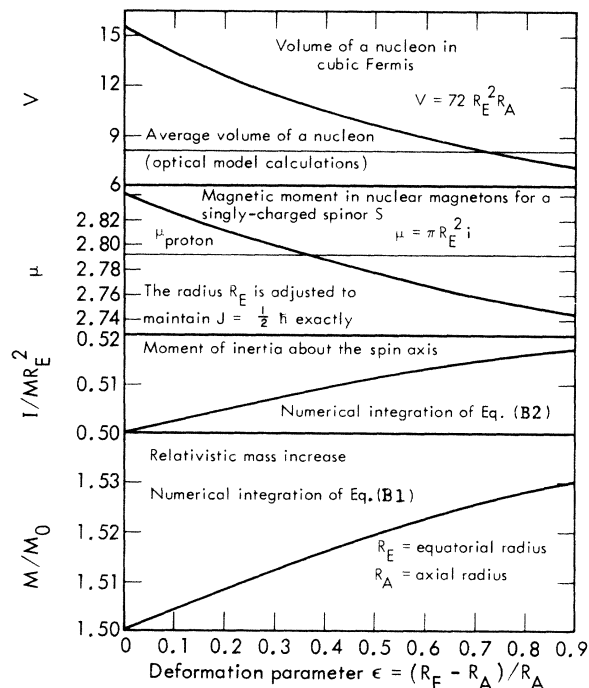


FIG. 24. Calculated quantities for relativistically spinning spheroid as a function of the deformation parameter $\epsilon = (R_E - R_A)/R_A$, where R_E and R_A are the equatorial and axial radii, respectively, of the spheroid. The quantities M/M_0 and I/MR_E^2 are obtained by numerical integration of Eqs. (B1) and (B2) in the text. The calculated variation of the magnetic moment μ is obtained by shrinking R_E slightly as I/MR_E^2 increases with increasing ϵ in order to maintain $J = \frac{1}{2}\hbar$ exactly (an equatorial charge distribution is assumed). The volume calculation is based on the assumption that the volume occupied by a nucleon ($N = SSS$) is $V = 9 \times 2R_E \times 2R_E \times 2R_A = 72 R_E^2 R_A$; this volume should match the average nucleon volume $V \approx 8 \text{ F}^3$, which is obtained from optical-model calculations for heavy nuclei (see the text).

$$333 \rightarrow 3_s [3] 3_s \dot{\dot{S}} \quad (C1)$$

is furnished by the η' decay mode of Eq. (f) in Appendix A. The η' is composed entirely of spinless quanta (Fig. 8), whereas the ρ meson, as outlined in considerable detail in Ref. 25 and in paper I, is the $\dot{\dot{S}}\dot{\dot{S}}$ spinor pair in a ${}^2S^{+1}L_J = {}^1P_1$ rotational mode. Figure 25 illustrates the transition (C1), and it shows how the details of the transition can be used to deduce the (J, I) spin and isotopic-spin rule given at the bottom of the figure. In the transition $333 \rightarrow \dot{\dot{S}}\dot{\dot{S}}$, conservation of energy leads directly to the quantization of spin angular momentum: in order to absorb all of the annihilation energy, the spinors \dot{S} must spin at the full relativistic limit of Eq. (B3), with their equators at or near the velocity of light.

Clear-cut evidence for the inverse transition

$$\dot{\dot{S}}\dot{\dot{S}} \rightarrow 3\{3\}3 \quad (C2)$$

is provided by the decay $\phi \rightarrow KK$. The narrow-width ($\Gamma = 4$ MeV) spin-1 ϕ meson must contain an $\dot{\dot{S}}\dot{\dot{S}}$ spinor pair, whereas the final-state kaons do not contain spinors. Furthermore, since the Q value for the reaction is only about 30 MeV, no quanta M can be annihilated in the decay process. Thus the transition

$$\phi = 3\dot{\dot{S}}\dot{\dot{S}}\pi \rightarrow 3333\pi \rightarrow 77 = K\bar{K} \quad (C3)$$

is mandated. This transition is illustrated in Fig. 26.

There is an interesting point to bring out in connection with the $\phi \rightarrow KK$ decay mode shown in Fig. 26. From the systematics of the meson resonances shown in Fig. 19, we would expect the ϕ meson

to appear at a mass of about 1008 MeV and with a width $\Gamma \sim 15$ MeV. However, the ϕ meson is quoted in RPP73 (Ref. 24) with a mass and width $\phi(1019.6)\Gamma 4.2$. An examination of the ϕ -meson experiments²⁴ reveals that these ϕ parameters are obtained only from the $\phi \rightarrow KK$ decay mode. In $\phi \rightarrow KK$ decay, we have the unusual situation of a spin-1 resonance that decays with a very small Q value into two spinless final-state particles. In order to carry off the spin angular momentum of the ϕ , the two kaons must be noncollinearly emitted, with a separation distance r_{KK} given by the angular momentum equation

$$[1(1+2)]^{1/2}\hbar = \vec{r}_{KK} \times \vec{P}. \quad (C4)$$

From the Q value of about 30 MeV in the $\phi \rightarrow KK$ decay, each kaon has a kinetic energy of about 15 MeV, and hence a linear momentum \vec{p} of about 123 MeV/c. Inserting this value for \vec{p} into Eq. (C4) gives

$$r_{KK} \approx 2.3 F, \quad (C5)$$

a result that is independent of any assumptions about light-quark structure. Since the spinor \dot{S} has a diameter $D = 2R_{\max} \approx 1.2 F$, the separation distance $R_{KK} \approx 2.3 F$ indicates that the kaons are emitted from the periphery of the $\dot{\dot{S}}\dot{\dot{S}}$ pair. The result of folding this $\phi \rightarrow KK$ kinematic constraint in with the natural resonance parameters of the ϕ meson is to shift a natural $\phi(\sim 1008)\Gamma \sim 15$ resonance (as suggested by Fig. 19) upwards in energy by an amount $\Delta E \sim \frac{1}{2}\Gamma$ and to narrow the width of the resonance.

If the above hypothesis is correct, then the ϕ meson as observed in its $\phi \rightarrow \pi^+\pi^-\pi^0$ decay mode

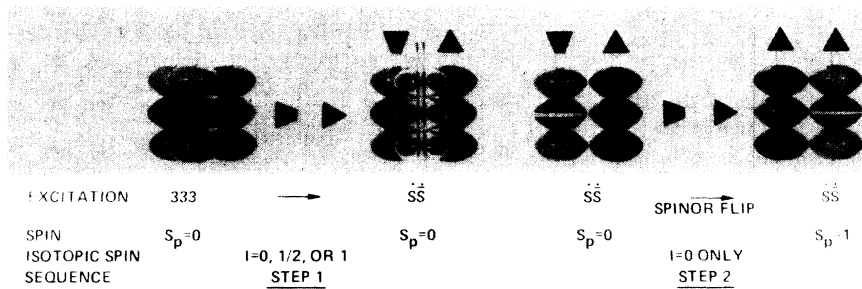


FIG. 25. The fundamental spinor production process $333 \rightarrow \dot{\dot{S}}\dot{\dot{S}}$. This reaction arises from the special relativistic result (Appendix B) that relativistically spinning spheres, with their equators near the velocity of light, are half again as massive as they were at rest. In this figure, we start with the basic excitation cluster 333. One 3 annihilates, and the tangential forces from the annihilation set the other two 3's spinning in opposite directions. In order to conserve energy, they must spin at the full relativistic limit, which leads automatically to the quantization of spin angular momentum, with each spinning 3 having spin angular momentum $J = \frac{1}{2}\hbar$. The spinning 3's constitute the nonstrange spinor pair $\dot{\dot{S}}\dot{\dot{S}}$ (658) (Fig. 19), with total angular momentum $J = S_p = 0$. This is step 1 of Fig. 25. If the $\dot{\dot{S}}\dot{\dot{S}}$ spinor pair is in the charge-symmetric isotopic-spin mode $I=0$ ($\dot{S}^+\dot{S}^-$), it can and does couple to external angular momenta via a photon exchange so as to have a spinor-flip transition and appear with $J = S_p = 1$. This is step 2 of Fig. 25. This two-step process leads to the important spin-isotopic-spin rule for $\dot{\dot{S}}\dot{\dot{S}}$ spinor pairs: $\dot{\dot{S}}\dot{\dot{S}}$ spinor pairs appear either as $J=1, I=0$ or as $J=0, I=1$ configurations. (Note that the $\dot{\dot{S}}\dot{\dot{S}}$ pairs described here are actually $\dot{\dot{S}}\dot{\dot{S}}$ pairs; this distinction between the spinors \dot{S} and $\bar{\dot{S}}$ is usually ignored in the text.)

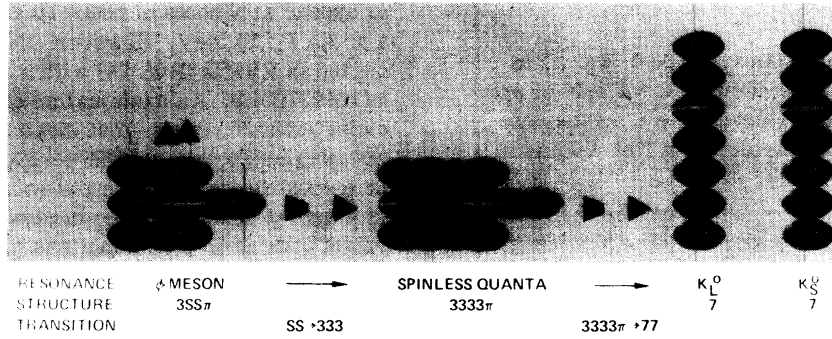


FIG. 26. The decay process $\phi \rightarrow KK$. The ϕ is the narrow-width spin-1 resonance $\phi = 3SS\pi$ (its spin of 1 and its narrow width show that it must contain a spinor pair SS). The kaon is the spinless caber 7 (see Figs. 7 and 9). Since the ϕ contains five quanta M ($\pi 3 = 5M$) plus a spinor pair SS , and the KK final state contains fourteen quanta M ($K = 7M$), the decay process $SS \rightarrow 333 = \text{nine quanta } M$ is unequivocally required. The isotopic spin $I = 0$ and spin angular momentum $J = 1$ of the ϕ meson constitute an example of the $I = 0, J = S_p = 1$ rule of Fig. 25 for SS spinor pairs.

should appear at a lower energy and with a broader width, since the large Q value in this latter reaction removes most of the angular momentum limitation on the final-state phase space. At the time this analysis was first published,³³ no direct measurements of the $\phi \rightarrow \pi^+\pi^-\pi^0$ decay mode existed from which one could determine the mass and width of the ϕ . However, several months later a Brookhaven experiment⁸ appeared which gave the $\phi \rightarrow \pi^+\pi^-\pi^0$ decay with a mass $\phi(1009 \pm 8)$ and with a width of roughly 20 MeV, in agreement with present expectations. These are the ϕ values that are shown in Fig. 19. The $\phi \rightarrow \pi^+\pi^-\pi^0$ decay seems identifiable with the elusive $H \rightarrow \pi^+\pi^-\pi^0$ meson, which has been seen weakly in a number of experiments,²⁴ and which has isotopic spin $I = 0$, a mass of about 1000 MeV, and is probably a spin-1 resonance.³⁴

APPENDIX D: ASSOCIATED-PRODUCTION EQUATIONS

In the present light-quark model for hadron resonances, all of the basis states are formed from the single mass quantum $M \sim 70$ MeV. By writing down equations for production and decay reactions in terms of the quantum M , it is possible to trace these reactions through in some detail. In this section we discuss a number of associated-production reactions—not from the viewpoint of providing a comprehensive treatment, but rather in the sense of sketching the manner in which the systematics of these reactions might be worked out.

1. Basis states and rules for associated production

Definition of strangeness. $S_1 = \text{first-class strangeness}$ —carried by spinless cabers—relevant for both binding energies (Table II) and strangeness quantum numbers.

$S_2 = \text{second-class strangeness}$ —carried by spinor triplets—relevant only for binding energies (see Table II and Figs. 2 and 20).

Excitation basis states.

$\pi \equiv M\bar{M}$	$S_1 = 0$	(Fig. 6)
$3 \equiv 3, \dot{3}, \bar{3}, \bar{3}$	$S_1 = +1, 0, 0, -1$	(Fig. 17)
$4 \equiv 4, \dot{4}, \bar{4}$	$S_1 = +1, 0, -1$	(Figs. 13 and 18)
$K \equiv 3\pi\pi, \bar{K} \equiv \bar{3}\pi\pi$	$S_1 = +1, -1$	(Figs. 7 and 27)
$333 \equiv 3\dot{3}\dot{3}$	$S_1 = +1 - 1 = 0$	Basic 3-triplet
$\bar{3}\bar{3}\bar{3} \equiv 3\bar{3}\bar{3}$	$S_1 = +1 - 1 = 0$	Basic 3-antitriplet

Spinor core configurations.

$$\begin{aligned}
 (\hat{p}) &= S_1^\dagger S_1^\dagger S_1^\dagger - \text{strangeness } S_2 = +1, \\
 (\hat{n}) &= S_1^\dagger S_1^\dagger S_1^\dagger - \text{strangeness } S_2 = +1, \\
 (\hat{\Lambda}) &= S_1^\dagger S_1^\dagger S_1^\dagger - \text{strangeness } S_2 = +1.
 \end{aligned}$$

Spinless mass operators. $\{ \}$ = creation operator—creation of quanta M . $[\]$ = annihilation operator—annihilation of quanta M . $\langle \rangle$ = transformation operator—transformation of quanta M or \bar{M} into their antistates: $\langle M \rangle \rightarrow \bar{M}$, $\langle \bar{M} \rangle \rightarrow M$.

Rules for the mechanism of associated production.

Rule (1) Strangeness $S_2 = +1$ (-1) spinor cores combine with strangeness $S_1 = -1$ ($+1$) spinless cabers to form Y^* resonances; strangeness $S_2 = +1$ (-1) spinor cores do not combine with strangeness $S_1 = +1$ (-1) spinless cabers to form Z^* resonances.

Rule (2) The conventional strangeness quantum number of a resonance is the sum of the strangeness quantum numbers S_1 carried by the spinless cabers in the resonance cluster.

Rule (3) The dominant excitations produced by

the creation operator $\{ \}$ in associated production are the same excitations which are dominant in the meson production reactions shown in paper I. These excitations, which are the straight conversion of kinetic energy into hadronic matter, are necessarily nonstrange.

Rule (4) The transformation operator $\langle \rangle$ occurs in conjunction with the annihilation operator $[\]$; the annihilation process can be associated with a geometrical rearrangement of the resonance structure. The transformation operator $\langle \rangle$ also seems to be responsible for the K_S^0 regeneration process ($K_L^0 = 3\bar{3}M - 3\bar{3}\langle M \rangle = 3\bar{3}\bar{M} = 3\bar{4} = K_S^0$), and it suggests that the physical K_L^0 secondary collision which causes the regeneration process leads to the re-orientation of the odd quantum M in the linear K_L^0 structure (see Fig. 9). These results both suggest that the distinction between the particle state M^0 and the antiparticle state \bar{M}^0 is the spatial orientation with respect to the resonance structure.

Rule (5) The asymmetric collision process $\pi + N$, in which a strangeness $S_2 = +1$ spinor core is involved, leads to the production of the excitation sequence $\{ \bar{3}\bar{3}\bar{3} \}$, $\{ \bar{3}\bar{3}\bar{3} \cdot 3\bar{3} \}$, $\{ \bar{3}\bar{3}\bar{3} \cdot 3\bar{3} \cdot 3\bar{3}\bar{3} \}$, etc., but not to the production of excitations such as $\{ 3\bar{3}\bar{3} \}$, $\{ \bar{3}\bar{3}\bar{3} \cdot 3\bar{3}\bar{3} \}$, etc.

2. Λ hyperon production

An associated production reaction for the Λ is

$$\pi + p \rightarrow \pi \{ \bar{3}\bar{3}\pi \} (\hat{p}) \rightarrow (\hat{\Lambda}) \bar{3} + 3\pi\pi = \Lambda + K. \quad (D1)$$

This reaction is shown pictorially in Fig. 27. The excitation $3\bar{3}\pi = 4\bar{4}$ shown in (D1) is the η meson. The spinor-flip transition $(\hat{p}) \rightarrow (\hat{\Lambda})$ is characteristically associated with an $I=0$ excitation channel, which may account for the isotopic spin $I=0$ of the Λ . From rule (1) the $(\hat{\Lambda})$ spinor core will combine with a $\bar{3}$ to form a Y^* resonance (the Λ), but it will not combine with a 3 to form a Z^* resonance. Typical decay processes for the final states of (1) are

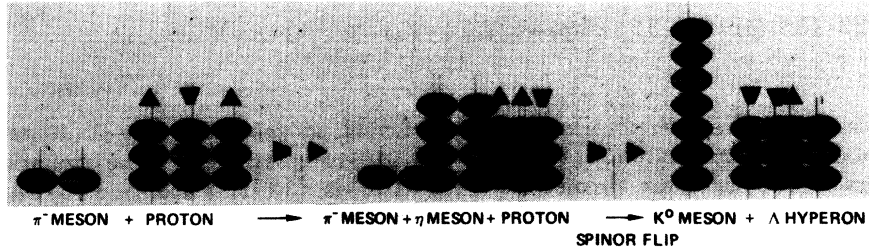


FIG. 27. A graphical display of the production process $\pi^- + p \rightarrow K^0 + \Lambda$. When the π^- strikes the proton, kinetic energy is transformed into hadronic matter in the form of an η meson. The η breaks apart asymmetrically, with one part combining with the π^- and the other part combining with the proton, so as to form a pair of resonances with strangeness $+1$ and -1 , respectively (which is the mechanism of associated production). This production process can be written as the sequence $\pi + p \equiv \pi + S\bar{S}S \rightarrow \pi \{ \bar{3}\bar{3}\pi \} S\bar{S}S \rightarrow S\bar{S}\bar{3} + 3\pi\pi \equiv \Lambda + K$, where $\{ \}$ is a creation operator.

$$\begin{aligned} \Lambda &= (\hat{\Lambda}) \bar{3} = (\hat{\Lambda}) \bar{M} \bar{M} \bar{M} \rightarrow (\hat{p}) [\bar{M}] \langle \bar{M} \rangle \bar{M} = (\hat{p}) + M \bar{M} = p + \pi \\ &\quad - (\hat{n}) [\bar{M}] \langle \bar{M} \rangle \bar{M} = (\hat{n}) + M \bar{M} = n + \pi, \\ K &= 3\pi\pi = M M M \pi \pi \rightarrow [M] \langle M \rangle M \pi \pi = \bar{M} M + \pi + \pi = \pi + \pi + \pi \\ &\quad \rightarrow [3] \pi\pi = \pi + \pi. \end{aligned}$$

3. Σ -hyperon production

An associated production reaction for the Σ is

$$\pi + p \rightarrow \pi \{ \bar{3}\bar{3}\bar{3} \} (\hat{p}) = \pi 3\bar{3}\bar{3}(\hat{p}) - (\hat{p})\bar{4} + 3\pi\pi = \Sigma + K. \quad (D2)$$

The excitation $\bar{3}\bar{3}\bar{3}$ is the excitation which appears in meson resonances as the ρ meson ($3\bar{3}3 \rightarrow \bar{S}\bar{S}$). Since no core spinor-flip is involved in reaction (D2), the Σ is produced with isotopic spin $I=1$. Typical decay processes of the Σ are

$$\begin{aligned} \Sigma &= (\hat{p})\bar{4} = (\hat{p}) \bar{M} \bar{M} \bar{M} \bar{M} \rightarrow (\hat{p}) \langle \bar{M} \rangle \bar{M} \langle \bar{M} \rangle \bar{M} \rightarrow (\hat{p}) [M \bar{M}] M \bar{M} \\ &\quad = p + \pi \\ &\quad - (\hat{\Lambda}) [\bar{M}] \bar{M} \bar{M} \bar{M} + \gamma = \Lambda + \gamma. \end{aligned}$$

The γ -producing decay, which occurs only in the $I=0$ mode, is shown in Fig. 22.

Since $\Lambda = S\bar{S}\bar{S}\bar{3}$ and $\Sigma = S\bar{S}\bar{S}\bar{4}$, the only other possible strangeness $S_1 = -1$ configuration is $S\bar{S}\bar{S}\bar{7}$. This configuration actually occurs, in the form of the $\Lambda(1402)$ resonance (see Fig. 21 and Table VII):

$$\bar{K} + p \rightarrow (\hat{p}) \bar{3}\pi\pi = (\hat{p}) \bar{7} = \Lambda(1402)S.$$

The $\Lambda(1402)$ has a single decay mode:

$$\begin{aligned} \Lambda(1402) &= (\hat{p})\bar{7} = (\hat{p}) \bar{3} \bar{M} \bar{M} \bar{M} \bar{M} \rightarrow (\hat{p}) \bar{3} \bar{M} [M] \bar{M} M \\ &\quad = (\hat{p})\bar{4} + \bar{M} M = \Sigma + \pi. \end{aligned}$$

4. Ξ -hyperon production

We have seen above that the strangeness $S_1 = -1$ resonances occur in all possible combinations:

$$S\bar{S}\bar{S}\bar{3} = \Lambda, \quad S\bar{S}\bar{S}\bar{4} = \Sigma, \quad S\bar{S}\bar{S}\bar{7} = \Lambda(1402).$$

The main question with regard to mapping the

strangeness $S_1 = -2$ Ξ resonances is to explain why they occur only in the combination

$$S\bar{S}S\bar{3}\bar{3} = \Xi, \quad (D3a)$$

and not in the combinations

$$S\bar{S}S\bar{3}\bar{4} = \Xi' \text{ or } S\bar{S}S\bar{4}\bar{4} = \Xi'' . \quad (D3b)$$

As we show below, the Ξ' and Ξ'' resonance forms

$$\pi + p \rightarrow \pi\{3\bar{3}\bar{3}\bar{3}\cdot\bar{3}\bar{3}\bar{3}\}(\hat{p}) = \pi\bar{3}\bar{3}\bar{3}\bar{3}\bar{3}\bar{3}\bar{3}(\hat{p}) \rightarrow (\hat{\Lambda})\bar{3}\bar{3} + 3\pi\pi + 3\pi\pi = \Xi + K + K, \quad (D4)$$

$$\bar{K} + p \rightarrow \bar{3}\pi\pi\{3\bar{3}\}(\hat{p}) \rightarrow (\hat{\Lambda})\bar{3}\bar{3} + 3\pi\pi = \Xi + K. \quad (D5)$$

In order to produce the Ξ' and Ξ'' hyperons, which are not observed experimentally, we would have to have associated-production reactions of the types shown below:

$$\pi + p \rightarrow \pi\{\bar{3}\bar{3}\bar{3}\bar{3}\pi\cdot\bar{3}\bar{3}\pi\}(\hat{p}) = \pi\bar{3}\bar{3}\bar{3}\bar{3}\bar{3}\bar{3}\bar{3}\pi(\hat{p}) \rightarrow (\hat{\Lambda})\bar{3}\bar{4} + 3\pi\pi + 3\pi\pi = \Xi' + K + K. \quad (D6)$$

$$\pi + p \rightarrow \pi\{\bar{3}\bar{3}\bar{3}\bar{3}\pi\cdot\bar{3}\bar{3}\bar{3}\}(\hat{p}) = \pi\bar{3}\bar{3}\bar{3}\bar{3}\bar{3}\bar{3}\bar{3}\bar{3}(\hat{p}) \rightarrow (\hat{\Lambda})\bar{4}\bar{4} + 3\pi\pi + 3\pi\pi = \Xi'' + K + K. \quad (D7)$$

$$\bar{K} + p \rightarrow \bar{3}\pi\pi\{\bar{3}\bar{3}\pi\}(\hat{p}) \rightarrow (\hat{\Lambda})\bar{4}\bar{4} + 3\pi\pi = \Xi'' + K + K. \quad (D8)$$

The excitations $\{\bar{3}\bar{3}\bar{3}\pi\cdot\bar{3}\bar{3}\pi\}$ and $\{\bar{3}\bar{3}\bar{3}\pi\cdot\bar{3}\bar{3}\bar{3}\}$ in (D6) and (D7), respectively, are both mixed excitations, and the experience with meson resonances (see the discussion in paper I) suggests that these mixed excitations occur with very small cross sections. Also, the excitation $\{\bar{3}\bar{3}\bar{3}\pi\cdot\bar{3}\bar{3}\bar{3}\}$ in (D7), which contains two $\bar{3}\bar{3}\bar{3}$ combinations, is not allowed by rule (5). The excitation $\{\bar{3}\bar{3}\pi\}$ in (D8) has nonzero strangeness, and hence is not allowed by rule (3). Thus we can see that the non-observance of the cascade resonances Ξ' and Ξ'' of Eq. (D3b) is simply explained in terms of the requisite excitation mechanisms.

The dominant Ξ decay mode is

$$\Xi = S\bar{S}S\bar{3}\bar{3} = S\bar{S}S\bar{3}\bar{M}\bar{M}\bar{M} \rightarrow S\bar{S}S\bar{3}[\bar{M}]\langle\bar{M}\rangle\bar{M} = S\bar{S}S\bar{3} + M\bar{M} = \Lambda + \pi.$$

$$\bar{K} + p \rightarrow \bar{3}\pi\pi\{3\bar{3}\pi\cdot\bar{3}\bar{3}\pi\}(\hat{p}) \rightarrow (?)\bar{3}\bar{3}\bar{3} + 3\pi\pi + 3\pi\pi = \Omega' + K + K. \quad (D9)$$

A possible reaction for producing the Ω (but see the discussion below) is

$$\bar{K} + p \rightarrow \bar{3}\pi\pi\{\bar{3}\bar{3}\bar{3}\cdot\bar{3}\bar{3}\bar{3}\}(\hat{p}) = \bar{3}\pi\pi\bar{3}\bar{3}\bar{3}\bar{3}\bar{3}\bar{3}(\hat{p}) \rightarrow (?)\bar{3}\bar{4}\bar{4} + 3\pi\pi + 3\pi\pi = \Omega + K + K. \quad (D10)$$

Since only 41 Ω particles have been observed,¹³ the occurrence of (D10) but not (D9) might be explainable in terms of cross sections. In meson resonances, the $3\bar{3}\bar{3}\cdot\bar{3}\bar{3}\bar{3}$ excitation leads to the dominant D meson, which has been observed in $p\bar{p}$ experiments and as a prominent peak in several missing-mass experiments. The $3\bar{3}\pi\cdot\bar{3}\bar{3}\pi$ excitation, on the other hand, leads only to the very weak $X^0(1148)$ and $X^-(1153)$ meson resonances of Fig. 19 (plus some stronger overlying rotational

can be ruled out on the basis of the unnatural excitation processes that would be required. The resonance configuration $S\bar{S}S\bar{3}\bar{7}$ has a calculated mass $\Xi^0(1315) + 280 = \Xi^0(1595)$, and hence seems identifiable with the $\Xi^0(1606)$ resonance shown in Fig. 16.

Two associated production reactions for the Ξ are

The decay mode

$$\Xi = S\bar{S}S\bar{3}\bar{M}\bar{M}\bar{M} \rightarrow S\bar{S}S\bar{3}\bar{M}\langle\bar{M}\rangle\bar{M} = S\bar{S}S\bar{4} + M\bar{M} = \Sigma + \pi$$

is not allowed, because the transformation $\langle\bar{M}\rangle \rightarrow \bar{M}$ can only take place in cases where an annihilation has occurred (e.g., $[M]$ or $[3]$), or where a secondary particle scattering has occurred (K_S^0 regeneration).

5. Ω -hyperon production

One puzzle about the Ω hyperon is to understand why it appears as the configuration $\Omega = S\bar{S}S\bar{3}\bar{4}\bar{4}$, but not as the configuration $\Omega' = S\bar{S}S\bar{3}\bar{3}\bar{3}$. The Ω' seemingly should be produced in the reaction

levels, as shown in paper I). However, reaction (D10) has a difficulty. The excitation shown in (D10) is $\bar{3}\bar{3}\bar{3}\cdot\bar{3}\bar{3}\bar{3}$ and not $\bar{3}\bar{3}\bar{3}\cdot\bar{3}\bar{3}\bar{3}$. Rule (5) states that this form of asymmetric excitation is not allowed. The way out of this difficulty relates to an interesting experimental observation. Although the excitation $\bar{3}\bar{3}\bar{3}\cdot\bar{3}\bar{3}\bar{3}$ is not allowed, rule (5) states that the excitation $\bar{3}\bar{3}\bar{3}\cdot\bar{3}\bar{3}\bar{3}\cdot\bar{3}\bar{3}\bar{3}$ is allowed. Suppose that instead of (D10), we have the following two-step process for the production

of the Ω :

$$\bar{K} + p \rightarrow \bar{K} \{ \bar{3} \bar{3} \bar{3} \cdot 3 \ 3 \ 3 \cdot \bar{3} \bar{3} \bar{3} \} \rightarrow K + \bar{N} N \bar{N}, \quad (D11a)$$

where $\bar{N} N \bar{N}$ is a strangeness $S = -2$ nucleon-triplet type of excitation which has the decay mode

$$\bar{N} N \bar{N} \rightarrow \Omega + K. \quad (D11b)$$

There are two different experimental results which, when taken together, suggest that the reaction sequence (D11a) – (D11b) may actually occur: (1) The excitation $333 \cdot 333 \cdot 333$ leads via the transition $333 \cdot 333 \cdot 333 \rightarrow SSSSSS$ to the Syracuse²⁴ $N \bar{N}$ bound state (Fig. 11), with a mass of about 1800 MeV, so that a nucleon triplet $\bar{N} N \bar{N}$ would have a mass of about 2700 MeV; (2) in one Ω^- experiment,³⁵ the experimenters noted that five of the $K^- p \rightarrow \Omega^- K^+ K^0$ events were of the type

$$K^- p \rightarrow K^+ + \Xi^- (\sim 2700 \text{ MeV}),$$

$$\Xi^- (\sim 2700) \rightarrow \Omega^- + K^0,$$

which is just the sequence we have shown in (D11a) and (D11b).

As we have outlined hyperon-excitation mechanisms thus far in the present paper, the first-class strangeness S_1 has been attributed solely to spinless quanta, and hyperon excitations are assumed to occur via the binding of strange *spinless* excitation quanta to the invariant $S \bar{S} S$ hyperon spinor core. However, if a strange excitation

unit 333 can make the transition $333 \rightarrow SS$ (Appendix C) and then bind to the spinor core $S \bar{S} S$, we can have a case where the hyperon excitation is via the binding of strange *spinors* to the $S \bar{S} S$ spinor core. There are three examples which suggest that excitation spinors with first-class strangeness may exist: (1) The Ω production mode (D11a) and (D11b) just discussed; (2) the $\Lambda(1518)D$ resonance, whose anomalously low mass can be reproduced by a strangeness $S_1 = -1$ $S \bar{S}$ spinor pair bound to the $S \bar{S} S$ spinor core ($\hat{\Lambda}$); (3) the $K^*(892)$ kaon resonance, which is the configuration $SS\pi$ in an $L = 1$ rotational mode (paper I), and in which the first-class strangeness of the resonance may be carried by the SS spinor pair. However, with only three such widely spaced examples as these, it is difficult to incorporate these results into the general systematics of the theory, at least in its present state of development.

APPENDIX E: A MODEL FOR THE MUON

In the present paper we have defined a light-quark geometric model which reproduces the strongly interacting hadron resonances, and in which absolute masses, spin angular momenta, and magnetic moments occur as calculated quantities. By a straightforward extension of these results, we can produce a similar model for the muon. This model is illustrated in Fig. 28.

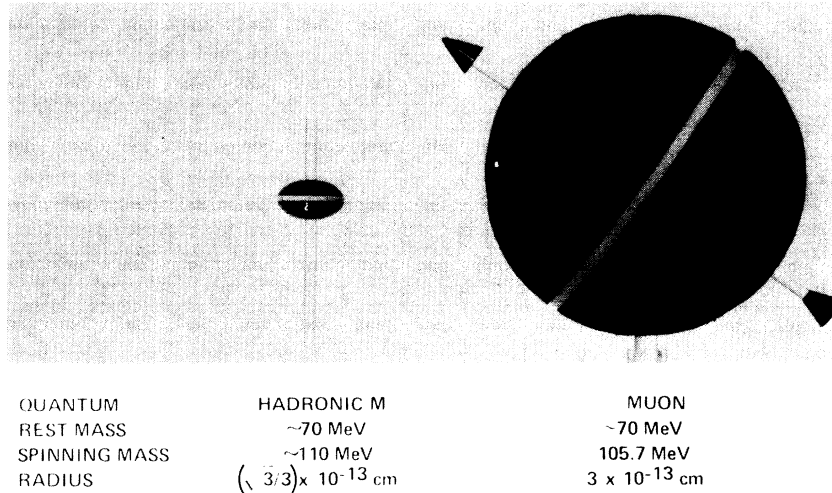


FIG. 28. The mass quantum $M = 70$ MeV as it appears in hadronic states (see Fig. 1) and as it appears in the muon (Appendix E). The stripe in each case represents an equatorial charge distribution, where the equatorial radii are the values quoted in the figure. The model shown here for the muon gives all of its first-order properties correctly as *calculated* quantities—namely, the mass, the spin angular momentum J , and the magnetic moment μ . The angle of inclination with respect to the vertical z direction shown for the muon is the angle that projects $J = [\frac{1}{2}(\frac{1}{2} + 1)]^{1/2} \hbar = (\frac{1}{2}\sqrt{3}) \hbar$ onto $J_z = \frac{1}{2} \hbar$ and $\mu = \sqrt{3} e \hbar / 2mc$ onto $\mu_z = e \hbar / 2mc$, as is required quantum-mechanically, where z is the axis of quantization. Although the equatorial charge distribution of the muon gives rise to an intrinsic electric quadrupole moment, this angle of inclination causes the quadrupole moment to vanish identically along the z (vertical) axis, and the precessional motion about the z axis causes the quadrupole moment to average out to zero along the x and y axes over one cycle of precession. This result is important, since quantum mechanics does not allow an *observable* quadrupole moment for the muon (but see Ref. 36).

From Eq. (B6) in Appendix B, a relativistically spinning sphere, with its equator moving at or near the velocity of light, becomes half again as massive as it was at rest. Thus a spherical 70-MeV rest mass will become a 105-MeV spinning sphere as observed in the laboratory frame of reference. If the radius of the sphere is set equal to its Compton wavelength, $R = \hbar/mc$, then from Eq. (B12) the calculated spin angular momentum is $J = \frac{1}{2}\hbar$, and from Eq. (B10) the calculated magnetic moment is $\mu = e\hbar/2mc$, where we assume an equatorial charge distribution.

The one difficulty with this model for the muon is that the equatorial charge distribution gives rise to an electric quadrupole moment, which quantum-mechanically is not allowed for a spin- $\frac{1}{2}$ particle. However, if the spinning muon is tipped on its axis and given a precessional motion, there is one angle between the spin axis and the axis of precession for which this difficulty vanishes, and this angle happens to be the same as the angle that is assumed in the usual quantum-mechanical formulation of the muon. This is the angle $\theta = \cos^{-1}(1/\sqrt{3})$. At that angle, the z component of the electric quadrupole moment, which is proportional to $P_2(\cos\theta)$, vanishes identically; also, the x and y components, which are proportional to $P_2(\cos\psi)$, where $\cos\psi = \sin\theta\cos\phi$, with ϕ the

angle of precession, average out to zero over one cycle of ϕ rotation (if the sphere is stationary³⁶). At this tipped angle for the spinning sphere, the radius of the sphere must be increased by a factor of $\sqrt{3}$ so as to obtain the projected quantities $J_z = \frac{1}{2}\hbar$ and $\mu_z = e\hbar/2mc$, as required experimentally. The total calculated angular momentum is then $J = [\frac{1}{2}(\frac{1}{2} + 1)]^{1/2}\hbar = (\frac{1}{2}\sqrt{3})\hbar$, and the total calculated magnetic moment is $\mu = \sqrt{3}e\hbar/2mc$. Thus we have obtained the quantum-mechanical value $[J(J+1)]^{1/2}\hbar$ for the total spin of the muon by requiring that the electric quadrupole moment of the muon must vanish.

In Fig. 28, the 70-MeV hadronic mass quantum M of Fig. 1 and the 70-MeV mass M_μ whose spinning configuration represents the muon are shown with their correct relative sizes. As can be seen, although M and M_μ are both 70-MeV quanta, M_μ appears in a considerably expanded geometry. Thus, although M and M_μ seem undeniably related, as for example in the dominant decay mode

$$\pi \rightarrow \mu + \nu, \quad M\bar{M} \rightarrow M[\bar{M}] + \nu = M_\mu + \nu,$$

they are geometrically quite different forms of the basis 70-MeV mass quantum. Hence in this hadronic light-quark model, we are not simply "coloring the quark muon."³⁷

*Work performed under the auspices of the U. S. Atomic Energy Commission.

¹M. H. Mac Gregor, Phys. Rev. D **9**, 1259 (1974).

²It should be noted that from the present light-quark systematics, the broad-width ϵ and S^* meson resonances are $^{2S+1}L_J = ^3P_0$ rotational levels rather than S states. From the classification of hadron resonances in Ref. 1, it is quite clear experimentally that S -wave resonances have narrower widths than rotational levels.

³A caber is a linear structure (beam) whose main utility lies in its inertial properties.

⁴E. Fermi and C. N. Yang, Phys. Rev. **76**, 1739 (1949).

⁵M. Gell-Mann, Phys. Lett. **8**, 214 (1964); G. Zweig, CERN Reports Nos. TH 401 and TH 412, 1964 (unpublished).

⁶The levels in Figs. 5 and 19 are shown as different isotopic-spin states of the same basic resonance structures. However, whereas the pions have comparable cross sections and thus constitute a conventional isotopic-spin multiplet, the resonances around 960 MeV have radically different cross sections and are not isotopic-spin partners in the usual sense. In general, charged modes of narrow-width meson resonances have much smaller cross sections than the corresponding neutral modes (see the resonances in Fig. 19).

⁷B. Maglich *et al.*, Phys. Rev. Lett. **27**, 1479 (1971).

⁸M. Aguilar-Benitez *et al.*, Phys. Rev. D **6**, 29 (1972).

⁹D. L. Cheshire *et al.*, Phys. Rev. Lett. **28**, 520 (1972).

¹⁰B. T. Feld, *Models of Elementary Particles* (Blaisdell, Waltham, 1969), p. 338.

¹¹J. Fox *et al.*, Phys. Rev. Lett. **31**, 1084 (1973);

B. L. Roberts, *ibid.* **32**, 1265 (1974). These results are based in part on an incompletely described statistical analysis, and the physical significance of the error limits thus obtained does not appear to be clear-cut.

¹²R. L. Cool *et al.*, Phys. Rev. Lett. **29**, 1630 (1972).

¹³M. Deutschmann *et al.*, Nucl. Phys. **B61**, 102 (1973).

¹⁴Feld, Ref. 10.

¹⁵M. Goldhaber, Phys. Rev. **101**, 437 (1953).

¹⁶L. J. Gutay *et al.* [Nucl. Phys. **B27**, 486 (1971)] noted a four-standard-deviation dip in $\pi\pi$ amplitudes right at 560 MeV.

¹⁷M. H. Mac Gregor, Nuovo Cimento **8A**, 235 (1972).

¹⁸W. Kienzle (*MMS*, 1967), CERN report, 1972 (unpublished).

¹⁹M. Basile *et al.* (BCS Collaboration, Nuovo Cimento Lett. **4**, 838 (1970) (see Fig. 8 in Ref. 17).

²⁰Bonn-Durham-Nijmegen-Paris (E.P.)-Torino (BDNPT) Collaboration, Nucl. Phys. **B16**, 221 (1969).

²¹K. W. J. Barnham *et al.*, Phys. Rev. Lett. **26**, 1494 (1971).

²²I. J. Bloodworth *et al.*, Nucl. Phys. **B37**, 203 (1972), who comment as follows: "The appearance of some structure in this and in two other experiments (Barnham and BDNPT) could clearly be due to statistical fluctua-

tions, although it seems surprising that the effect occurs in the same few bins." These are the same bins in which the Kienzle dip still persists and in which the Crennell peak appears.

²³D. J. Crennell *et al.*, Phys. Rev. Lett. 20, 1318 (1968).

²⁴T. A. Lasinski *et al.*, Rev. Mod. Phys. 45, No. 2 (1973) Part II.

²⁵Particle Data Group, Phys. Lett. 50B, 1 (1974).

²⁶C. A. Rey *et al.*, Phys. Rev. Lett. 32, 908 (1974).

²⁷J. Arvieux, Nucl. Phys. A221, 253 (1974).

²⁸M. H. Mac Gregor, Nuovo Cimento 18A, 169 (1973).

²⁹C. Defoix *et al.*, Nucl. Phys. B44, 125 (1972).

³⁰H. W. Atherton *et al.*, Phys. Lett. 43B, 249 (1973).

³¹A. F. Garfinkel *et al.*, Phys. Rev. Lett. 29, 1477 (1972).

³²M. H. Mac Gregor, Nuovo Cimento 20A, 471 (1974).

³³See the end of the "note added in proof" in Ref. 17.

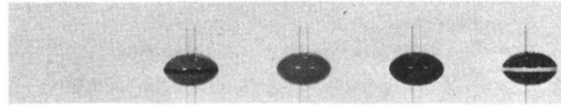
³⁴For the spin of the H meson, see the report by G. Goldhaber, in *Proceedings of the Thirteenth International Conference on High Energy Physics, Berkeley, 1966* (Univ. of California Press, Berkeley, 1967).

³⁵P. F. Schultz *et al.*, Phys. Rev. 168, 1509 (1968).

³⁶If a relativistically spinning sphere is given a translational motion, the addition of velocity vectors unbalances the spinning sphere and causes it to precess around the linear velocity vector. It can be shown that the longitudinal wavelength for this precession is identifiable with the de Broglie wavelength. With this interpretation, if a longitudinally precessing muon in a crystal satisfies the Bragg condition, then the x and y components of the electric quadrupole moment will *not*

cancel out on the average over a cycle of precession, and an observable multiple-scattering effect can be produced. An interesting paradox arises if we attribute the de Broglie wavelength of the muon to this type of longitudinal precession. The paradox arises in connection with the neutron, which is a composite particle and yet which satisfies the same de Broglie equation, and hence has the same type of longitudinal precession as the spherical muon. A conceptual solution to this paradox is to say that each quark in the neutron separately precesses in a spherical manner when the neutron has a translational velocity. However, this solution raises another difficulty, because it introduces an extraneous factor of three into the equation for the neutron de Broglie wavelength (by using the quark mass instead of the neutron mass). But if the muon has a total spin $J = (\frac{1}{2}\sqrt{3})\hbar$, and if a neutron quark has a total spin $J = \frac{1}{2}\hbar$, then the extraneous factor of three in the neutron de Broglie equation is removed, and we have resolved the paradox. The interesting point about this paradox in connection with the present paper is that from the considerations described in Fig. 28, the muon must have a total spin $J = (\frac{1}{2}\sqrt{3})\hbar$, and from the size of a nucleon quark as determined in Appendix B, the quark has a total spin $J = \frac{1}{2}\hbar$. Hence the resolution of this paradox about de Broglie wavelengths is a natural concomitant of the present light-quark systematics.

³⁷G. R. Kalbfleisch and E. C. Fowler, Nuovo Cimento 19A, 173 (1974).



QUANTUM	M^+	M^0	\bar{M}^0	M^-
MASS (MeV)	74.6	70.0	70.0	74.6
CHARGE	+e	0	0	-e

FIG. 1. The fundamental mass quantum $M \sim 70$ MeV. M appears to have the same quantum numbers as the K meson; in particular, it has isotopic spin $I = \frac{1}{2}$, spin angular momentum $J=0$ (it also appears as the spinning quantum M_s in the spinor S), and strangeness $S = \pm 1$. The shape of the quantum M is that of an oblate spheroid, with radii $R_{\max} \simeq \frac{1}{3}\sqrt{3} F$ and $R_{\min} \simeq \frac{1}{3} F$, as determined in Appendix B. As shown in Fig. 2, the quantum M occurs in its spinless form in the basis states $1 \equiv M$, $3 \equiv 3M$, $4 \equiv 4M$, and $7 \equiv 7M$, and it occurs in its spinning form in the spinor $S \equiv 3M_s$. Although the spinless quantum $M \sim 70$ MeV has not been observed experimentally, the spinning quantum M_s is related phenomenologically by the equations of special relativity to the readily observed muon (see Appendix E and Fig. 28).

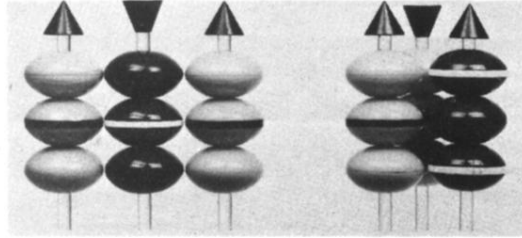


FIG. 10. The proton and neutron. These are both formed as Fermi-Yang (Ref. 4) spinor clusters $N = S\bar{S}S$. The internal charge assignments for the nucleons follow uniquely from the requirement of reproducing the following experimental data: the total charges, the magnetic moments, the spins, the mass difference, and the zero electric dipole moment for the neutron about its spin axis. From their resultant electromagnetic interactions, the proton appears with a linear $S\bar{S}S$ configuration and the neutron with a clustered $\bar{S}S\bar{S}$ configuration. The nucleon values that are reproduced from the parameters of Table I are the following:

	Proton	Neutron
Spinor configuration	$S\uparrow S\uparrow S\uparrow$ (linear)	$S\uparrow S\downarrow S\uparrow$ (clustered)
Intrinsic mass (MeV)	991.8	998.1
hadronic binding energy	-54.6	-54.6
magnetic binding energy	+3.4	-1.7
Coulomb binding energy	-2.2	-2.1
Calculated mass	938.4 MeV	939.7 MeV
Experimental mass	938.4 MeV	939.6 MeV
Calculated magnetic moment	+2.79 μ_N	-1.86 μ_N
Experimental magnetic moment	+2.79 μ_N	-1.91 μ_N

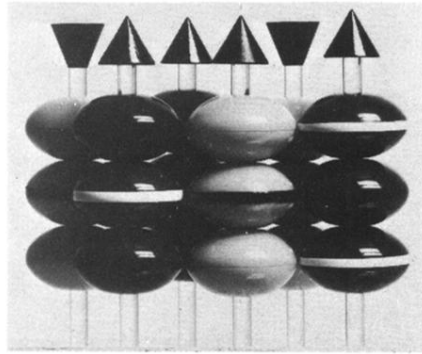


FIG. 11. The $\bar{p}n$ bound state. The same parameters that reproduce the proton and neutron also reproduce the $\bar{p}n$ bound state. The $\bar{p}n$ cluster shown here is a spin-1 configuration, as suggested by the experimental data.

Spinor configuration	$S_{\uparrow}^{-}S_{\uparrow}^{+}S_{\uparrow}^{-}S_{\uparrow}^{+}S_{\uparrow}^{-}S_{\uparrow}^{+}$
Intrinsic mass (MeV)	1989.9
hadronic binding energy	-191.1
magnetic binding energy	+1.7
Coulomb binding energy	-5.6
Calculated mass	1794.9 MeV
Experimental mass	1794.5 ± 1.4 MeV

The Coulomb corrections for Figs. 10-15 are discussed in Sec. IV and summarized in Table I.

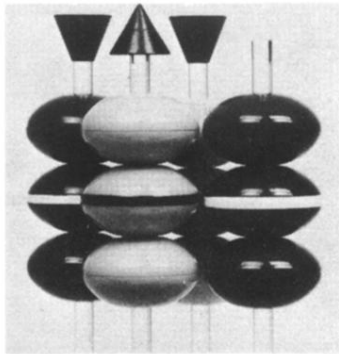


FIG. 12. The Λ hyperon. The Λ is the caber cluster $\bar{S}_S^S \bar{3}$, in which the anticaber $\bar{3}$ carries the strangeness quantum number $S = -1$. Calculated values for the Λ are the following:

Caber configuration	$S_{\uparrow}^{\uparrow} S_{\uparrow}^{\uparrow} S_{\uparrow}^{\uparrow} \bar{3}^{-}$
Intrinsic mass (MeV)	1206.4
hadronic binding energy	- 84.6
magnetic binding energy	- 1.7
Coulomb binding energy	- 3.2
Calculated mass	1116.9 MeV
Experimental mass	1115.6 MeV
Calculated magnetic moment	- 0.93 μ_N
Experimental magnetic moment	(- 0.67 \pm 0.06) μ_N

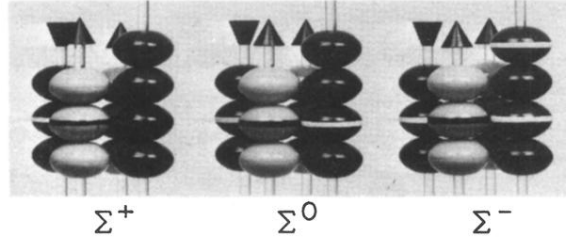


FIG. 13. The Σ hyperons. The Σ hyperons are caber clusters $\bar{S}_3^3\bar{4}$, in which the anticaber $\bar{4}$ carries the strangeness quantum number $S=-1$. The configurations shown here reproduce the masses and charge splittings correctly. The Σ^+ magnetic moment is correctly reproduced. The calculated Σ^- magnetic moment is in disagreement with a recent measurement (Ref. 11). The magnetic moment of the Σ^0 has not measured, but the Σ^0 cluster shown here and the Λ cluster of Fig. 12 correctly reproduce the Q value of the observed decay mode $\Sigma^0 \rightarrow \Lambda + \gamma$ (see Fig. 22).

	Σ^+	Σ^0	Σ^-
Caber configuration	$S_1^\dagger S_2^\dagger S_3^\dagger \bar{4}^0$	$S_1^\dagger S_2^\dagger S_3^\dagger \bar{4}^-$	$S_1^\dagger S_2^\dagger S_3^\dagger \bar{4}^-$
Intrinsic mass (MeV)	1271.8	1276.4	1281.0
hadronic binding energy	-84.6	-84.6	-84.6
magnetic binding energy	+5.1	+5.1	+5.1
Coulomb binding energy	-1.4	-3.2	-3.3
Calculated mass (MeV)	1190.9	1193.7	1198.2
Experimental mass (MeV)	1189.4	1192.5	1197.3
Calculated charge splitting (MeV)	2.8	4.5	
Experimental charge splitting (MeV)	3.1	4.8	
Calculated magnetic moment	$+2.79\mu_N$	$+2.79\mu_N$	$+2.79\mu_N$
Experimental magnetic moment	$(+2.59 \pm 0.46)\mu_N$...	$(-1.48 \pm 0.37)\mu_N$ (Ref. 11)

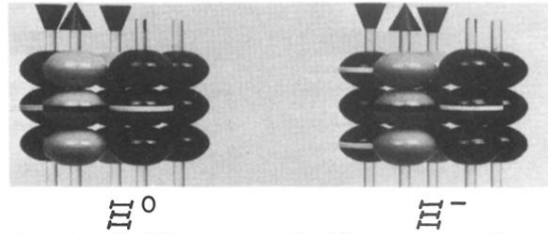


FIG. 14. The Ξ hyperons. The Ξ hyperons are the caber clusters

$$\bar{S} \begin{matrix} S \\ \bar{3} \\ \bar{3} \end{matrix},$$

in which the two anticabers $\bar{3}\bar{3}$ carry the strangeness quantum $S=-2$. In order to reproduce the large charge splitting for this hyperon resonance, we must, as in the case of the proton and neutron, form the second charge state by using a doubly charged spinor S^- . This leads to the prediction that the Ξ^- and the neutron have comparable magnetic moments, in contrast to the SU(6) prediction that the Ξ^- and Λ have comparable magnetic moments. A recent experimental result (Ref. 12) is in agreement with the present prediction. The Ξ^0 magnetic moment is unknown.

	Ξ^0	Ξ^-
Caber configuration	$S^\dagger S^\dagger S^\dagger \bar{3} \bar{3}^0$	$S^\dagger S^\dagger S^\dagger \bar{3} \bar{3}^-$
Intrinsic mass (MeV)	1416.4	1422.7
hadronic binding energy	-99.6	-99.6
magnetic binding energy	-1.7	-1.7
Coulomb binding energy	-3.2	-3.3
Calculated mass	1311.9 MeV	1318.1 MeV
Experimental mass	1314.9 MeV	1321.3 MeV
Calculated charge splitting		6.2 MeV
Experimental charge splitting		6.4 MeV
Calculated magnetic moment	$-0.93\mu_N$	$-1.86\mu_N$
Experimental magnetic moment	...	$(-1.93 \pm 0.75)\mu_N$ (Ref. 12)

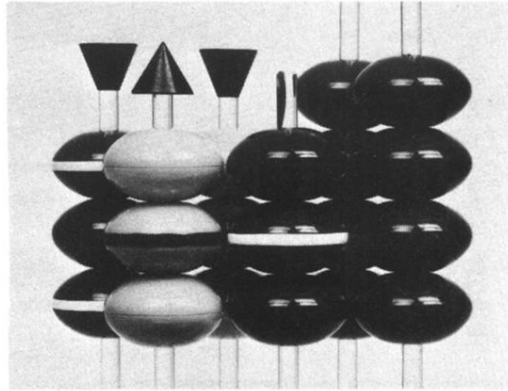
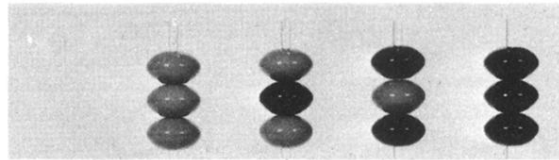


FIG. 15. The Ω^- hyperon. The Ω is the caber cluster

$$\bar{S}_S^S \bar{S}_4^{\bar{4}},$$

in which the three anticabers $\bar{3}\bar{4}\bar{4}$ carry the strangeness quantum number $S = -3$. The spin of the Ω has not been measured. Since the $\Omega^- - \Xi^-$ mass difference is 350.9 MeV, almost precisely equal to 5×70.0 MeV, we have assigned the Ω^- the same spinor-triplet configuration as the Ξ^- . In a similar pairing of resonances, the $\Lambda(1402.4) = p7^-$ and $\Sigma^0(1192.5) = p4^-$ resonances have a mass difference of 209.9 MeV, almost precisely equal to 3×70.0 MeV.

Caber configuration	$S\bar{\uparrow}S\bar{\uparrow}S\bar{\uparrow}3^-4^0\bar{4}^0$
Intrinsic mass (MeV)	1772.7
hadronic binding energy	-99.6
magnetic binding energy	-1.7
Coulomb binding energy	-3.3
Calculated mass	1668.1 MeV
Experimental mass	1672.2 MeV (Ref. 13)



CABER	3	$\bar{3}$	$\frac{3}{2}$	$\frac{\bar{3}}{2}$
STRANGENESS	+1	0	0	-1
HADRONIC B.E.	$\sim 4\%$	~ 0	~ 0	$\sim 4\%$

FIG. 17. Strange and nonstrange forms of the caber 3. Phenomenologically, the relationship between strangeness quantum numbers and binding energies that is established here is one of the most important results of the present systematics: strange quanta have HBE $\sim 4\%$, and nonstrange quanta have HBE $\sim 0\%$. These caber properties are summarized in Table II. In Sec. IV it is demonstrated experimentally that strange and nonstrange basis states have the same intrinsic masses.

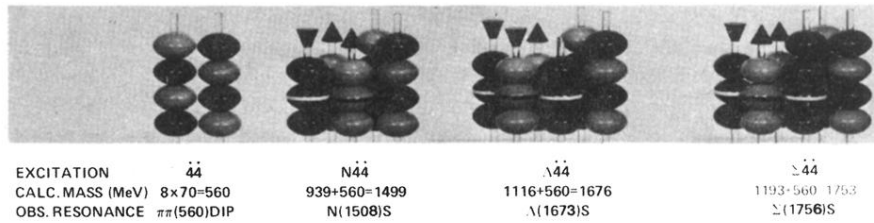


FIG. 18. The nonstrange caber pair $\bar{4}\bar{4}$, which appears with zero hadronic binding energy. Evidence for direct $\bar{4}\bar{4} = 560$ MeV resonance effects in meson amplitudes is weak (Ref. 16), but the $N\bar{4}\bar{4}$, $\Lambda\bar{4}\bar{4}$, and $\Sigma\bar{4}\bar{4}$ resonances are dominant and easily observed baryon and hyperon S states. The mass values shown here indicate that the zero-binding-energy approximation for these excitations is accurate.

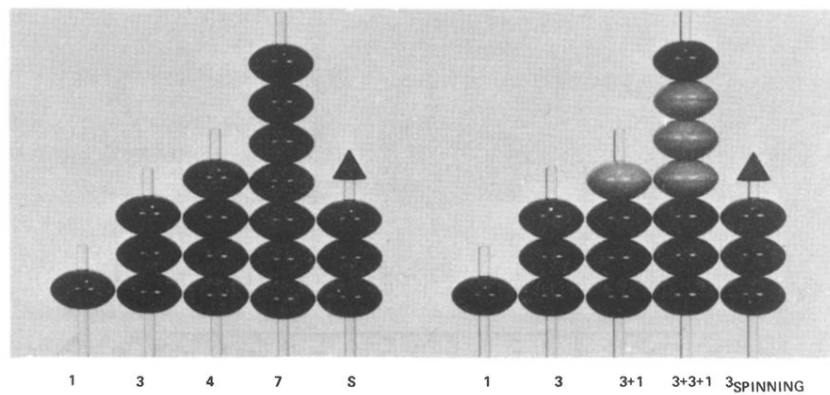


FIG. 2. The cabers 1, 3, 4, 7, S. These are formed as linear arrays of quanta M . The linear arrays account in an apparently unique manner for a number of phenomenologically required light-quark binding energy characteristics and electromagnetic characteristics, as is summarized in Table IV. These linear arrays occur both as cabers (strangeness = +1) and as anticabers (strangeness = -1), and hadronic binding energies exist only between caber-anticaber pairs. In hyperon resonances, which are formed by adding spinless anticabers to an existing nucleon spinor triplet, it is the spinless anticabers which carry the conventional strangeness quantum numbers; the conservation of baryon number is precisely equivalent to the conservation of nucleon spinor triplets, so that the strangeness of the spinor triplet, and hence also of the spinor S, does not enter into the bookkeeping of the associated-production process. Thus the spinor S is assigned a strangeness quantum number of zero, although from its hadronic binding energy it is in fact "strange." In Sec. III, "nonstrange" forms of the cabers 3, 4, and S are also described. The mass of a caber is the sum of the masses of the constituent subquanta M . The properties of the cabers 1, 3, 4, 7, S are summarized in Table II, and the spinor S is discussed in detail in Appendix B.

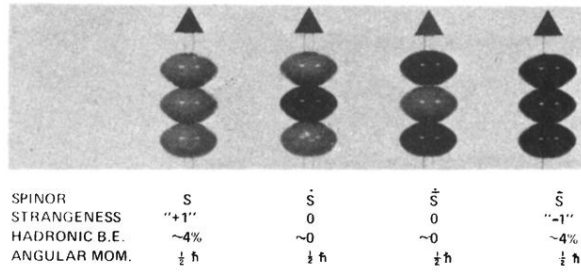


FIG. 20. Strange and nonstrange forms of the spinor S . Figures 17 and 20 show analogous characteristics for the spinless caber 3 and the spinor S . The fundamental spinor-pair production and decay transition $333 \leftrightarrow SS$ is discussed in Appendix C. This transition gives an explanation for the quantization of spin angular momentum, and it leads to a fundamental spin and isotopic-spin selection rule: $\tilde{S}\tilde{S}$ spinor pairs occur either as $J=1, I=0$ or as $J=0, I=1$ configurations. Spinors S occur in hadron resonances in a very distinctive manner, namely as $S\bar{S}$ and $\tilde{S}\tilde{\bar{S}}$ spinor triplets in baryon resonances and as $\tilde{S}\tilde{\bar{S}}$ and $\tilde{S}\tilde{\bar{S}}\tilde{S}\tilde{\bar{S}}$ pairs and quartets in meson resonances. From their 4% hadronic binding energies, the spinors S and \bar{S} are "strange," but from the invariant nature of $S\bar{S}$ triplets, this strangeness is an invariant (and therefore ignorable) in associated-production reactions. Thus we formally assign to the spinors S and \bar{S} a strangeness $S=0$. As is shown in Sec. IV, strange and nonstrange spinors have the same intrinsic masses, and as is shown in Appendix B, the spin angular momentum $J=\frac{1}{2}\hbar$ is a calculated quantity.

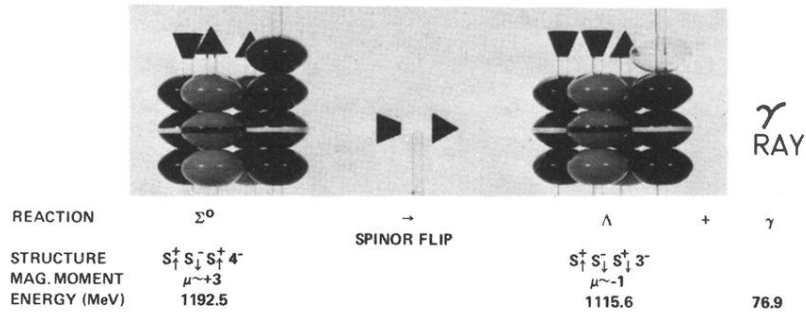


FIG. 22. An empirical determination of the SS spinor-pair magnetic interaction energy from the decay $\Sigma^0 \rightarrow \Lambda + \gamma$. The Σ^0 and Λ hyperons shown in the figure have identical Coulomb energies. Hence the electromagnetic energy difference of 6.9 MeV indicated in the figure is due to magnetic effects. The Σ^0 has +3 magnetic pairs ($t^+ t^- t^+$), and the Λ has -1 magnetic pair ($t^+ t^- t^+$), where +1 pair denotes a repulsive interaction that contributes positively to the potential energy. Thus the 6.9 MeV of magnetic energy is attributed to the difference $(+3) - (-1) = +4$ magnetic pairs, which gives a magnetic pairing energy of 1.7 MeV per pair.

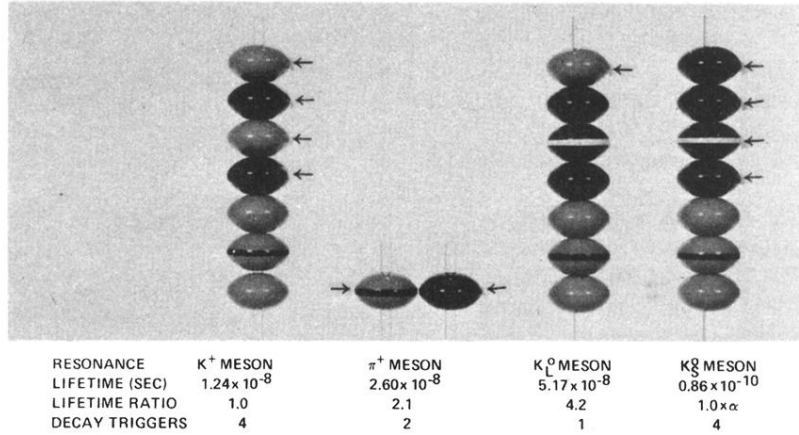


FIG. 23. Lifetime systematics of the K^+ , π^+ , K_L^0 , and K_S^0 mesons. As shown in this figure, the K^\pm , π^\pm , K_L^0 lifetimes form an accurate 1:2:4 lifetime triplet, and the K_S^0 can be grouped into a similar triplet shifted by one power of $\alpha = e^2/\hbar c$. Statistically, these accurate 1:2:4 lifetime ratios can be explained by assuming that 4:2:1 subquanta M are available to independently annihilate and trigger the decays (the author is aware of no other explanation for these lifetime ratios). Possible sets of decay triggers are indicated by the arrows. The anomalously long lifetimes of the resonances are related to the fact that the decays are triggered by the annihilation of single quanta M or \bar{M} , since resonances that contain matching internal $M\bar{M}$ pairs have much shorter lifetimes.

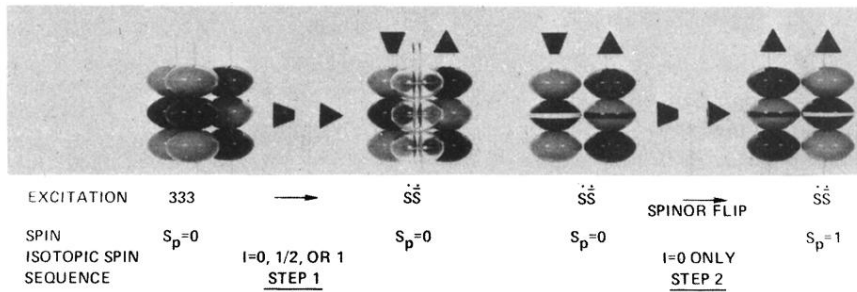


FIG. 25. The fundamental spinor production process $333 \rightarrow \bar{S}S$. This reaction arises from the special relativistic result (Appendix B) that relativistically spinning spheres, with their equators near the velocity of light, are half again as massive as they were at rest. In this figure, we start with the basic excitation cluster 333. One 3 annihilates, and the tangential forces from the annihilation set the other two 3's spinning in opposite directions. In order to conserve energy, they must spin at the full relativistic limit, which leads automatically to the quantization of spin angular momentum, with each spinning 3 having spin angular momentum $J = \frac{1}{2}\hbar$. The spinning 3's constitute the nonstrange spinor pair $\bar{S}S(658)$ (Fig. 19), with total angular momentum $J = S_p = 0$. This is step 1 of Fig. 25. If the $\bar{S}S$ spinor pair is in the charge-symmetric isotopic-spin mode $I=0$ ($\bar{S}^+\hat{S}^-$), it can and does couple to external angular momenta via a photon exchange so as to have a spinor-flip transition and appear with $J = S_p = 1$. This is step 2 of Fig. 25. This two-step process leads to the important spin-isotopic-spin rule for $\bar{S}S$ spinor pairs: $\bar{S}S$ spinor pairs appear either as $J=1, I=0$ or as $J=0, I=1$ configurations. (Note that the $\bar{S}S$ pairs described here are actually $\bar{S}\bar{S}$ pairs; this distinction between the spinors \hat{S} and \bar{S} is usually ignored in the text.)

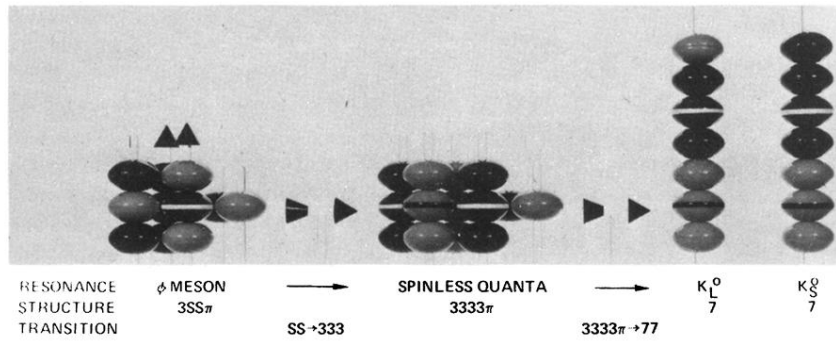


FIG. 26. The decay process $\phi \rightarrow KK$. The ϕ is the narrow-width spin-1 resonance $\phi = 3SS\pi$ (its spin of 1 and its narrow width show that it must contain a spinor pair SS). The kaon is the spinless caber 7 (see Figs. 7 and 9). Since the ϕ contains five quanta M ($\pi 3 = 5M$) plus a spinor pair SS , and the KK final state contains fourteen quanta M ($K = 7M$), the decay process $SS \rightarrow 333 = \text{nine quanta } M$ is unequivocally required. The isotopic spin $I = 0$ and spin angular momentum $J = 1$ of the ϕ meson constitute an example of the $I = 0, J = S_p = 1$ rule of Fig. 25 for SS spinor pairs.

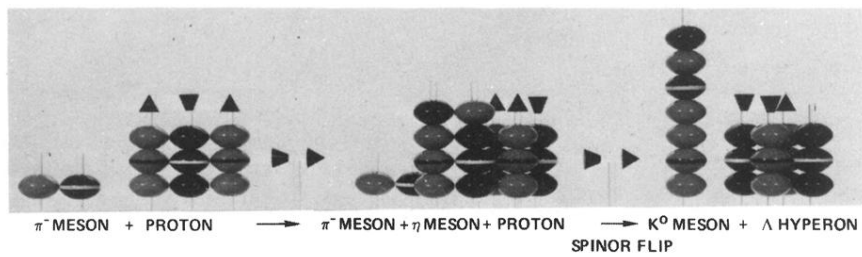
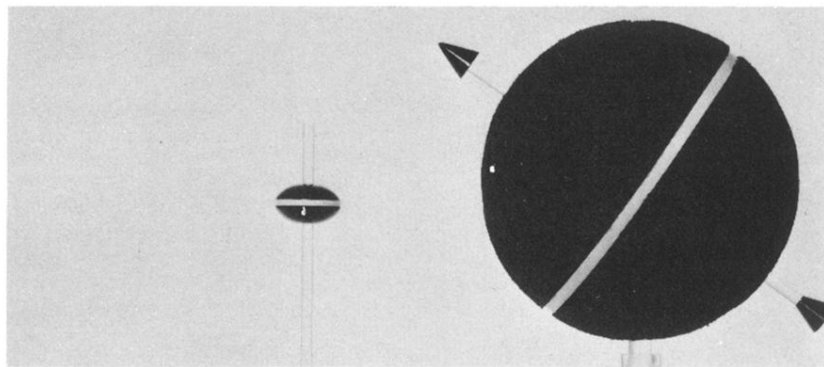


FIG. 27. A graphical display of the production process $\pi^- + p \rightarrow K^0 + \Lambda$. When the π^- strikes the proton, kinetic energy is transformed into hadronic matter in the form of an η meson. The η breaks apart asymmetrically, with one part combining with the π^- and the other part combining with the proton, so as to form a pair of resonances with strangeness +1 and -1, respectively (which is the mechanism of associated production). This production process can be written as the sequence $\pi + p \equiv \pi + S\bar{S}S \rightarrow \pi\{3\bar{3}\pi\}S\bar{S}S \rightarrow S\bar{S}S\bar{3} + 3\pi\pi \equiv \Lambda + K$, where $\{ \}$ is a creation operator.



QUANTUM	HADRONIC M	MUON
REST MASS	~70 MeV	~70 MeV
SPINNING MASS	~110 MeV	105.7 MeV
RADIUS	$(\sqrt{3}/3) \times 10^{-13}$ cm	3×10^{-13} cm

FIG. 28. The mass quantum $M = 70$ MeV as it appears in hadronic states (see Fig. 1) and as it appears in the muon (Appendix E). The stripe in each case represents an equatorial charge distribution, where the equatorial radii are the values quoted in the figure. The model shown here for the muon gives all of its first-order properties correctly as *calculated* quantities—namely, the mass, the spin angular momentum J , and the magnetic moment μ . The angle of inclination with respect to the vertical z direction shown for the muon is the angle that projects $J = [\frac{1}{2}(\frac{1}{2} + 1)]^{1/2} \hbar = (\frac{1}{2}\sqrt{3}) \hbar$ onto $J_z = \frac{1}{2} \hbar$ and $\mu = \sqrt{3} e \hbar / 2mc$ onto $\mu_z = e \hbar / 2mc$, as is required quantum-mechanically, where z is the axis of quantization. Although the equatorial charge distribution of the muon gives rise to an intrinsic electric quadrupole moment, this angle of inclination causes the quadrupole moment to vanish identically along the z (vertical) axis, and the precessional motion about the z axis causes the quadrupole moment to average out to zero along the x and y axes over one cycle of precession. This result is important, since quantum mechanics does not allow an *observable* quadrupole moment for the muon (but see Ref. 36).

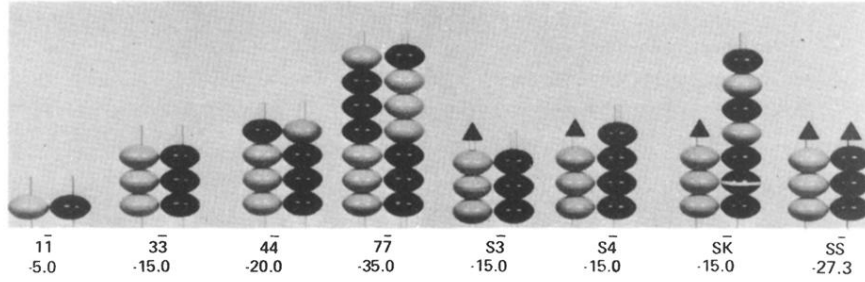


FIG. 3. Hadronic binding energies between caber-anticaber pairs. The hadronic binding, which from its $\sim 4\%$ magnitude is very short-ranged, operates directly between matching M and \bar{M} subquanta in adjacent cabers. Denoting these subquanta as M (nonspinning) and M_s (spinning), the hadronic binding energies between subquanta are as follows: $M\bar{M} = -5.0$ MeV, $M\bar{M}_s = \bar{M}M_s = -5.0$ MeV, $M_s\bar{M}_s = -9.1$ MeV, $MM = \bar{M}\bar{M} = MM_s = \bar{M}\bar{M}_s = M_sM_s = \bar{M}_s\bar{M}_s = 0$. As shown in the figure, the corresponding caber-anticaber binding energies in MeV are as follows: $1\bar{1} = -5.0$, $3\bar{3} = -15.0$, $4\bar{4} = -20.0$, $7\bar{7} = -35.0$, $S\bar{3} = S\bar{4} = S\bar{7} = -15.0$, $S\bar{S} = -27.3$, $SS = \bar{S}\bar{S} = 0$. The mass proportionality of the $1\bar{1}$, $3\bar{3}$, $4\bar{4}$, and $7\bar{7}$ binding energies and the equality of the $S\bar{3}$, $S\bar{4}$, and $S\bar{7}$ binding energies are both phenomenologically required features, and they seem to follow uniquely from the linear caber configurations shown here.

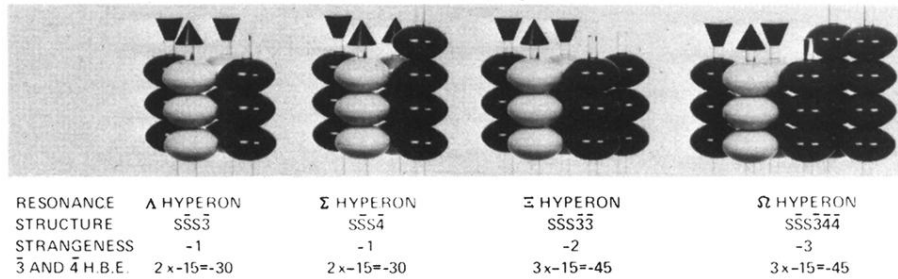


FIG. 4. Hadronic binding energies for clusters of spinless anticabers added to a nucleon core. Due to the very short range of the $\sim 4\%$ hadronic binding energies, only *adjacent* caber-anticaber pairs in a cluster can bind hadronically. When adding spinless anticabers to an $S\bar{S}S$ -triplet nucleon core to form a hyperon resonance, the first $\bar{3}$ or $\bar{4}$ binds with two spinors S to give HBE = -30.0 MeV, the second $\bar{3}$ binds with only one spinor S to give HBE = -15 MeV, and the third anticaber, from its position in the excitation cluster, binds with essentially zero binding energy. As discussed in Fig. 2, the spinless anticabers carry the strangeness quantum numbers of the hyperon resonance. Experimentally, anticabers $\bar{3}$ and $\bar{4}$ will bind to an $S\bar{S}S$ nucleon spinor core to produce Y^* resonances, but cabers 3 and 4 will not bind to this same spinor core to produce Z^* resonances. Thus the particle-antiparticle asymmetry that is inherent in the nucleon spinor core leads to observable consequences. In the present light-quark approach to particle structure, the Fermi-Yang (Ref. 4) formulation of the nucleon, $N = S\bar{S}S$, is required, rather than the Gell-Mann and Zweig (Ref. 5) formulation, $N = SSS$.



RESONANCE	π^+	π^0	π^-
UNBOUND MASS	144.6	140.0	144.6
HADRONIC B. E.	-5.0	-5.0	-5.0
BOUND MASS	139.6	135.0	139.6
EXPER. MASS	139.6	135.0	139.6

FIG. 6. The π mesons. The M^0 , \bar{M}^0 , and M^\pm mass values of Fig. 1 and the $M\bar{M}$ binding energy of Fig. 3 are adjusted so as to precisely reproduce the pion mass values. A stringent test of this phenomenology is to then use these same parameters to reproduce the higher-mass resonances, since any systematic errors will scale with the resonance masses. As is shown in Figs. 7–9, the parameters that accurately reproduce the pion masses also accurately reproduce the masses of the higher-mass resonances of Fig. 5. The caber pairs shown here also reproduce the strangeness quantum number $S=0$ and the spin $J=0$ of the pion. Phenomenologically, it seems to be correct that every hadronic resonance must contain at least one neutral quantum M^0 or M_s^0 . If we postulate this as a requirement for the π mesons, then we have also reproduced the isotopic spin $I=1$ of the pion multiplet.

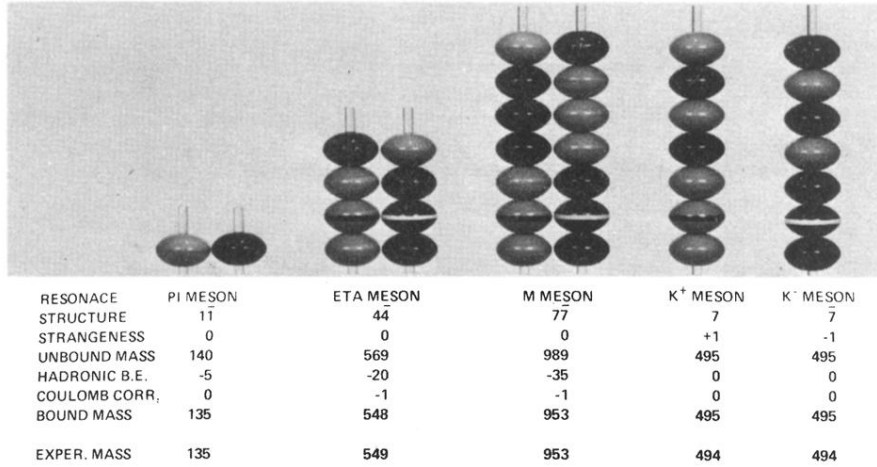
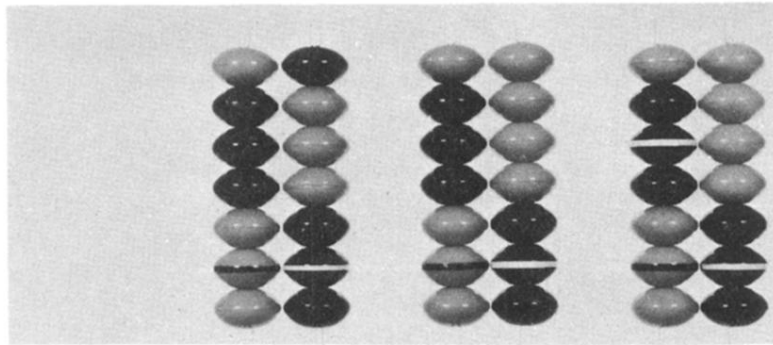


FIG. 7. The pseudoscalar bosons π , η , M , and K^\pm , members of the pseudoscalar nonet. As can be seen, the parameters that reproduced the pion masses in Fig. 6 also reproduce the masses of these resonances. Furthermore, the mass calculation singles out the M meson as the fundamental member of the M, η', δ^0 multiplet, in agreement with the results of Figs. 5 and 8 and with the systematics shown in Table V. The Coulomb corrections used here were obtained from parameter (10) in Table I: $R_{\max} \approx 0.6 \text{ F} \rightarrow e^2/2R_{\max} \approx -1 \text{ MeV}$, a result that is essentially independent of any specific choice made for the internal + and - charge distributions in the subquanta M^+ and M^- . The Caber charge assignments $\eta = 4^+ 4^-$, $M = 7^+ 7^-$, $K^+ = 7^+$, and $K^- = 7^-$ shown here are in agreement with the rule for Coulomb self-energies given at the bottom of Table I.



RESONANCE	M MESON	η' MESON	δ^- MESON
PRODUCTION PROCESS	$A+B \rightarrow A+B+RES.$	$A+B \rightarrow C+RES.$	$A+B \rightarrow A+RES.$
UNBOUND MASS	989	989	994
HADRONIC B. E.	-35	-30	-30
COULOMB CORR.	-1	-1	-1
BOUND MASS	953	958	963
EXPER. MASS	953	958	962

FIG. 8. The $M(953)$, $\eta'(958)$, and $\delta^-(962)$ mesons. The symmetric production mode $A+B \rightarrow A+B+M$ mandates that the M , which is created directly from kinetic collision energy, must have perfect internal particle-antiparticle symmetry, and hence a binding energy of -35 MeV. The asymmetric production mode of the η' , on the other hand (see Table V), suggests a particle-antiparticle "defect," an unmatched MM pair, which shifts the mass upwards by 5 MeV. This asymmetry also relates to the decay modes of the M and η' resonances, as is shown in Table V. The $M(953)$, $\eta'(958)$, $\delta^0(963)$ fine structure is a direct experimental indication of the 5-MeV internal $M\bar{M}$ binding energy that was invoked initially to explain the pion masses of Fig. 6. The δ^- appears here naturally as a charged form of the η' . From the Coulomb rule at the bottom of Table I, this charged state is formed by adding a charge, so that $\delta^- = 7^+ - 7^-$. The 7^+ caber shown here in the δ^- can also be observed singly as the K_L^0 meson of Fig. 9.

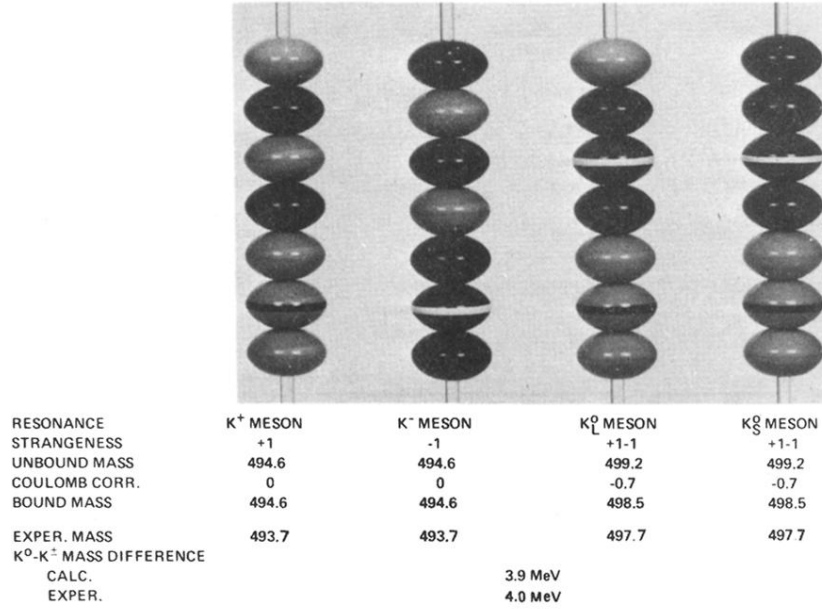


FIG. 9. The K mesons. The configurations shown here reproduce the absolute mass values, the charged splitting of the masses, and the strangeness characteristics. The $K^\pm = 7^\pm$ mesons were shown in Fig. 7. The $K_L^0 = 7^{+-}$ caber also appears in the δ^- resonance of Fig. 8; the K_S^0 is a more symmetric form of the 7^{+-} caber, and it has a $\pi\pi$ decay mode as compared to the $\pi\pi\pi$ decay mode of the K_L^0 . As is shown in Fig. 23 of Appendix A, these kaon configurations also have phenomenological significance with respect to the lifetimes of these resonances. From the calculation of the K^0 - K^\pm mass difference, the Coulomb correction in the K^0 must be -0.6 MeV (the value of -0.7 MeV shown here is from the radius $R_{\min} \approx \frac{1}{3}$ F given in Table I). Thus the K^0 charge separation must be $e^2/R^\pm = -0.6$ MeV $\rightarrow R^\pm = 2.4$ F. This large value for R^\pm is one of the main reasons for selecting a linear structure to represent the kaon. The conventional quark model predicts unambiguously (Ref. 10) that the K^\pm meson should be heavier than the K^0, \bar{K}^0 meson, so the present light-quark systematics offers a resolution of this long-standing theoretical puzzle. The kaon configurations shown here are $K^\pm = 3^\pm 4^0$, $K_L^0 = 3^+ 3^- 1^0$, and $K_S^0 = 3^+ 4^-$, so that K^\pm have strangeness ± 1 and K_L^0 and K_S^0 have mixed strangeness, as observed experimentally. The K_S^0 regeneration process, a secondary scattering, is a geometrical rearrangement of the K_L^0 structure.